CARBON DIOXIDE VARIABILITY WITHIN THE URBAN SALT LAKE VALLEY: AN OBSERVATIONAL AND MODELING STUDY

by

Carolyn H. Stwertka

A thesis submitted to the faculty of
The University of Utah
in partial fulfillment of the requirements for the degree of

Master of Science

Department of Atmospheric Sciences

The University of Utah

August 2013

The University of Utah Graduate School

STATEMENT OF THESIS APPROVAL

The thesis of **Carolyn H. Stwertka**

has been approved by the following supervisory committee members:

Courtenay Strong	, Chair	**7/17/2012** Date Approved
David Bowling	, Member	**7/17/2012** Date Approved
W James Steenburgh	, Member	**7/17/2012** Date Approved

and by **Kevin Perry** , Chair of

the Department of **Atmospheric Sciences**

and by Donna M. White, Interim Dean of The Graduate School.

ABSTRACT

A multiple-box model was designed to determine how anthropogenic, biological, and meteorological processes combine to produce diel cycles of carbon dioxide (CO_2) concentrations within the urban Salt Lake Valley (uSLV). The model was forced by an anthropogenic CO_2 emissions inventory, observed winds, sounding-derived mixing depths, and net biological flux estimates based on temperature, solar radiation, day of year, and ecosystem type. The model was validated using hourly CO_2 data from a network of sensors around the uSLV for years 2005-2009. The model accounted for 53% of the observations on an hourly basis and accounted for 90-94% of the mean diel cycle of the observations depending on the season.

Salt Lake Valley suffers from prolonged temperature inversions during the winter that trap pollutants and gases at the surface. The CO_2 network (co2.utah.edu) was compared with the CO_2 multiple-box model to determine whether the model could capture the main drivers of CO_2 variability during the Persistent Cold Air Pool Study (PCAPS). Time-height analyses were performed to facilitate investigation and explanation of CO_2 variability during PCAPS intensive observation periods (IOPs). The analyzed data included atmospheric soundings, CO_2 network data, quasivertical CO_2 profiles collected ascending by foot or vehicle, and laser-ceiliometer data.

To Mom, Dad, Zanny, Max, Ruth, Mort, Eve, Albert, and Kona for your eternal childlike excitement of scientific exploration. *"I am among those who think that science has great beauty. A scientist in her laboratory is not only a technician: she is also a child placed before natural phenomena which impress her like a fairy tale."* Marie Curie

CONTENTS

LIST OF FIGURES

LIST OF TABLES

ACKNOWLEDGMENTS

Funding for this research came from the NSF GK-12 Grant Think Globally, Learn Locally (TGLL). The CO_2 network data co2.utah.edu was funded through the Jim Ehleringer Lab (Department of Biology, University of Utah) and the Quality Control was done by Susan Bush. The Hidden Peak CO_2 network data is run by Britt Stevens at NCAR. The Persistant Cold Air Pool Study (PCAPS) data was from Neil Lareau and the Mountain Meteorology group at the University of Utah. The laboratory equipment used to study quasivertical transects of CO_2 was from the Dave Bowling Lab (Department of Biology, University of Utah).

CHAPTER 1

INTRODUCTION

1.1 Controls on CO_2 Concentrations

Over the past 800,000 years, CO_2 mole fractions remained between 170 and 300 parts per million (ppm) (Luthi et al., 2008). The year 2012, global mean CO_2 mole fractions reached 393.5 ppm (http://www.esrl.noaa.gov/gmd/ccgg/trends/). This marked increase in CO_2 is generally attributed to extensive combustion of fossil fuels beginning with the Industrial Revolution and extensive deforestation in the 1700s-1800s (Andres et al., 2009; Apadula et al., 2003; Bush et al., 2008; Coutts et al., 2007; IPCC, 2007; Pataki et al., 2003, 2005). Before the Industrial Revolution in 1750, the world population numbered around 750 million people. After the Industrial Revolution ended in 1805, the world population numbered 1 billion people. The year 2012 marked the 7 billion mark for world human population (UNFP, 2007). In a 2007 United Nations report, the UNFP (2007) estimated that over half the world's population lived in urban areas compared to less than 15% in 1900. This rapid urbanization is occurring in low and middle income countries typically lacking the capital, resources, and planning needed to enact environmental protection or develop infrastructure for climate change mitigation. The United Nations report estimated that by 2030, more than 80% of the human population will live in urban areas.

Urban areas are regions of concentrated population, development, transportation, industrial activity, economic development, and pollution. Most of the concentrated pollution in urban areas comes from the combustion of fossil fuels for heating and electricity generation, for running motor vehicles, and for industrial purposes. Urban areas have CO_2 mole fractions generally exceeding the atmospheric global average (Pataki et al., 2005; UNFP, 2007) and are believed to be drivers of climate change due to the production of concentrated CO_2 emissions and pollution (Grimmond et al., 2002; McKain et al., 2012; Pataki et al., 2007; Reid and Steyn, 1997; UNFP, 2007). Urban CO_2 studies are included in a rapidly expanding field that aims to find a representative measure of carbon emissions. However, finding a representative measure of carbon emissions is difficult because the data are limited and localized, the data are confined to the surface layer, and the sources of emissions vary (Grimmond et al., 2002; Idso et al., 2001, 2002; Molina and Molina, 2002; Pataki

et al., 2005; Reid and Steyn, 1997; Strong et al., 2011).

The forestry literature suggests urban forests can reduce CO_2 emissions in two ways. First, trees can store atmospheric CO_2 as long as they photosynthesize, have extensive roots, are not pruned too often, and are not burned when dead. Second, shade from trees surrounding buildings can reduce air conditioning demands, thus reducing the respective emissions associated with producing electrical power (Gottschalk et al., 2010; McPherson and Simpson, 1999; Nowak and Crane, 2002; Nowak et al., 2002). Idso et al. (2002) suggested that increases in CO_2 concentrations within urban areas could help stimulate plant growth to balance the increase in CO_2 emissions. Unfortunately, maximum photosynthesis occurs during maximum atmospheric mixing because both processes increase with insolation. Atmospheric mixing essentially largely offsets the summer biological sink in many urban environments (Coutts et al., 2007; Strong et al., 2011).

During the nighttime and the winter, the biosphere is a net source of CO_2 from respiration. In Krakow, Poland, Zimnoch et al. (2004) found the dominant source of CO_2 to be the biosphere, and on some summer evenings, CO_2 from respiration sometimes rose as high as winter anthropogenic CO_2. All said, urban areas are most often net sources of CO_2 into the atmosphere despite their urban forests (Grimmond et al., 2002; Moriwaki and Kanda, 2004; Ramamurthy and Pardyjak, 2011).

1.2 Urban CO_2 Dome

The volume of enhanced CO_2 mixing ratios within urban areas has been called the Urban CO_2 dome (Idso et al., 1998). The urban CO_2 dome can be thought of as a gaseous analog of the Urban Heat Island Effect – the enhanced urban temperatures relative to temperatures in surrounding rural areas (Environmental Protection Agency, 1990; Moriwaki and Kanda, 2004; Oke, 1967). In an urban area of 1 million residents, annual temperatures can range from 1-2°C warmer than surrounding rural areas, and can reach 12°C higher on calm nights (Akbari, 2005). Similarly, the Urban CO_2 dome refers to the tendency for urban areas to have higher CO_2 concentrations than the surrounding rural areas (Idso et al., 1998; Pataki et al., 2003). Idso et al. (2002) found that the CO_2 concentrations in the city of Phoenix, Arizona in the winter morning hours could reach up to 50% higher than surrounding rural values, and 25% higher in the afternoon. Similarly the CO_2 network (http://co2.utah.edu) indicates that morning winter concentrations of CO_2 in Salt Lake City, UT can reach up to 600 ppm which can be up to 50% higher than surrounding rural areas (400 ppm). Afternoon-evening concentrations are generally lower than morning concentrations (around 500 ppm) yet are still 25%+ higher than surrounding rural areas (http://co2.utah.edu). In both Phoenix and Salt Lake City, mid-day concentrations can be as low as the global mean average due to atmospheric mixing or strong synoptic winds (Idso et al., 2002; Pataki et al., 2003;

Strong et al., 2011). Similar urban CO_2 domes have been identified internationally in Rome, Italy; Krakow, Poland; Paris, France; Copenhagen, Denmark; Kuwait City, Kuwait; and Benin, West Africa (Gratani and Varone, 2005; Kelome et al., 2006; Lichtfouse et al., 2003; Nasrallah et al., 2003; Soegaard and Moller-Jensen, 2003; Widory and Javoy, 2003; Zimnoch et al., 2004).

The urban CO_2 literature describes similar CO_2 diel cycles within many cities around the world. A diel double peak in CO_2 is often found: a peak in the early morning due to morning rush hour traffic emissions into a shallow boundary layer, and a peak during evening rush hour traffic enhanced by residential natural gas combustion into a shallow nocturnal boundary layer. CO_2 mole fractions during midday are typically the lowest of the day due to atmospheric mixing, and in the summer, enhanced biological uptake of CO_2. CO_2 mole fractions tend to steadily increase overnight due to anthropogenic and biospheric emissions into a shallow nocturnal boundary layer (Coutts et al., 2007; Henninger, 2008; Idso et al., 1998, 2002; Koerner and Klopatek, 2002; Nasrallah et al., 2003; Pataki et al., 2003, 2006, 2007; Soegaard and Moller-Jensen, 2003; Strong et al., 2011; Takahashi et al., 2002; Velasco et al., 2005; Widory and Javoy, 2003).

1.3 CO_2 in Salt Lake City, UT

With rising population comes rising demand for electricity. Coal is the largest producer of carbon dioxide emissions in Utah, followed by petroleum products, and natural gas (Woods et al., 2001). Coal-fired power plants in central Utah dominate the electricity supply in Utah with minimal contribution from two geothermal facilities. Utah contains four of the United States' 100 largest oil fields in addition to two of its largest 100 natural gas fields (USEIA, 2011). Around 80% of Utah's households heat their homes with natural gas (USEIA, 2011), and only around 10% of Utah's households use geothermal (USEIA, 2011). Utah has five oil refineries, located in northern Salt Lake City. As Utah's population continues to grow [currently at 2.2 million (Bureau, 2012)], Utah has the potential to continue to develop fossil fuels from very large deposits of oil shale, but also has the potential to develop renewable energies such as solar, hydroelectric, and wind farms. These energy-use and energy-development decisions will impact the local and global climate for future generations. Controlling emissions in urban environments can help reduce the global increase in carbon dioxide (Balling Jr. et al., 2002; McKain et al., 2012; Pataki et al., 2005; Strong et al., 2011).

Salt Lake City, Utah has a network of CO_2 monitoring stations that have been running since 2001 (Strong et al., 2011; http://co2.utah.edu). Using this CO_2 network and additional isotopic analysis, Pataki et al. (2005) found that natural gas was the largest source of CO_2 at the center of Salt Lake City ($> 50\%$) in the winter with contributions becoming negligible in the summer; gasoline combustion remained a large source throughout the year, and biological respiration was

the largest source (up to 60%) during the growing season in rural areas. The source difference between natural gas combustion and gasoline combustion was found to have a diurnal cycle (Pataki et al., 2006). Natural gas contribution to CO_2 mole fractions was highest at predawn, accounting for 60-70% of the total fossil fuel-derived CO_2, and was lowest during late afternoon and evening rush hours, accounting for 30-40% of the total fossil fuel-derived CO_2 (Pataki et al., 2006). These temporal patterns are consistent with an increase in nocturnal home heating and rush-hour increases in traffic.

CO_2 variability within the Urban CO_2 dome is largely the result of natural gas combustion, fossil fuel combustion, and plant and soil respiration. However, CO_2 fluxes also strongly depend on topography, synoptic meteorology, and regional atmospheric processes (Koerner and Klopatek, 2002; Pataki et al., 2003, 2005, 2007; Strong et al., 2011). Few studies have analyzed the vertical profile of CO_2 above an urban environment. The sparse information available indicates that, above the surface urban layer, the CO_2 concentrations tend to decrease to rural or background mole fractions (Balling Jr. et al., 2002; Pataki et al., 2005). Pataki et al. (2005) used the elevation differences in the Salt Lake City, UT CO_2 network to study vertical variations of CO_2 during a winter cold-air pool in Salt Lake City. The results indicated that atmospheric stability and the height of the capping inversion strongly influenced CO_2 mole fractions, but the urban atmosphere could be relatively well-mixed below the capping inversion. Such analyses of vertical variation of wintertime CO_2 can provide information about complex transport and mixing in addition to carbon cycling in urban mountain valleys.

1.4 Modeling

Numerical models are useful for understanding and forecasting variability in atmospheric composition, and the predictive skill and knowledge provided by models can inform development of regulations to minimize greenhouse gas and pollutant impacts. Modeling efforts studying urban CO_2 variability range in scale and complexity from relatively simple box models (Reid and Steyn, 1997; Strong et al., 2011) to mesoscale atmospheric transport models (McKain et al., 2012, e.g.) and nested global-through-urban 3-D models such as GATOR-GCMOM (Jacobson, 2010).

Jacobson (2010) used a global model to study the contribution of urban CO_2 into a larger urban CO_2 dome. The model underestimated the surface CO_2 mole fractions but was able to capture the Urban CO_2 dome above Los Angeles.

McKain et al. (2012) used a complex mesoscale atmospheric model with a 1.3-km resolution to assess whether surface observations of CO_2 mole fractions could be used to verify greenhouse gas emissions in the uSLV. The model realistically simulated many features of the CO2 data, but

hourly data-model mismatches stemmed from inadequate simulation of shallow circulations and the precise timing of boundary-layer stratification and destratification.

Reid and Steyn (1997) developed a simple multiple-box model to simulate the diel variability of CO_2 in Vancouver, Canada using a mass balance equation of the major sources and sinks of CO_2. There were eight boxes, each of 1.9-km in horizontal dimension with a flux tower available for validation in the eighth box. The mass balance equation specified the biological flux, the anthropogenic flux, the advection (direction and wind speed), the boundary layer growth, and entrainment. The multiple-box model was able to accurately represent all stages of the diel cycle of CO_2 in Vancouver which included the early morning peak, the subsequent decrease due to atmospheric mixing and entrainment, the afternoon minimum, and the rise to the secondary evening peak.

Extending the multiple-box modeling framework of Reid and Steyn (1997), Strong et al. (2011) developed a similar computationally efficient framework to study the variability of CO_2 in the extended Salt Lake Valley. The model accounted for 53% of the variance in hourly CO_2 observations and accounted for 90-94% of the variance of the mean diel cycle of the observations depending on the season. The success of the multiple-box model motivated its use in studying CO_2 variability during the Persistent Cold Air Pool Study (PCAPS; Chapter 3).

1.5 Organization of Thesis

Chapter 2 provides an overview of the multiple-box model and presents results used in development of the biological flux input for the multiple-box model, focusing on details omitted from (Strong et al., 2011) for conciseness.

Chapter 3 presents an observational and modeling investigation of CO_2 variability during the Persistent Cold Air Pool Study (PCAPS) period of the winter of 2010-2011. This chapter is the basis for a manuscript in preparation (Stwertka et al., 2012).

CHAPTER 2

MODELING THE BIOLOGICAL CO_2 FLUX

2.1 Multiple Box Model

The multiple-box model developed by Strong et al. (2011) solves a mass balance equation to simulate the temporal evolution of CO_2 concentration on a grid encompassing the uSLV. The terms of the mass balance equation are the major sources and sinks of CO_2 as described in Reid and Steyn (1997). These include the total anthropogenic flux of CO_2 being produced by all human activities, the biological flux of CO_2 due to photosynthesis and respiration, advection of CO_2, and the entrainment of air from above the boundary layer into the boundary layer.

Similar to Reid and Steyn (1997), the model's basic formulation is a mass balance equation for CO_2 (Lettau, 1970)

$$\frac{\partial(CAh)}{\partial t} = QA - u\frac{\partial(CAh)}{\partial x} - v\frac{\partial(CAh)}{\partial y} + HC_h\frac{\partial h}{\partial t}A \tag{2.1}$$

where C is CO_2 concentration in kg m^{-3}, A is box horizontal area, h is box vertical extent ("mixing depth"), Q is the net flux of CO_2 into the grid box (sum of anthropogenic emissions $[Q_a]$ and net biological CO_2 flux $[Q_b]$) in kg m^{-2}s^{-1}, u is the component of wind in the model x-direction, v is the component of wind in the model y-direction, and C_h is the ambient CO_2 mole fraction above h. The term H represents the Heaviside step function with an argument $\partial h/\partial t$, which sets entrainment (last term on the right hand side) to zero if the mixing height is decreasing

$$H = \begin{cases} 1 & \text{if } \frac{\partial h}{\partial t} \geq 0 \\ 0 & \text{if } \frac{\partial h}{\partial t} < 0. \end{cases}$$

The effects of diffusion are assumed negligible (Strong et al., 2011).

Dividing through by A, Equation (2.1) can be written for box i as

$$\underbrace{\frac{\partial C_i}{\partial t}}_{\text{rate of change}} = \underbrace{\frac{Q_{a,i}}{h}}_{\text{anthropogenic}} + \underbrace{\frac{Q_{b,i}}{h}}_{\text{biological}} \underbrace{-u_i\left(\frac{\partial C}{\partial x}\right)_i - v_i\left(\frac{\partial C}{\partial y}\right)_i}_{\text{advection}} + \underbrace{\frac{H}{h}\frac{\partial h}{\partial t}(C_h - C_i)}_{\text{entrainment}} \tag{2.2}$$

where descriptive labels have been added to facilitate referring to terms in the equation. Strong et al. (2011) simulated Equation (2.2) on a 10-km grid with $n_x = 9$ adjacent boxes in the east-west

direction and $n_y = 18$ adjacent boxes in the north-south direction, for a total of $n = 162$ boxes (Fig. 2.1b). Equation (2.2) was integrated using the Crank-Nicolson method, meaning that terms on the right hand side were approximated by the average of their finite-difference values at time j and $j+1$, and details of the associated numerical formulations are given in an Appendix at the end of this chapter. Strong et al. (2011) used a 30-minute time step, incorporated wave-permeable boundary conditions (Durran et al., 1993), and applied a 9-point selective optimized filter (Bogey and Bailly, 2004) at each time step for numerical stability. This chapter focuses on development of the biological flux, and development of other model inputs is reviewed in Section 2.4 following Strong et al. (2011). The performance of the model was evaluated using available observations.

Within the Salt Lake Valley, near-surface CO_2 mole fractions have been measured continuously since 2001 (http://co2.utah.edu) using a network of infrared gas analyzers at urban and rural sites (Ehleringer et al., 2009; Strong et al., 2011, Fig. 2.1a;). Measurements from sites 1-5 in Fig 2.1a constituted the urban Salt Lake Valley (uSLV) sites. Two sites, "Kennecott" on the upper western edge of the Salt Lake Valley (site 6, Fig. 2.1a), and "Hidden Peak" in the Wasatch Mountains (site 7, Fig. 2.1a) were considered nonurban or rural sites [see also Table 1 in Strong et al. (2011)].

In the remainder of this chapter, Section 2.2 describes basic carbon cycle ecology focusing on the atmosphere-biosphere flux of CO_2. Section 2.3 details the development of the biological flux input for the multiple-box model, Section 2.4 describes tests performed to investigate the model's sensitivity to specified fluxes, and Section 2.5 provides a summary and discussion of chapter results.

2.2 Basic Ecosystem-Atmosphere Carbon Dynamics

This section briefly reviews some fundamental concepts of importance to development of the biological flux for the multiple-box model, drawing especially from the textbook written by Chapin et al. (2002). Subsections are provided focusing on carbon cycling, gross primary productivity, soil and plant respiration, and net ecosystem exchange.

2.2.1 Carbon Cycling

Carbon within the Earth system is contained in four pools: atmosphere, ocean, land (soils and vegetation), and sediments/rocks. The dynamic and constant exchanges that occurred between these pools is called the carbon cycle. Fluxes of carbon in or out of sediments and rocks occur over millions of years from geologic processes such as plate tectonics, weathering, uplift, and volcanism. Although fluxes of carbon between the atmosphere and ocean were not a direct input to the CO_2 mass balance in the Salt Lake Valley, they represented an integral component of the global carbon cycle. Development of the biological flux for the multiple-box model focused on the exchange of

carbon in the form of gaseous carbon dioxide between the biosphere and atmosphere on timescales from seconds to seasons.

Carbon in the atmosphere is primarily in the form of carbon dioxide gas (CO_2). In biosphere-atmosphere interactions, CO_2 is removed from the atmosphere through plant photosynthesis and returned to the atmosphere through plant or soil respiration. Photosynthesis is the process of converting the visible wavelengths of solar radiation and atmospheric CO_2 into carbon-containing organic compounds to provide energy and food for plant growth. The organic compounds can move within ecosystems and are eventually released into the atmosphere via respiration or combustion.

During photosynthesis, CO_2 diffuses through a layer of air near the leaf surface, then travels through the leaf's stomata (small pores in the leaf surface) into the leaf. Once inside, the CO_2 diffuses through air spaces between the cells and dissolves in a thin layer of water inside the cell walls before traveling from the cell surface to the chloroplasts. Chlorophyll, a light absorbing pigment, absorbs the incoming photosynthetically active radiation (PAR) and funnels it to the chloroplasts, within which light-harvesting reactions occur. Water is split into H^+ and O_2. The H^+ atoms react with the CO_2 molecules to form organic compounds such as glucose (sugar for energy use) or cellulose (plant mass) and the O_2 diffuse out of the system into the atmosphere as a byproduct.

The water that facilitates the transfer of CO_2 into the interior leaf could easily evaporate and diffuse through stomata into the atmosphere. This process is called transpiration. Plant growth is a trade-off between gaining CO_2 into the system to drive photosynthesis, and losing water necessary for photosynthesis to occur. To maintain the most efficient balance of photosynthetic input to the plant and transpiration, plants regulate their CO_2 uptake by controlling the diameter of their stomata. Plants that are water stressed often need to reduce their stomata diameter. This reduces the quantity of CO_2 entering the plants, reducing photosynthesis, and reducing the efficiency of the plants for converting solar radiation into food and energy for plant growth.

The amount of carbon dioxide stored or released depends on ecosystem processes, their interactive controls, and the ecosystem's "state variables": climate, parent material (i.e., rocks, soil), topography, and potential biota (i.e., organisms within the region that could exist at a site) (Chapin et al., 2002). Climate in the broad geographical sense plays the largest role in creating the distribution of biomes (types of ecosystems), and carbon storage within these biomes depends on plant material, soil types, topography, and potential biota.

Interactive controls on an ecosystem are those involving interaction and alteration of the environment (Chapin et al., 2002). Important interactive controls include the supply of resources that could support the growth of organisms, modulators which influence the rates of ecosystem processes such

as temperature, disturbance regimes that occur by fire or disease outbreak, the biotic community that is present and its diversity of functional types (groups of species with a similar role in community or ecosystem processes), and human activities responsible for alteration of landscape and atmospheric composition. Ecosystem processes such as photosynthesis and respiration both respond to yet also control the interactive processes that directly determine their activity (Chapin et al., 2002).

2.2.2 Gross Primary Productivity (GPP)

The total amount of carbon taken up and stored in an ecosystem is called the gross primary production (GPP). Photosynthesis through a single leaf, the process through which most carbon enters ecosystems, depends on the availability of photosynthetically active radiation (PAR), CO_2 in the atmosphere, temperature, and nitrogen supply (Chapin et al., 2002). The long-term state controls and the interactive controls determine the characteristics of ecosystem differences, but the short-term direct controls determine the seasonal and diurnal variations in GPP. The short-term direct controls on GPP are leaf area, nitrogen, season length, temperature, light, and CO_2. Leaf area, in turn, depends on water and nitrogen within the soil. Human pollution and disturbance can cause a reduction of photosynthesis. Pollutants reduce the carbon gain in a plant primarily by damaging the leaf area which then reduces photosynthetic capacity (Chapin et al., 2002). Pollutants often found in urban areas such as SO_2, ozone, and acid rain can reduce photosynthesis by entering the leaf and damaging the photosynthetic machinery. This causes the plants to allow less CO_2 in through their leaves because they cannot store the same quantity of carbon and energy. Disturbances such as cattle grazing or deforestation can decrease the total area of the photosynthesizing leaves.

2.2.3 Soil and Plant Respiration

Carbon is accumulated in the plant ecosystem through GPP, but leaves the ecosystem through respiration, disturbance, or lateral transference to other ecosystems. Respiration provides energy for growth and maintenance of biomass through breaking up stored carbon sugars. At the ecosystem scale, respiration occurs at all times in nonphotosynthetic plant organs and occurs in leaves at night. Nighttime respiration is included in GPP.

Respiration rates tend to increase exponentially with temperature, but this tendency has been altered by adaptation and acclimation to regional climate. For example, respiration from plants in warm or cold climates may exhibit contrasting sensitivities to temperature, but both plants could have similar respiration rates when measured in their natural mean habitat temperatures (Chapin et al., 2002).

2.2.4 Net Ecosystem Exchange (NEE)

One of the goals in this chapter is to develop a Net Ecosystem Exchange (NEE) that could be used as the biological flux input (Q_b) for the multiple-box model, where NEE is the net exchange of CO_2 between the atmosphere and the ecosystem. At night, GPP is zero, so NEE quantifies ecosystem respiration (Chapin et al., 2002). NEE is the balance between GPP and respiration from autotrophs and heterotrophs. Autotrophs are producing organisms that can create and use their own food and energy from substances present in their environment. However, the carbon balance in an ecosystem must also include the respiration of heterotrophs, which are organisms that eat live or dead organic matter, convert it to food for growth, and respire out CO_2.

NEE is measured by eddy covariance towers and is defined such that fluxes into the ecosystem are considered negative. A network of eddy covariance towers measuring NEE in ecosystems around the world indicates that, in the absence of disturbance, temperate ecosystems are net sinks of CO_2 (Chapin et al., 2002). As discussed above, GPP, respiration, and consequently NEE are closely linked to time of day and season of the year. Seasonal changes drive NEE across latitudinal bands. This creates an annual fluctuation in atmospheric CO_2 of around 6 parts per million by volume (ppmv) that is caused by northern hemispheric land mass photosynthesis (Keeling et al., 1996).

2.3 Development of the Biological Flux

To quantify Q_b, each box within the model was assigned an ecosystem (Fig. 2.1c) based on United States Geological Survey data (Homer et al., 2004). Since long-term measurements of Q_b were not available, we identified a comparable "proxy" ecosystem in the AmeriFlux network (Section 2.3.1) for each ecosystem. Lookup tables of biological CO_2 flux were created for each proxy ecosystem based on day of year, incoming solar radiation, and air temperature. Finally, to specify Q_b at each model box, the corresponding proxy ecosystem Q_b lookup table was queried with the meteorological conditions at the Salt Lake City International Airport for the model time.

The remainder of this section describes the steps summarized above, covering use of the AmeriFlux network (Section 2.3.1), assignment of land use categories (Section 2.3.2), assignment of ecosystem types (Section 2.3.3), and selection of AmeriFlux proxy ecosystems (Section 2.3.4). Section 2.3.5 defines the structure of the lookup tables, Section 2.3.6 details how lookup tables were created, and Section 2.3.7 presents an evaluation of lookup table performance.

2.3.1 AmeriFlux Network

AmeriFlux is a network of continuous observations of ecosystem level exchanges of CO_2 and other important biological variables across North, South, and Central America. AmeriFlux was established in 1996 as part of FLUXNET, a global network of micrometeorological tower sites that

use eddy covariance methods to measure the exchanges of carbon dioxide, water vapor, and energy between terrestrial ecosystems and the atmosphere.

AmeriFlux Level 4 data are the highest level of quality controlled data in the network. By definition, Level 4 files contain gap-filled and filtered records, complete with measured net ecosystem exchange, calculated gross productivity, and total ecosystem respiration terms on varying time intervals including hourly, daily, weekly, and monthly with flags regarding the quality of the original and gap-filled data. The data files contain the following variables: month, day, day of year (DOY), global radiation, air temperature, vapor pressure deficit, soil temperature, precipitation, soil water content, mean sensible heat flux, mean latent heat flux, NEE, ecosystem respiration based on NEE, and gross primary production based on NEE. Proxy ecosystems for the uSLV were found within the North America AmeriFlux network as detailed in Table 2.1.

2.3.2 Land Use Categories

Land use categories are economic categories defined by the "Standard land use coding manual: a standard system for identifying and coding land use activities" (Urban Renewal Administration and Bureau of Public Records, 1965). Land cover categories are based on visual features. When studying biosphere-atmosphere interactions, both land use and land cover are necessary for accurate prediction of interactions between the biosphere and atmosphere. The United States Geologic Survey (USGS) Land Use Land Cover (LULC) data set developed by Anderson et al. (1976) is based on remote sensing color-infrared photographs. NASA high-altitude aerial photographs and the National High-Altitude Photography (NHAP) program were the primary sources of remote sensing imagery for the Level II data (Homer et al., 2004). Level II data are between 1-km and 2.5-km resolution. There were 9 Level I LULC categories derived from a Landsat type satellite and 37 Level II categories more specifically defining LULC types. For example, a Level I category is "Forest Land." Level II categories within Forest Land are "Deciduous Forest Land," "Evergreen Forest Land," and "Mixed Forest Land" (Anderson et al., 1976).

The AmeriFlux network classifies its vegetation types based on the International Geosphere Biosphere Programme (IGBP). This 1-km resolution dataset consists of 17 categories. These classifications are derived from NOAA's Advanced Very High Resolution Radiometer's (AVHRR) Normalized Difference Vegetation Index (NDVI) (Loveland and Belward, 1997). Each of the 17 IGBP LULC categories are represented by one of the 37 Level II USGS categories making it possible to assign an Ameriflux ecosystem as a proxy to the ecosystems found in the uSLV.

The first criterion of choosing a proxy ecosystem was that there must be five or more years of level 4 AmeriFlux data. The second criterion was how similar the proxy ecosystem was to the uSLV ecosystem.

2.3.3 Salt Lake Valley Ecosystem Types

The United States Environmental Protection Agency (US EPA) has defined ecoregions of North America (Woods et al., 2001). Ecoregions are classified by similar geology, physiography, vegetation, climate, soils, land use, wildlife, and hydrology. These data are used to compare proxy ecosystems to the uSLV ecosystems defined by the LULC categories discussed above.

The Salt Lake Valley is part of the Great Basin which is the northern part of the Basin and Range province. The Salt Lake Valley generally is categorized within the Central Basin and Range and the Wasatch and Uinta Mountains ecoregions. The Central Basin and Range is internally-drained by ephemeral streams lower than around 1600 masl, has more saline and alkaline soils than the sagebrush Steppe Valley to the north, is drier than the Wasatch and Uinta Mountains, has more shrubs and grasses than the Snake River Plain, and is cooler than the Mojave Basin and Range (Woods et al., 2001). The land is used for a variety of activities from grazing to irrigated cropland to urban development and large military bases. The Wasatch and Uinta Mountains are generally within 2,500 - 3,300 masl. The primary water source is winter precipitation in the form of snow. Annual water totals can range from 76-178 cm. Englemann spruce, Douglas fir, aspens, sagebrush, and other alpine plants are found within the region. Its primary uses are for wildlife habitat, recreation, logging, and water supply for the Salt Lake Valley (Woods et al., 2001).

The eastern part of the urban Salt Lake Valley and the Utah Valley is considered Moist Wasatch Front Footslopes. This subecoregion supported the majority of Utah's population and commercial activity. The area is nonglaciated and at an elevation between 1,280 to 1,600 masl. Annual precipitation averages 25-56 cm. The water comes from perennial streams and aqueducts that originate in the Wasatch Range. This area includes the irrigated croplands which grow alfalfa, vegetables, and small grains in addition to orchards (Woods et al., 2001). Natural vegetation is mainly sagebrush, and desert grasses. However, widespread urban, suburban, industrial, and commercial activity have taken over and planted deciduous trees within urbanized areas. Within this ecoregion, the vegetation type for the multiple box model included the residential forest and croplands (Fig. 2.1b, symbols $\circ$ and $\blacktriangle$, respectively).

The area to the west of the urban Salt Lake Valley that nestles near the Oquirrh Mountains is classified as Woodland and Shrub Covered Low Mountains. This type of ecoregion commonly has Juniper trees, pinyon pines, bitterbrush and western serviceberry as well as large cleared areas for grazing. The elevations range from 1,500-2,700 masl with annual precipitation ranging from 25-56 cm. Winter temperatures frequently drop below freezing. Summer temperatures often exceed 30°C (Woods et al., 2001). The vegetation type assigned to this ecosystem type in the multiple box model was brushlands (Fig 2.1b, symbol $*$).

The foothills of the Wasatch Mountains, 1,500-2,400 masl, fall under the ecoregion of Semi-arid Foothills. This region receives 30-56 cm of precipitation. Winter temperatures frequently drop below freezing, and summer temperatures often exceed 30°C. This region includes junipers, pinyons, sagebrush, grama grass, mountain mahogany, gambel oak and maple-oak scrub (Woods et al., 2001). The vegetation type assigned to this ecosystem type in the multiple box model was alpine forest (Fig. 2.1b, symbol ♦).

The Wasatch Mountains are part of the Wasatch Montane Zone. The Wasatch mountains are forested with Douglas fir, aspens, Engelmann spruce, and subalpine fir. Their underlying geology consists of sedimentary and metamorphic rocks that are commonly visible. The vegetation type included in the model within this ecoregion is the subalpine forest. Elevations range from 2,400-3,000 masl with annual precipitation ranging from 38-127 cm depending on aspect, elevation, temperature, and density of trees. Winter temperatures were not provided in Woods et al. (2001), but are generally below freezing with summer temperatures generally exceeding 20°C. In the multiple box model, this area was also assigned alpine forest (Fig. 2.1b, symbol ♦).

The small area of wetlands surrounding the Great Salt Lake is part of a subecoregion within the moist Wasatch front-slope. The wetlands are home to migratory birds, and the salt water marshes can be contaminated by fresh water river runoff that increases the level of the Great Salt Lake (GSL). The soils are poorly drained and often have a high saline mole fraction due to proximity to the GSL. The vegetation type included in the multiple box model from this ecoregion was the Wetland (Fig. 2.1b, symbol ◇).

Finally, the barren and water covered landscape in and around the GSL that are not considered Wetland are considered Salt Desert or Shadescale-Dominated Saline Basins. The elevations range from 4,200-4,650 masl, with 10-20 cm of precipitation annually, wintertime temps ranging from below freezing to 4-10°C, and summer temperatures reaching above 32°C. Soils are mostly clayey, poorly drained; there are salt flats, mud flats, saline lakes, playas, and minimal salt-tolerant and drought-tolerant vegetation. The vegetation type assigned to this ecosystem type in the multiple box model was barren land and water (Fig. 2.1b, symbol ▪).

2.3.4 Proxy Ecosystem Selections

The Mead Irrigated Croplands in Nebraska was chosen as an Ameriflux proxy for croplands (Table 2.1). Mead Croplands are in a temperate climate and are designated as IGBP croplands (Verma et al., 2005). The soil consists of silty clay loams and maize-soybean rotation under no-till practice. Approximately 1/3 the crop residue is left on the surface. The Mead Croplands in Nebraska are classified as part of the Western Corn Belt Plains. Specifically, the subecoregion is the Nebraska Kansas Loess Hills. This region features a tallgrass prairie with cottonwood forests along

the flood plains. The land is primarily used for crops such as wheat, corn, soybeans, and alfalfa (Chapman et al., 2001).

Niwot Ridge in the Colorado Rockies was chosen as the Ameriflux proxy ecosystem for the upper elevation forest surrounding the uSLV (Table 2.1). Niwot ridge is classified as an IGBP evergreen needleleaf forest in a temperate climate. The trees within the forest are approximately 100 years old (Monson et al., 2005). Niwot Ridge in Colorado is a part of the Crystalline Subalpine Forests ecoregion that exists from 2,600 - 3,600 masl in steep, forested slopes below mountain tops. Due to intense winter snow storms and monsoonal pulses, the area can receive 76-147 cm of water annually depending on elevation and aspect. Temperatures in the winter remain below freezing and can be as low as -5°C in the summer. Similar to the Wasatch Mountains, the Niwot Ridge forests include species such as Engelmann spruce, subalpine fir, aspen, and pockets of lodgepole pines. The Colorado subalpine forests are plagued by disturbances such as insect outbreaks, fire, and avalanches. Similar to the Wasatch subalpine forest, bedrock geology consists of metamorphic materials. However, the Colorado geology includes igneous intrusions. Similar to the Wasatch, primary land-use involves hiking, mining, and recreational activities.

The Harvard Forest in Massachusetts was chosen as the Ameriflux proxy ecosystem for the residential forest (Table 2.1). The Harvard Forest is also in a temperate climate and is classified as an IGBP deciduous broadleaf forest. The stand age is approximately 80.5 years (mean) and measurements have been made since 1964 (Urbanski et al., 2007). Because of urban versus rural forest density and productivity, the Harvard proxy ecosystem NEE was scaled by 0.5 for Q_b. The model simulations are not terribly sensitive to this parameter, and its specification at 0.5 is supported by studies showing that rural forests sequester about twice as much CO_2 as urban forests per unit land area because of differences in tree density (McPherson and Simpson, 1999). Harvard Forest is part of the Worcester/Monadnock Plateau (Griffith et al., 2009). The rolling hill plateaus have many ponds, lakes, and reservoirs. The elevation primarily ranges from 91-245 masl with some topography over 305 masl. The vegetation is mainly a mix of transitional hardwoods like red oak, sugar maple, beech, white pine, hemlock and evergreen forests. The area receives 76-145 cm of precipitation annually, temperatures largely remain below freezing during the winter, and from 12-27°C in the summer (Griffith et al., 2009).

The Viara grassland was chosen as the Ameriflux proxy ecosystem for the model brushlands (Table 2.1). The Vaira grasslands in California are located at the lower foothills of the Sierra Nevada Mountains. The elevation ranges from 91-305 masl. Growing season is confined to the wet season - typically from October to early May. Unfortunately, there is not a detailed dataset for the California Environmental Protection Agency (EPA) Ecoregions, but the Western Region Climate

Center (WRCC) did provide climatological data for the region (Western Regional Climate Center, 2012). The climate is Mediterranean with warm wet winters, and hot dry summers. The annual precipitation is 50-100 cm (Western Regional Climate Center, 2012). The grasslands are dominated by C3 grasses (Xu and Baldocchi, 2004). The soil type is very rocky silt loam and the grasslands are grazed in a region of oak/grass savanna (Xu and Baldocchi, 2004).

Since no wetlands satisfying the proxy selection criteria were available in the AmeriFlux dataset, wetlands were assigned as croplands (Table 2.1). The barren and water ecosystems were also assigned a zero CO_2 flux.

2.3.5 Determining Lookup Table Variables

Lookup tables were made for each proxy ecosystem, and illustrative slices through these lookup tables are shown in Figs. 2.2-2.5. To determine which variables to use as predictors for the Net Ecosystem Exchange (NEE), a set of correlations were calculated between NEE and variables provided in the AmeriFlux data (Table 2.2). As expected from known environmental controls on GPP and respiration (Section 2.2), global radiation was highly negatively correlated with NEE, meaning that high global radiation values supported enhanced photosynthesis and sequestration of CO_2. Latent heat flux was also highly negatively correlated with the NEE in part because latent heat flux tends to scale with global radiation.

Temperature was not as highly negatively correlated with NEE indicating its lesser, but still important, role in atmosphere-biosphere exchange of CO_2. Vapor pressure deficit had negative correlations with NEE comparable to those of air temperature for all proxy ecosystems in part because increases in temperature also tend to increase the vapor pressure deficit (the difference between the pressure exerted by water vapor in a saturated airmass and the pressure exerted by water vapor in unsaturated airmass with the same temperature and pressure).

Precipitation was poorly correlated with NEE in part because it has an indirect effect on the plant system which operates on a timescale longer than the hourly analysis in Table 2.2.

Temperature and global radiation were determined to be the predictors of NEE for the lookup tables because they correlated well with NEE and were readily available for the simulation period. It would have been possible to develop lookup tables for respiration and GPP separately, and then combine them together to obtain NEE. However, since NEE was measured at the AmeriFlux sites and corresponds directly to Q_b in the model inputs, single lookup tables for NEE were developed. Moreover, the GPP and respiration values in the Ameriflux data were estimates derived from the NEE measurements.

NEE lookup tables were created for each proxy ecosystem. Each lookup table specified a value of NEE as a function of day of year (d), global radiation (R), and air temperature (T). The

lookup tables were thus three-dimensional, with the first dimension corresponding to day of year with bins centered on $1 \leq d \leq 365$, the second dimension corresponding to air temperature with bins centered approximately every seven degrees from $-20^{\circ}C \leq T \leq 30^{\circ}C$, and the third dimension corresponding to global radiation with bins centered approximately every 122 W m^{-2} from $0 \leq R \leq 1{,}000$ W m^{-2}. To populate the value in a given bin in the three-dimensional ($d \times T \times R$) space, AmeriFlux NEE values from the proxy site were averaged over observation times satisfying the following criteria:

1. observed T fell within the range corresponding to the bin
2. observed R fell within the range corresponding to the bin
3. observed d was within the week centered on the d corresponding to the bin

Averaging over data during the week centered on each bin's d was done to increase the sample size for the estimate of the mean, providing smoother output from the table. When the table was used for a given ecosystem, the T, R, and d valid for a specific time step in the model specified a bin, and the NEE value in that bin was used as model input Q_b.

The lookup tables, for completeness, had cells corresponding to potentially unrealistic combinations such as very low T and very high R, and nearest-neighbor interpolation was used to populate any cells where observations were not available. The model occasionally queried cells that were realistic for the Salt Lake Valley, but fell outside the range of observations of R or T at the Ameriflux proxy site (Tables 2.3 and 2.4; discussion in next section). During the development of each proxy ecosystem lookup table, one year of data was withheld to evaluate the table's ability to simulate NEE observations at the AmeriFlux site (Section 2.3.7).

2.3.6 Lookup Table Descriptions

2.3.6.1 Harvard Forest

An illustrative winter and summer day from the Harvard Forest lookup table are shown in Fig. 2.2. In the winter, there was a very small net output of CO_2 into the atmosphere due to respiration under conditions of low global radiation and high temperatures (light red shading, Fig. 2.2a). In the summer, the largest net removal of CO_2 from the atmosphere was during high solar radiation and warm temperatures (dark blue shading, Fig. 2.2), and the variation of NEE was stronger with respect to R than with respect to T. In the summer, low solar radiation at night corresponded to respiration of CO_2 into the atmosphere at all temperatures.

As indicated in Table 2.3, the max solar radiation at the Harvard Forest was 605 W m^{-2} for December-February (DJF) and 887 W m^{-2} for June-August (JJA). The interpolation populated data

up to 1,000 W m^{-2}. Similarly, the temperature in DJF (JJA) ranged from -19 to 19°C (3 to 41 °C) at Harvard Forest, and the lookup tables were populated from -20 to 40°C for all seasons via nearest-neighbor interpolation to accommodate the Salt Lake Valley limits of -20 to 41° (Table 2.3 and 2.4).

2.3.6.2 Mead Croplands

Slices through the Mead Croplands lookup table for an illustrative winter and summer day are shown in Fig. 2.3. The pattern was similar to the Harvard Forest NEE pattern, but a slightly larger seasonal amplitude. Specifically, reduced solar radiation and colder temperatures during winter supported near-zero NEE (Fig. 2.3a), and increased solar radiation and warmer temperatures enabled the crops to sequester substantial CO_2 (large negative NEE at almost all temperatures in Fig. 2.3b). In the evening through the early morning, zero to low solar radiation limited potential photosynthesis, and respiration was the dominant flux of CO_2 out of the system into the atmosphere. NEE in the winter was slightly positive, reflecting plant and soil respiration (Fig. 2.3a). NEE in the summer was large and negative during the day, and respiration dominated overnight (Fig. 2.3b).

Similar to the Harvard forest, the max solar radiation at Mead Croplands was 702 W m^{-2} during DJF, and was 977 W m^{-2} during JJA, and the interpolation populated data up to 1,000 W m^{-2} (Table 2.3). Similarly, the temperature in DJF (JJA) shown in Table 2.4 ranged from -25 to 19°C (-3 to 33s°C), and the lookup table was interpolated from -20 to 41°C for all seasons to accommodate the Salt Lake Valley limits (Table 2.3 and 2.4).

2.3.6.3 Vaira Brushlands

The Viara Brushlands growing season is primarily in the spring, so Fig. 2.4 shows an illustrative winter and spring day. Because California has a more Mediterranean climate with warmer seasonal temperatures (Table 2.4), photosynthesis can occur during all seasons if photosynthetic reactants are available. Maximum photosynthetic activity occurs during the spring season with the snowmelt from the Sierras (as discussed in Section 2.3.4). Overall, temperatures at Vaira brushlands are much warmer in DJF and MAM than at any of the other AmeriFlux proxy sites or the Salt Lake Valley (Table 2.4).

The minimum (maximum) seasonal temperature was -2°C (42°C). However the lookup table populated temperatures down to -8°C (Table 2.4 and Fig. 2.4a,b). The maximum solar radiation for DJF at Vaira brushlands was 771 W m^{-2}. As discussed for the first two lookup tables, the interpolation depicted in Fig. 2.4 populated data to the Salt Lake Valley temperature and global radiation limits (Table 2.4 and 2.3).

2.3.6.4 Niwot Ridge

The Niwot Ridge lookup table for a representative winter and summer day (Fig. 2.5) shows a pattern broadly similar to the tables described above (Figs 2.2, 2.3, and 2.4). In the winter, there is zero to slightly positive CO_2 flux into the atmosphere (Fig. 2.4a). In the summer, at night, there is respiration, and in the daytime there is a net flux of CO_2 out of the atmosphere (blue shading, Fig. 2.4b). The Niwot Ridge alpine system does not have as strong a photosynthetic flux as the other ecosystems. This could be due in part to the ecology of alpine trees, the age of the trees, and the availability of resources necessary for photosynthesis.

For all seasons, Niwot Ridge experiences higher maximum incoming solar radiation than the other Ameriflux proxy sites (Table 2.3) in part because of its cloud climatology and latitude, but also its elevation (3,050 masl compared with the Salt Lake Valley (SLV) at 1,286 masl, Harvard forest at 340 masl, Mead Croplands at 333 masl, and Vaira brushlands at 129 masl). However, Niwot Ridge is also the coldest of the sites for all seasons (Table 2.4). The Niwot Ridge lookup table is populated beyond the temperature and solar radiation regime of the ecosystem as shown in Fig. 2.5b).

2.3.7 Proxy Ecosystem Model Performance

To assess the performance of each lookup table, we evaluated its ability to simulate one year of AmeriFlux NEE withheld from the construction of the lookup table. The agreement between the AmeriFlux data and the output from the lookup table was quantified using the squared Pearson correlation coefficient (r^2; Table 2.1), which indicated the fraction of variance accounted for.

2.3.7.1 Harvard Forest

The Harvard Forest lookup table accounted for 64% of the hourly NEE variability observed at the corresponding AmeriFlux site during a year withheld from the table development (Fig. 2.6; Table 2.1). During the winter months, NEE was slightly positive due to respiration. During spring through fall, there was sufficient photosynthetically active radiation and water for photosynthesis to occur, supporting much larger negative NEE.

2.3.7.2 Mead Croplands

The Mead Croplands lookup table accounted for 79% of the hourly NEE variability observed at the corresponding AmeriFlux site during a year withheld from the table development (Fig. 2.7; Table 2.1). The Mead Croplands had a slightly shorter growing season than Harvard Forest. At the height of the growing season, Mead Croplands had almost twice of the flux of CO_2 into the biosphere as the Harvard Forest did (compare Figs. 2.6 and 2.7).

2.3.7.3 Vaira Grasslands

Unlike the other Ameriflux proxy ecosystems, the Vaira Grasslands growing season ran from October through May as seen in Fig. 2.8, and the lookup table accounted for 78% of the hourly NEE variability for a year withheld from the table development (Fig. 2.8; Table 2.1). The lookup table captured some of the interesting early winter variations of NEE (days of year 275-325, Fig. 2.4 and 2.8).

2.3.7.4 Niwot Ridge Forest

The Niwot Ridge lookup table accounted for 57% of the hourly variability of the corresponding AmeriFlux NEE data for a year withheld from the table development (Fig. 2.9; Table 2.1). The growing season during which the forest sequesters CO_2 is similar to Harvard Forest's growing season. The relatively low r^2 for Niwot Ridge arose in part because the lookup table failed to capture the strongest negative NEE values that occurred during the growing season, suggesting that this strong CO_2 uptake was tied to factors not included in our ($d \times T \times R$) space (e.g., moisture variables including precipitation history).

2.3.8 Application of Lookup Tables

To use the lookup tables corresponding to the ecosystem in a given model box, three quantities were determined for each model box at each time step in the simulation: air temperature (T), day of year, and incoming solar radiation. T was estimated by linear interpolation of hourly observations at the Salt Lake City International Airport.

The estimate of incoming solar radiation for the Salt Lake Valley began with an equation for clear-sky solar irradiance (K_o^+)

$$K_o^+ = a_1 \sin\phi + a_2, \tag{2.3}$$

where ϕ was solar elevation angle computed at each model time step for the latitude, longitude, and elevation of Salt Lake City. The constants $a_1 = 1090$ W m^{-2} and $a_2 = -65$ W m^{-2} were turbidity coefficients representative for North America (Holstag and Ulden, 1983).

Next, the global radiation (R) was estimated by adjusting K^+ for cloud cover

$$R = K_o^+(1 + b_1 N^{b_2}), \tag{2.4}$$

where empirical coefficients $b_1 - 0.75$ and $b_2 = 3.4$ were based on field measurements (Holstag and Ulden, 1983), and N was the total cloud cover derived from surface observations at the Salt Lake City International Airport (Table 2.5). Querying the lookup tables with day of year, T, and R as defined above yielded the composite diel cycles of Q_b shown for each season in Fig. 2.10i-l.

2.4 Model Inputs and Sensitivity Tests

The previous section described the development ion of the biological flux (Q_b) used as an input for the multiple-box model. The anthropogenic flux, Q_a was adapted from the Vulcan dataset (Gurney et al., 2009) by introducing an empirical adjustment for air temperature-driven variations in natural gas combustion as detailed in (Strong et al., 2011). The wind speed input fields were developed using data from 16 sites within the MesoWest data archive (Horel et al., 2002; Strong et al., 2011). For the entrainment input terms, mixing depth was determined using the "parcel" method (Holzworth, 1967; Miller, 1967) that set h to the height at which the dry adiabatic lapse rate from the hourly surface air temperature intersected the temperature profile of the morning rawinsondes launched from the Salt Lake City International Airport (Strong et al., 2011). A harmonic fit to the rural Kennecott CO_2 data was used as the horizontal boundary condition and upper boundary condition C_h in Eq. 2.2 as discussed in detail in Chapter 3.

Figure 2.10 depicts the composite diel cycles of the model input fields averaged across grid cells containing the uSLV measurement sites (sites 1-5, 2.1a). On average for all seasons, the biosphere provided a net positive CO_2 flux into the atmosphere during hours without light (Q_b, Fig. 2.10 i-l). The biosphere in the summer was a very large net sink of CO_2 from the atmosphere, but the inversely correlated deepening of the mixing depth (h, Fig. 2.10a-d) cancelled out much of this effect (Chapter 3; also Strong et al., 2011). Anthropogenic fluxes into the atmosphere were largest in the winter due to natural gas heating. Wind speed and direction had the largest diurnal variation in the summer (JJA) and captured the diel rotation from down-valley in the morning to up-valley flow in the afternoon.

To evaluate the importance of flux specifications, sensitivity tests were performed with the multiple-box model. It was found that the diel cycle of carbon dioxide responds importantly to all terms, yet depended most heavily on the anthropogenic flux and the contemporaneous evolution of the mixed layer depth. Figure 2.11 shows results from a sensitivity test in which Q_a was set to zero and a sensitivity test in which Q_a and Q_b were both set to zero. The biological flux became the dominant source of CO_2 when the anthropogenic flux was removed from the model (green curve, Fig. 2.11). With neither a biological nor anthropogenic flux, the simulation reduced to the boundary condition CO_2 concentration, which in this model was prescribed as a harmonic fit to the Kennecott site data (blue curve, Fig. 2.11).

Wind and mixing height sensitivity tests were also performed, but not shown. The winds played a large role in maintaining realistic CO_2 concentrations in the model. Without advection effects, the seasonal cycle of CO_2 was still discernible, but concentrations within the uSLV quickly reached extremely unrealistic levels.

Mixing heights also played an essential role in regulating seasonal and diel cycles of CO_2 within the uSLV. Without mixed layer growth, the biological flux still removed CO_2 from the atmosphere during the summer, but concentrations nonetheless rose continuously until they caused numerical instabilities within the model.

2.5 Conclusions and Discussion

Strong et al. (2011) developed a multiple-box model to investigate how biological, anthropogenic, and meteorological processes combine to create the diel cycles of CO_2 mole fraction within the urban Salt Lake Valley all hours of all seasons. The biological flux input for the Strong et al. (2011) multiple-box model was developed by first creating Net Ecosystem Exchange (NEE, Q_b) lookup tables from Ameriflux proxy ecosystems chosen to represent Salt Lake Valley ecosystems. Lookup tables were based on air temperature, solar radiation, and day of year. During the simulations, the lookup tables were queried with solar radiation (based on solar angle and observed cloud fraction), air temperature, and day of year for each model box at each time step. The lookup tables accounted for between 57 and 79% of the hourly variance of the corresponding AmeriFlux NEE data for years withheld from the table development, and the tables underestimated some of the largest-amplitude NEE diel cycles because the tables were constructed from data averaged into cells of the table.

Among the measured variables within the AmeriFlux network, the Net Ecosystem Exchange (NEE) was best explained by variance in solar radiation and surface air temperature. The dependence of NEE on incoming solar radiation and air temperature most realistically accounted for the hourly variance of the NEE cycles for the Vaira Grasslands (78%) and the Mead Croplands (79%), neither of which are classified as trees. The Mead Croplands were irrigated and most likely fertilized allowing the system to be water-saturated and nitrogen-rich. Similarly, the Vaira grasslands were fed by runoff from the Sierra Nevada Mountains, may receive nitrogen-rich runoff from the agricultural land to the north in the Sacramento Valley, and were on disturbance-free private property.

Alternatively, solar radiation and temperature explained 57% of the hourly variance of NEE for Niwot Ridge evergreen needle-leaf forest and 64% of the hourly variance of NEE for the Harvard deciduous broadleaf forest. Considering processes on a range of time scales, the CO_2 flux in these forests could depend on one or a number of the following controls: disturbance by fire or humans, soil resources, plant functional type, water limitation, small leaf area, limited nitrogen, limited season length, and limited atmospheric CO_2 mole fractions. Both forests are mature-to-old stands (80.5 years mean stand age for Harvard Forest and 98 years for Niwot Ridge [estimated in 2008]) which could potentially decrease the magnitude of photosynthetic flux.

Similar to Strong et al. (2011), Reid and Steyn (1997) created a biological flux first by perform-

ing a surface survey of vegetation types and their area. Unlike Strong et al. (2011), Reid and Steyn (1997) averaged together the results from previous above-canopy diurnal net exchange studies in a similar climate over grass, coniferous, and deciduous communities. Reid and Steyn (1997) used multiple net ecosystem exchange sites and studies, and included data from before 1997 in three of the four proxy ecosystems used in Strong et al. (2011): Vaira Grasslands (Xu and Baldocchi, 2004), the Harvard Forest (Wofsy et al., 1993), and the Mead Croplands (Verma et al., 2005). Reid and Steyn (1997) averaged the various ecosystems together to smooth out marked spatial variability between and within the ecosystems. In contrast, Strong et al. (2011) developed and used separate lookup tables for each ecosystem type.

The Q_b specification presented here assumed sufficient similarity between the proxy ecosystem and the local ecosystem in terms of water availability, elevation, soil type, vegetation age, vegetation density, and vegetation diversity. The Harvard Forest-based Q_b lookup table was scaled by 0.5 (Table 2.1) to account for differences in vegetation density and hence NEE (McPherson and Simpson, 1999; Nowak et al., 2002) – a scaling to which overall model performance was not overly sensitive.

For every season except winter, the composite ecosystems started photosynthesizing slightly before sunrise between 5:00-7:00 LST and stopped near sunset between 18:00-20:00 LST (Q_b; Fig. 2.10). In the nighttime hours, and in the winter the composite ecosystem averaged as a source of CO_2 into the atmosphere (Fig. 2.10i). The anthropogenic flux, Q_a, always represented a net source of CO_2. The diurnal cycles in Fig. 2.10 showed a three peak daily cycle that occurred during morning rush hour, lunch time, and evening rush hour. The morning and evening rush hours emitted CO_2 into a shallow boundary layer, with results similar to those observed in other urban centers around the world (Gratani and Varone, 2005; Idso et al., 2001, 2002; Kelome et al., 2006; Lichtfouse et al., 2003; Nasrallah et al., 2003; Pataki et al., 2005; Soegaard and Moller-Jensen, 2003; Widory and Javoy, 2003; Zimnoch et al., 2004). The afternoon peak in Q_a was not seen in the urban diel CO_2 mole fractions because the CO_2 was mixed into a deep mixed layer rendering its influence minimal. The same was true for the large biological flux removing CO_2 from the atmosphere in the summertime afternoons: deepening of the mixed layer diluted the effects of the surface biological flux, halving its effect from morning to afternoon during winter, and rendering the surface fluxes nearly ineffectual (Strong et al., 2011). However, mornings and evenings when respiration dominates the biological flux into a shallow mixed layer, the biological flux was of intermediate importance between advection and entrainment (Strong et al., 2011).

The sensitivity tests found that all inputs - anthropogenic flux, biological flux, wind, and mixed layer growth had an impact on the diel cycle of CO_2. Strong et al. (2011) did not aim to separate anthropogenic flux emissions as did many other urban CO_2 studies (Coutts et al., 2007; Gratani

and Varone, 2005; Henninger, 2008; Idso et al., 2001, 2002; Kelome et al., 2006; Koerner and Klopatek, 2002; Moriwaki et al., 2006; Pataki et al., 2005, 2007; Velasco et al., 2005). These studies found traffic volume to be the driving force in both the diel cycle of CO_2 mole fraction (morning and evening rush hour traffic emissions into a shallow mixed layer) and the increased CO_2 mole fractions with respect to the surrounding rural areas. Some studies found that vegetation helped moderate and reduce daytime CO_2 fluxes (Coutts et al., 2007; Strong et al., 2011; Velasco et al., 2005). However, one study in Krakow, Poland reported that the dominant source of CO_2 in summer nights was the local biosphere (Zimnoch et al., 2004), and that CO_2 emissions from the biosphere caused nighttime mole fraction to rise as much as anthropogenic CO_2 emissions would cause the urban CO_2 mole fractions to rise in the winter. Considering the Vulcan data used here to develop Q_a, the dominant factors producing anthropogenic CO_2 flux in the uSLV were traffic, residential natural gas heating, and industrial sources (Gurney et al., 2009; Wofsy et al., 2010).

As discussed in Strong et al. (2011), uncertainties in this modeling method stem from the assumptions and simplifications in the modeling framework, uncertainties in the input data sets, and the methods used to process the input data. The multiple-box model assumed a homogeneity of CO_2 mole fraction within each 10×10-km box. Each box was assigned an ecosystem type based on the most prominent ecosystem within the box. The biological flux can vary spatially depending on ecosystem type, water availability, density of biomass and control variables such as nitrogen and water availability and soil type. The model did not resolve large-scale synoptic variations in CO_2, but did include a trend and hemispheric annual cycle in its boundary conditions.

Refinements are planned for the next version of this modeling system, but the current model captures the essential temporal features of the uSLV CO_2 cycles on diel and seasonal time scales (Strong et al., 2011). Consistent with findings of earlier studies (Idso et al., 2002; Koerner and Klopatek, 2002; Pataki et al., 2007), the model results indicate that the biological processes contributing to the Net Ecosystem Exchange exert a prominent influence during certain hours, but are the least important contributing factor to overall CO_2 mole fraction in the uSLV. While there are many reasons to plant trees for energy-efficiency, carbon sequestration, shading, and aesthetics (McPherson and Simpson, 1999), the multiple-box model results do not support the notion that the urban-forest carbon sink within the Salt Lake Valley largely offsets extensive emissions from fossil fuel combustion (Strong et al., 2011). Additional model runs and sensitivity tests are planned to investigate the effects of potential changes in human factors including traffic patterns, traffic volume, green infrastructure, clean fuels, and urban planning, and such simulations are anticipated to be of value for urban researchers and policy makers.

Reasons motivating increased research attention on urban carbon dynamics include rapid and

extensive urban expansion, population growth, and increasing release of greenhouse gases and pollutants. There are international efforts leading to world education and understanding of the global carbon cycle (Ciais et al., 2010; IPCC, 2007), and regional efforts at the urban scale provide detailed information for evaluating consequences of changes in human behavior on CO_2 emissions (Pataki et al., 2009; Strong et al., 2011). The results of the Strong et al. (2011) modeling study indicated that the multiple-box modeling framework and inputs used can provide a foundation for testing CO_2 emission scenarios and human behavioral changes on urban and potentially larger spatial scales.

The Salt Lake Valley is leveraged into several national-level resources that will enhance future CO_2 research. Salt Lake City is a member of the C40 CITIES Climate Initiative (http://www.c40cities.org/) aiming for a meaningful impact on greenhouse gas emissions and climate risks. There is a planned National Ecological Observatory Network (NEON) site within the Salt Lake Valley (http://neoninc.org), and data from that site will provide enhanced opportunities for the testing and development of CO_2 modeling frameworks. Finally, plans are being made for an expanded observational network, including some measurements of CO_2 flux, supported by the National Science Foundation Experimental Program to Stimulate Competitive Research (http://utepscor.org/).

2.6 Appendix

This Appendix describes how the multiple-box model's system of equations (2.2) was set up as a matrix inversion problem by Strong et al. (2011). Using a superscript to denote time, using a subscript to denote space, and averaging the right hand side of (2.2) over times j and $j+1$, the finite difference form of each term away from the edges of the domain was

$$\frac{\partial C_i}{\partial t} = \frac{C_i^{j+1} - C_i^j}{\Delta t} \tag{2.5}$$

$$\frac{Q_i}{h} = \frac{1}{2}\left(\frac{Q_i^{j+1}}{h^{j+1}} + \frac{Q_i^j}{h^j}\right) \tag{2.6}$$

$$-u_i\left(\frac{\partial C}{\partial x}\right)_i = -\frac{1}{2}\left[u_i^{j+1}\left(\frac{C_{i+1}^{j+1} - C_{i-1}^{j+1}}{2\Delta x}\right) + u_i^j\left(\frac{C_{i+1}^j - C_{i-1}^j}{2\Delta x}\right)\right] \tag{2.7}$$

$$-v_i\left(\frac{\partial C}{\partial y}\right)_i = -\frac{1}{2}\left[v_i^{j+1}\left(\frac{C_{i-nx}^{j+1} - C_{i+nx}^{j+1}}{2\Delta x}\right) + v_i^j\left(\frac{C_{i-nx}^j - C_{i+nx}^j}{2\Delta x}\right)\right] \tag{2.8}$$

$$\frac{1}{h}\frac{\partial h}{\partial t}(C_h - C_i) = \frac{1}{2}\left[\frac{1}{h^{j+1}}\frac{\partial h^{j+1}}{\partial t}\left(C_h^{j+1} - C_i^{j+1}\right) + \frac{1}{h^j}\frac{\partial h^j}{\partial t}\left(C_h^j - C_i^j\right)\right] \tag{2.9}$$

where (2.6-2.9) represent averages of the finite differences at time j and $j+1$. Substituting (2.5-2.9) into (2.2) and rearranging so that all the unknown terms (those involving C_i^{j+1}) are on the left hand side,

$$\left(1+\frac{\Delta t}{2h^{j+1}}\frac{\partial h^{j+1}}{\partial t}\right)C_i^{j+1}+\frac{\Delta t}{4\Delta x}\left[u_i^{j+1}\left(C_{i+1}^{j+1}-C_{i-1}^{j+1}\right)+v_i^{j+1}\left(C_{i-n_x}^{j+1}-C_{i+n_x}^{j+1}\right)\right]= \tag{2.10}$$

$$\left(1-\frac{\Delta t}{2h^{j}}\frac{\partial h^{j}}{\partial t}\right)C_i^{j}-\frac{\Delta t}{4\Delta x}\left[u_i^{j}\left(C_{i+1}^{j}-C_{i-1}^{j}\right)+v_i^{j}\left(C_{i-n_x}^{j}-C_{i+n_x}^{j}\right)\right]+$$

$$+\frac{\Delta t}{2}\left[\frac{C_h^{j+1}}{h^{j+1}}\frac{\partial h^{j+1}}{\partial t}+\frac{C_h^{j}}{h^{j}}\frac{\partial h^{j}}{\partial t}\right]+\frac{\Delta t}{2}\left(\frac{Q_i^{j+1}}{h^{j+1}}+\frac{Q_i^{j}}{h^{j}}\right) \tag{2.11}$$

which can be written compactly in matrix-vector form as

$$\mathsf{G}\vec{C}^{j+1}=\mathsf{H}\vec{C}^{j}+\vec{B}. \tag{2.12}$$

Equation (2.12) was a set of n linear equations in the n unknowns $\vec{C}^{j+1}$, with G and H being known $(n\times n)$ matrices, and $\vec{C}^{j}$ and $\vec{B}$ being known $(n\times 1)$ vectors. The solution to (2.12) was obtained via matrix inversion

$$\vec{C}^{j+1}=\mathsf{G}^{-1}\left(\mathsf{H}\vec{C}^{j}+\vec{B}\right). \tag{2.13}$$

In equation (2.12), G was an $(n\times n)$ sparse matrix. To illustrate how the elements of this matrix were defined, a hypothetical smaller spatial domain with $n_x=4$ and $n_y=5$ is shown in the left panel of Fig. 2.12. The grid points in this domain are numbered $i=1,\ldots,n_xn_y$, and the right panel of Fig. 2.12 has letters indicating the row-column positions of non-zero elements of G. The diagonal elements (D) operated on C_i^{j+1}. The upper diagonal elements (E) operated on the node to the east (C_{i+1}^{j+1}) and had a zero entry where C_{i+1}^{j+1} had the boundary condition C_h to its east (upper diagonal elements $k\times n_x, k=1,2,\ldots,n_y-2$). The lower diagonal elements (W) operated on the node to the west (C_{i-1}^{j+1}) and had a zero entry where C_i^{j+1} had the boundary condition C_h to its west (lower diagonal elements $k\times n_x, k=1,2,\ldots,n_y-2$).

The upper band elements (S) were situated n_x columns to the right of the diagonal and operated on the node to the south $(C_{i+n_x}^{j+1})$. The lower band elements (N) were situated n_x columns to the left of the diagonal and operated on the node to the north $(C_{i-n_x}^{j+1})$. Rows of G for which C_i^{j+1} has the boundary condition C_h to its north (rows $1,2,\ldots,n_x$) lacked the element N, and rows of G for which C_i^{j+1} had the boundary condition C_h to its south (rows $n-n_x+1, n-n_x+2,\ldots,n$) lacked the element S.

Values of the non-zero elements of G were

$$D = 1+\frac{\Delta t}{2h^{j+1}}\frac{\partial h^{j+1}}{\partial t} \tag{2.14}$$

$$E = \frac{\Delta t}{4\Delta x}u_i^{j+1} \tag{2.15}$$

$$W = -E \tag{2.16}$$

$$N = \frac{\Delta t}{4\Delta x}v_i^{j+1} \tag{2.17}$$

$$S = -N. \tag{2.18}$$

The non-zero elements of the matrix H were collocated with those of G and were given by

$$D = 1 - \frac{\Delta t}{2h^j}\frac{\partial h^j}{\partial t} \tag{2.19}$$

$$W = \frac{\Delta t}{4\Delta x}u_i^j \tag{2.20}$$

$$E = -W \tag{2.21}$$

$$S = \frac{\Delta t}{4\Delta x}v_i^j \tag{2.22}$$

$$N = -S. \tag{2.23}$$

Elements $i = 1,2,\ldots,n$ of the vector $\vec{B}$ on the right hand side of (2.12) were

$$B_i = \frac{\Delta t}{2}\left(\frac{Q_i^{j+1}}{h^{j+1}} + \frac{Q_i^j}{h^j} + \frac{C_h}{h^{j+1}}\frac{\partial h^{j+1}}{\partial t} + \frac{C_h}{h^j}\frac{\partial h^j}{\partial t}\right) + \hat{B}_i. \tag{2.24}$$

where $\hat{B}_i$ depended on the configuration of boundary conditions adjacent to the grid point. For interior grid points with no boundary conditions, $\hat{B}_i = 0$. To indicate values of $\hat{B}_i$ for a grid point with an adjacent boundary condition, notation $C_\uparrow, C_\downarrow, C_\rightarrow, C_\leftarrow$ represents the value of the boundary condition adjacent to grid point i in, respectively, the model's positive y-direction, negative y-direction, positive x-direction, and negative x-direction. An "edge" was defined as the set of non-corner grid points adjacent to a model boundary. For the edge at the model's positive y-direction (points $i = 2,\ldots,n_x - 1$)

$$\hat{B}_i = -\frac{\Delta t}{4\Delta x}\left(v_i^j C_\uparrow^j + v_i^{j+1} C_\uparrow^{j+1}\right). \tag{2.25}$$

For the edge at the model's negative y y-direction (points $i = n - nx + 2,\ldots,n-1$)

$$\hat{B}_i = \frac{\Delta t}{4\Delta x}\left(v_i^j C_\downarrow^j + v_i^{j+1} C_\downarrow^{j+1}\right). \tag{2.26}$$

For grid points with an adjacent boundary condition in only the positive x-direction ($i = 2n_x, 3n_x, \ldots, (n_y - 1)n_x$)

$$\hat{B}_i = -\frac{\Delta t}{4\Delta x}\left(u_i^j C_\rightarrow^j + u_i^{j+1} C_\rightarrow^{j+1}\right). \tag{2.27}$$

For grid points with an adjacent boundary condition in only the negative x-direction ($i = 1n_x + 1, 2n_x + 1, \ldots, (ny-2)n_x + 1$)

$$\hat{B}_i = \frac{\Delta t}{4\Delta x}\left(u_i^j C_\leftarrow^j + u_i^{j+1} C_\leftarrow^{j+1}\right). \tag{2.28}$$

Corner grid points were treated by using combinations of (2.25-2.28).

Table 2.1. The vegetation types assigned to model boxes, the proxy ecosystem in the AmeriFlux network used to develop the Q_b lookup table, the fraction of hourly variance in the proxy ecosystem accounted for by the lookup table based on a year of withheld data, and any scaling applied to the Q_b lookup table.

Model vegetation type	AmeriFlux proxy	r^2	scaling factor
Brushland	Vaira Brushland (Xu and Baldocchi, 2004)	0.80	0.0
Cropland	Mead Cropland (Verma et al., 2005)	0.78	0.0
Forest	Niwot Ridge (Monson et al., 2005)	0.57	0.0
Residential	Harvard Forest (Wofsy et al., 1993)	0.64	0.5
Wetland	Mead Cropland (Verma et al., 2005)	0.78	0.0

Table 2.2. Correlation coefficients for predictors of Net Ecosystem Exchange for the four AmeriFlux sites used as proxy ecosystems in (Strong et al., 2011). Correlations were averaged over years used to make the lookup tables.

Predictor	Harvard	Mead	Niwot Ridge	Vaira
global radiation	-0.69	-0.59	-0.66	-0.42
air temperature	-0.39	-0.30	-0.26	-0.11
vapor pressure deficit	-0.38	-0.42	-0.28	-0.05
precipitation	-0.01	-0.00	0.05	-0.04
soil temperature	-0.26	-0.27	-0.14	-0.00
latent heat flux	-0.63	-0.86	-0.65	-0.78

Table 2.3. Seasonal maxima of solar radiation in W m^{-2} for AmeriFlux proxy sites and the Salt Lake Valley (SLV).

Months	SLV	Harvard	Mead	Niwot Ridge	Vaira
December-February	658	605	702	813	771
March-May	971	864	1022	1132	1001
June-August	983	887	977	1140	1051
September-November	862	717	855	1017	922

Table 2.4. Seasonal maxima and minima of air temperature in Celsius for the AmeriFlux sites and Salt Lake Valley (SLV).

Months	min/max	SLV	Harvard	Mead	Niwot Ridge	Vaira
December-February	min	-19	-18	-25	-25	-2
	max	19	17	19	6.3	27.5
March-May	min	-9	-12	-11	-18	0
	max	37	26	32	15	33
June-August	min	3	8	10	-3	7
	max	41	32	37	22	42
September-November	min	-14	-4	-13	-17	0
	max	36	24	37	18	38

Table 2.5. Conversion of airport cloud observations to fractional cloud coverage for use in equation (2.4).

Observation	description	cloud fraction (eighths)
CLR	clear	0
SCT	scattered	2.5
BKN	broken	6
OVC	overcast	8

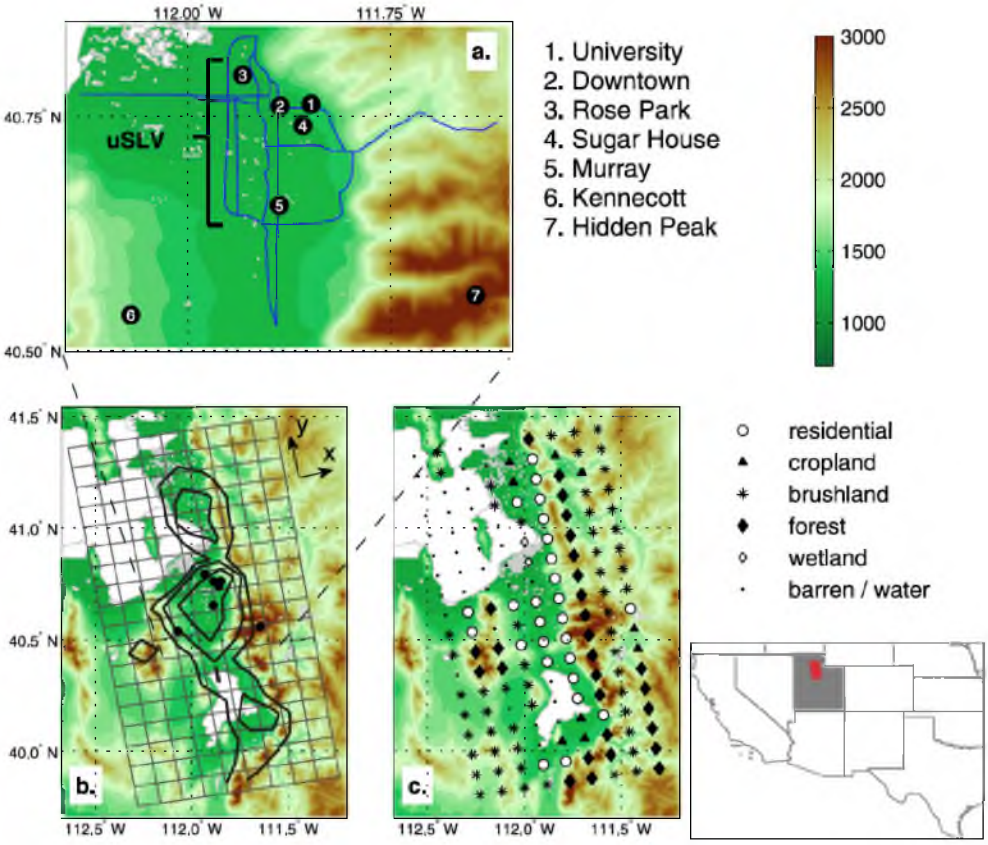

Figure 2.1. The domain of the multiple box model is depicted here. The map at the bottom right shows the southwestern United States with Utah shaded gray and the model domain shaded red. In (a-c), shading indicates elevation in meters, and water is white with the Great Salt Lake toward the top left. (a) The Salt Lake Valley is shown. Blue lines are interstate highways, and numbered circles indicate measurement sites named to the right [sites 1-5 make up the urban Salt Lake Valley (uSLV)]. (b) The region surrounding the Salt Lake Valley is shown with a grid indicating the edges of each 10×10-km model box, arrows indicating the model x direction and y direction, filled circles indicating the seven measurement sites in (a), and dashed lines indicating where the corners of (a) align with (b). Annual mean anthropogenic CO_2 emissions are shown with units 10^7 kg m^{-2} s^{-1} at three contour levels: 0.25, 1, and 3. (c) The vegetation type assigned to each model box is indicated by a symbol as shown in the legend to the right. Adapted from Figure 1 in Strong et al. (2011).

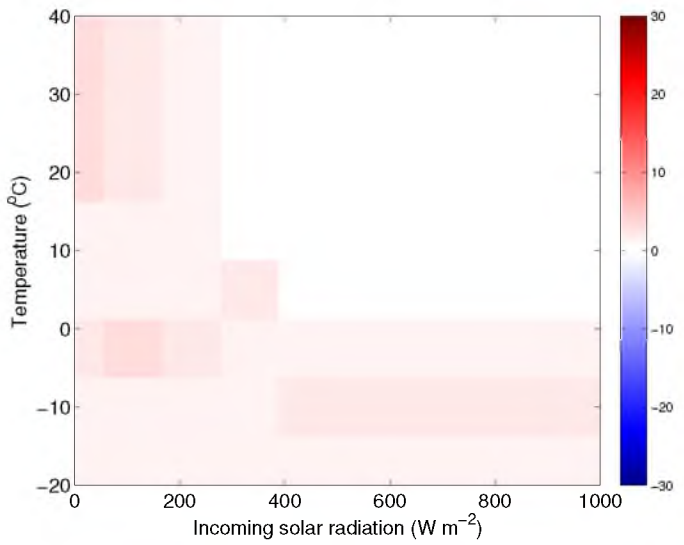

(a) January 15

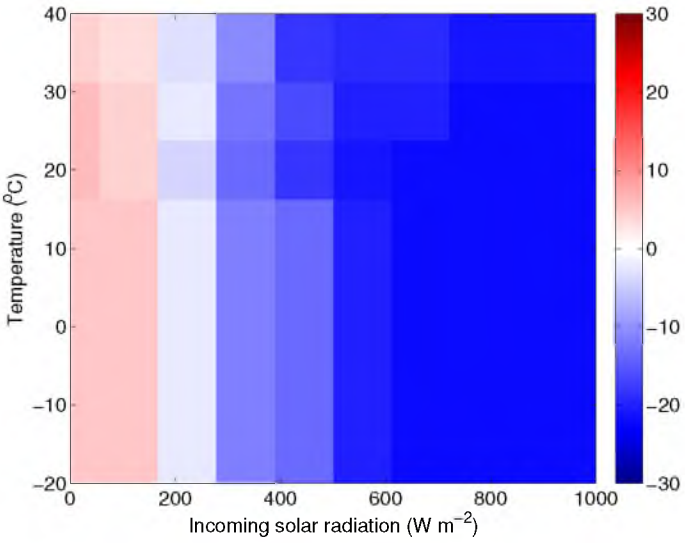

(b) July 13

Figure 2.2. Illustrative slices through the Harvard Forest lookup table representing the Net Ecosystem Exchange (μmol m^{-2}) for (a) 15 January and (b) 13 July.

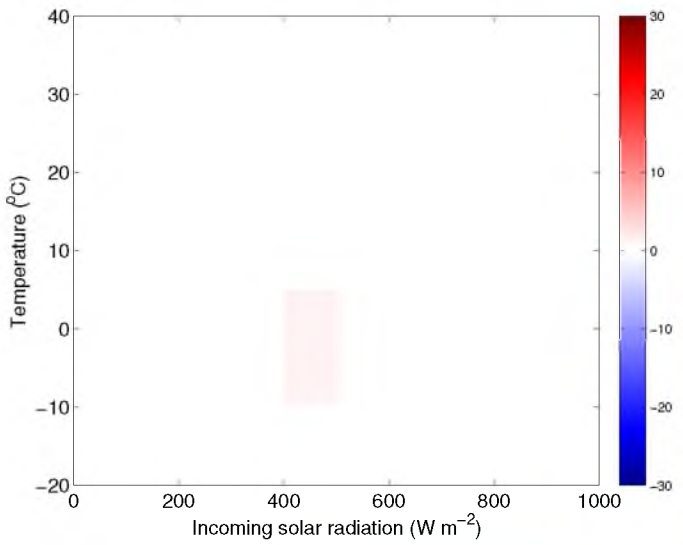

(a) January 15

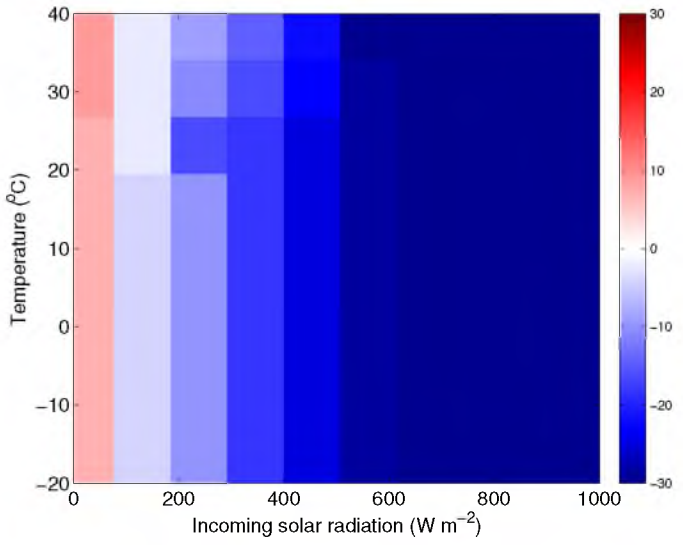

(b) July 13

Figure 2.3. Illustrative slices through the Mead Croplands lookup table representing the Net Ecosystem Exchange (μmol m^{-2}) for (a) 15 January and (b) 13 July.

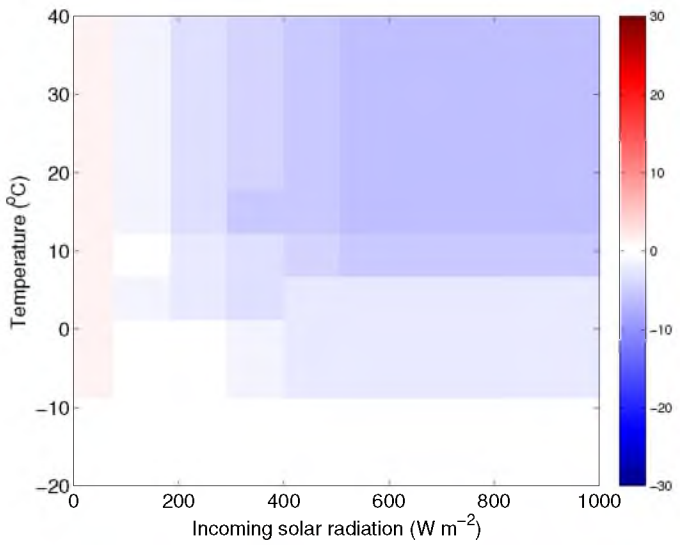

(a) January 15

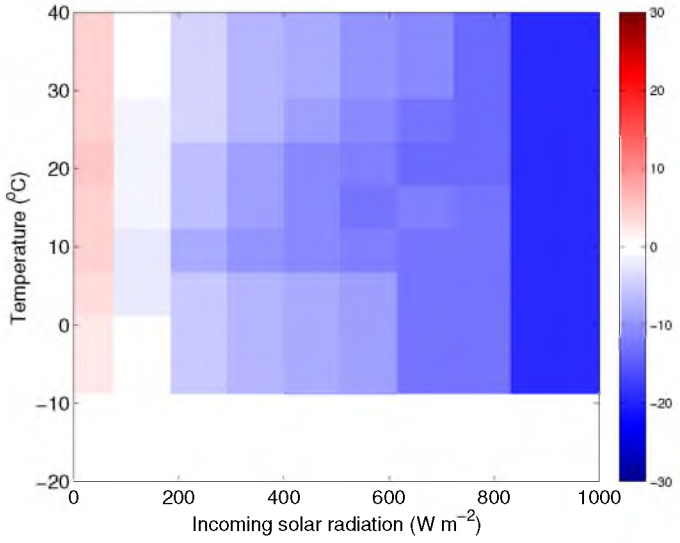

(b) March 15

Figure 2.4. Illustrative slices through the Viara Brushlands lookup table representing the Net Ecosystem Exchange (μmol m^{-2}) for (a) 15 January and (b) 13 July.

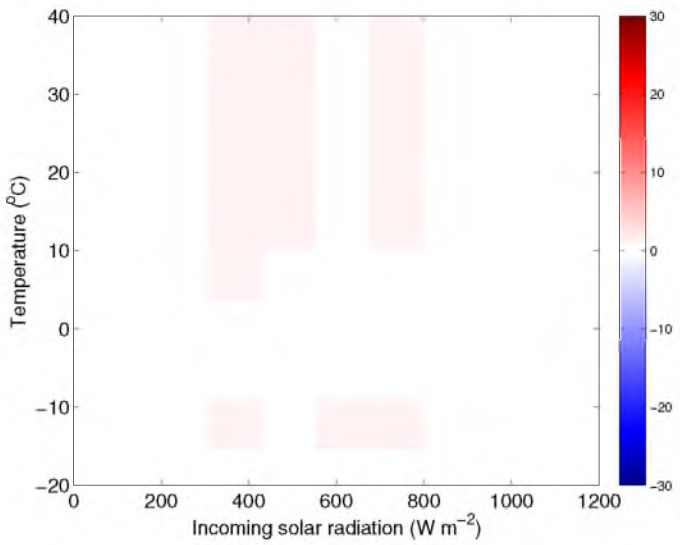

(a) January 15

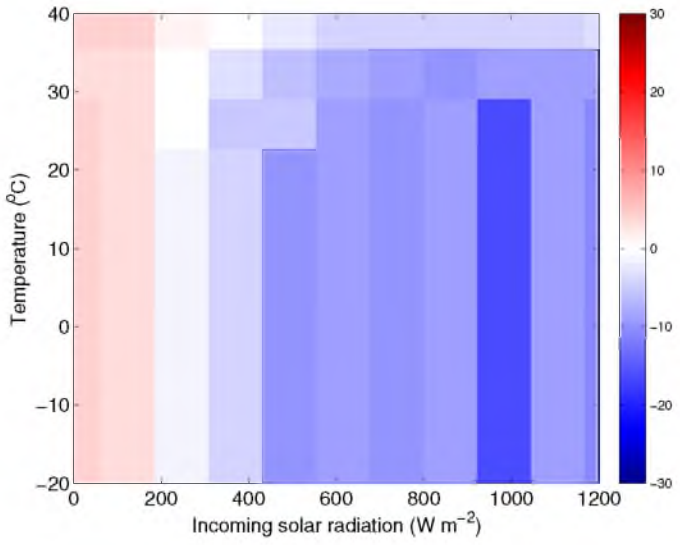

(b) July 13

Figure 2.5. Illustrative slices through the Niwot Ridge lookup table representing the Net Ecosystem Exchange (μmol m^{-2}) for (a) 15 January and (b) 13 July.

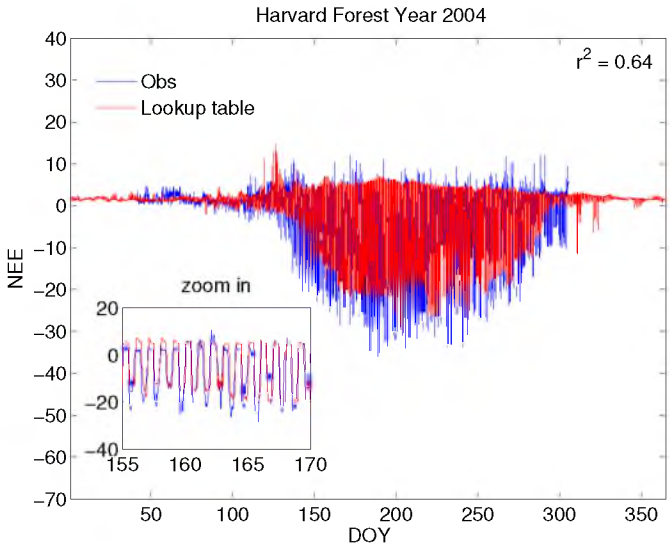

Figure 2.6. Harvard Forest lookup table performance for 2004. The Net Ecosystem Exchange measured at the Harvard Forest AmeriFlux site (blue curve) and its simulation using the lookup table (red curve). The time axis is day of year (DOY), and the inset figure widens the time axis for visual inspection.

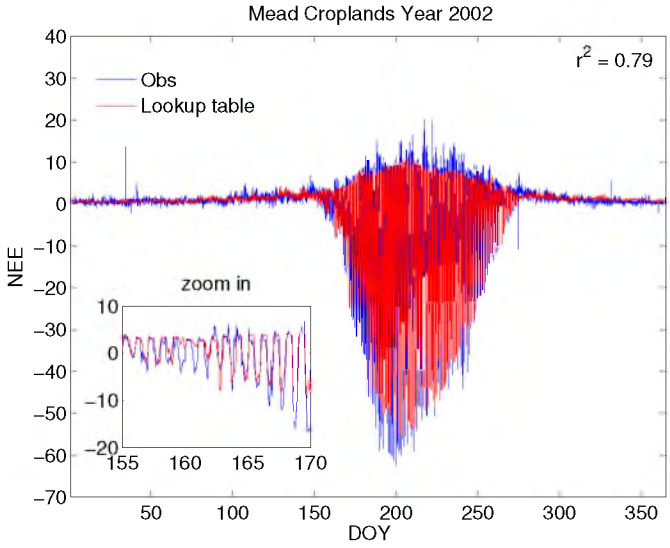

Figure 2.7. Mead Croplands lookup table performance for 2002. The Net Ecosystem Exchange measured at the Mead Croplands AmeriFlux site (blue curve) and its simulation using the lookup table (red curve). The time axis is day of year (DOY), and the inset figure widens the time axis for visual inspection.

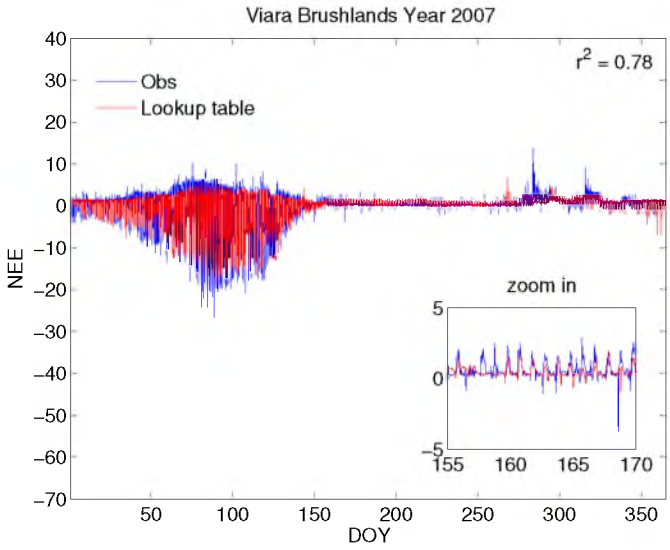

Figure 2.8. Vaira Brushlands lookup table performance for 2007. The Net Ecosystem Exchange measured at the Viara Brushlands AmeriFlux site (blue curve) and its simulation using the lookup table (red curve). The time axis is day of year (DOY), and the inset figure widens the time axis for visual inspection.

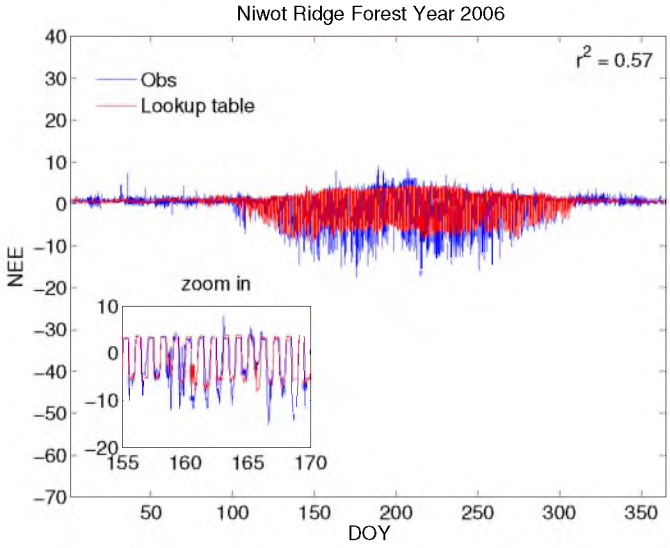

Figure 2.9. Niwot Ridge lookup table performance for 2006. The Net Ecosystem Exchange measured at the Niwot Ridge AmeriFlux site (blue curve) and its simulation using the lookup table (red curve). The time axis is day of year (DOY), and the inset figure widens the time axis for visual inspection.

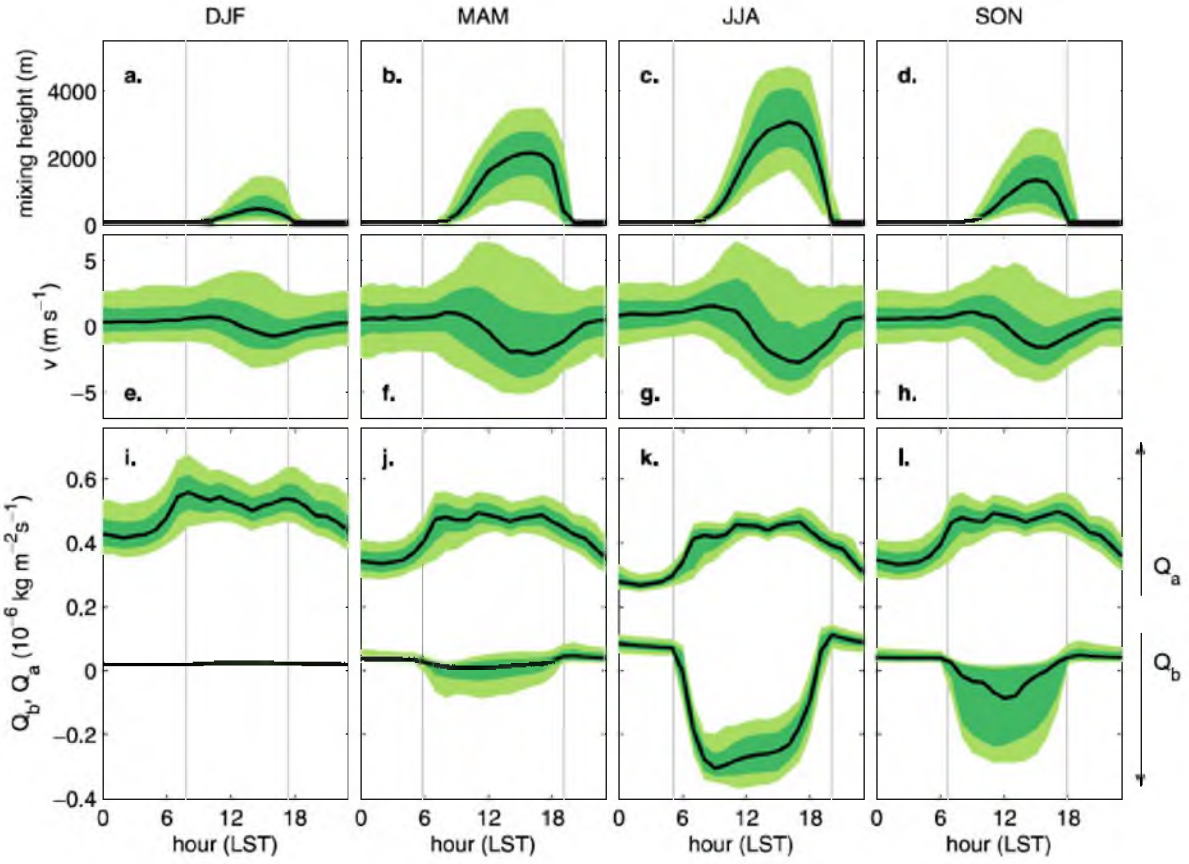

Figure 2.10. Composite diel cycles (local standard time) of model forcing averaged across model boxes containing uSLV measurement sites (sites 1-5, Fig. 2.1a), organized into columns by season: winter (DJF), spring (MAM), summer (JJA), and fall (SON). (a-d) Mixed layer height (h). (e-h) Wind component in model y direction (v). (i-l) Net anthropogenic flux (Q_a) appears as nonnegative curves in the top part of each plot, and net biological flux (Q_b) appears as curves crossing through zero in bottom part of each plot. For each variable, the bold curve is the median, the dark shaded region indicates the 25th to 75th percentiles, and the light shaded region extends to the 10th to 90th percentiles. Vertical lines indicate the time of sunrise and sunset in the middle of each 3 month window. Adapted from Figure 4 in (Strong et al., 2011).

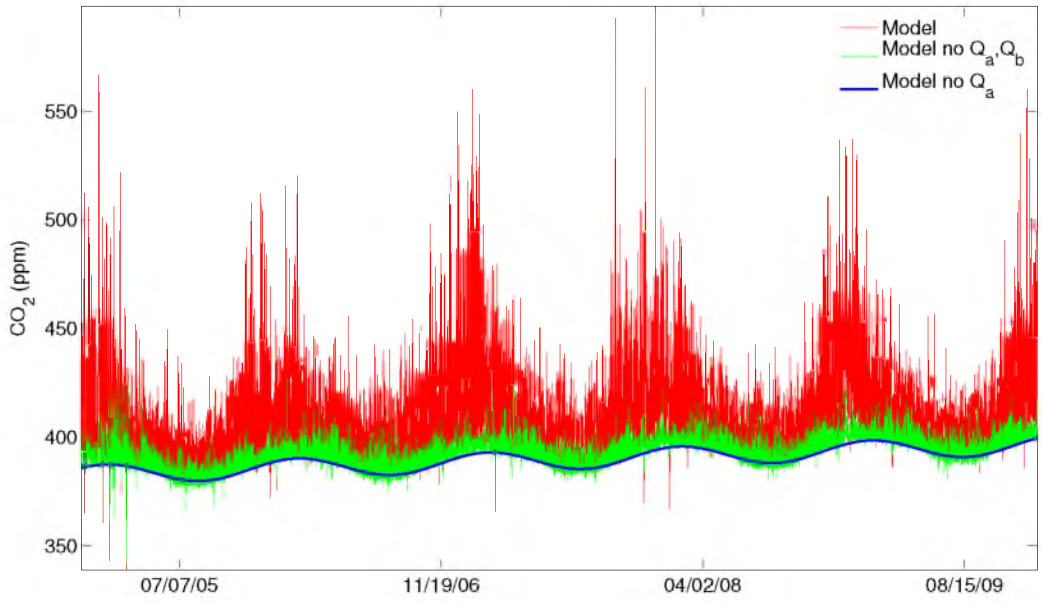

Figure 2.11. Multiple-box model sensitivity tests are shown. The red curve shows output from the multiple-box model as run in Strong et al. (2011). The green curve shows output from a sensitivity test in which the anthropogenic flux (Q_a) was set to zero, and the blue curve shows the smooth harmonic fit to the Kennecott CO_2 data (equivalent to running the model with zero anthropogenic flux and zero biological flux).

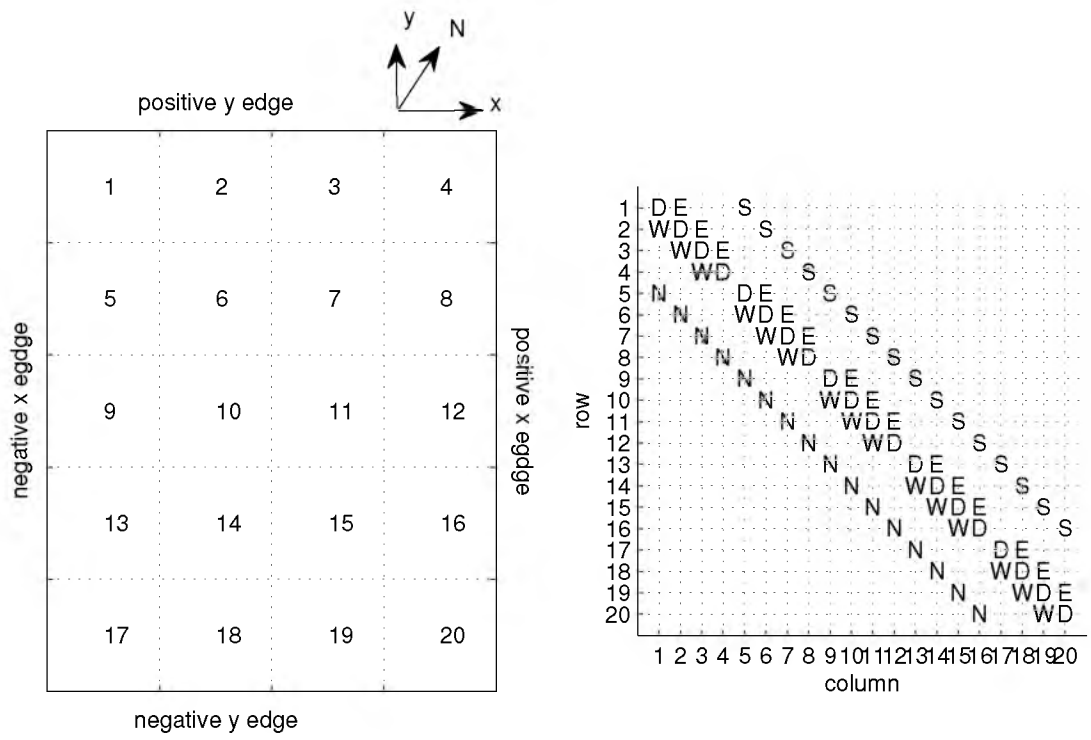

Figure 2.12. Developing the multiple-box model matrix for a simplified domain with $n_x = 4$ and $n_y = 5$, each box is depicted with its value of i for $i = 1, \ldots, n_x n_y$. At the upper right of the figure, N indicates north, and the model positive y-direction is oriented slightly west of north. The edges of the domain are labeled with names based on the positive and negative x and y directions indicated by arrows at the upper right.

CHAPTER 3

CARBON DIOXIDE VARIABILITY IN THE SALT LAKE VALLEY DURING THE PERSISTENT COLD AIR POOL STUDY (PCAPS)

3.1 Abstract

An in-depth observational and modeling study was undertaken to explain the variability of carbon dioxide (CO_2) in the urban Salt Lake Valley (uSLV) during the winter of 2010-2011, corresponding to the Persistent Cold Air Pool Study (PCAPS). A multiple-box model was used to study anthropogenic and meteorological influences on CO_2 variability during the PCAPS period within the uSLV. CO_2 variability was simulated using a multiple-box model forced by surface winds, mixing heights derived from atmospheric soundings, an anthropogenic emissions data set, and an empirical biological flux. The model output was compared with thermodynamic data and ceilometer data from intensive observation periods taken during PCAPS. In addition, an existing multisite network of CO_2 observations was supplemented with quasivertical profiles of CO_2 collected by ascending steep topography on foot or by vehicle.

For the PCAPS period, the multiple-box model accounted for 33% of the variance of the hourly observations and 83% of the variance in the mean diel cycle. Following introduction of an improved parameterization of the residual layer CO_2 concentration, the model increased its performance to account for 45% of the hourly observations. During the winter when wind speeds were low, surface CO_2 variability largely depended on atmospheric stability and to a lesser extent on mixed layer growth. The highest concentrations occurred under cool, clear nights under a strong nocturnal temperature inversion. Moderate concentrations were seen at night below an elevated cloud layer under which CO_2 could mix freely despite consistent nighttime emissions. Low concentrations were found during midday mixing or after cyclonic storms removed CO_2 from the uSLV. Periods of extended high CO_2 mole fractions were sustained by a combination of high anthropogenic emissions, low wind speeds, and low boundary layer growth. Periods of extended low CO_2 mole fractions were sustained primarily by elevated winds and secondarily by greater mixed layer growth.

Increased CO_2 concentrations were seen at the Hidden Peak mountain site shortly after strong wind events in the uSLV.

3.2 Introduction

Wintertime temperature inversions often occur in valleys or basins surrounded by topography that limits outflow and inflow of air via onshore or offshore breezes (Pataki et al., 2005; Whiteman et al., 1999, 2001). Cold air can remain in valleys or basins for days before synoptic forcing erodes or advects the cold air away (Malek et al., 2006; Silcox et al., 2001; Whiteman et al., 1999). Atmospheric pollutants and greenhouse gas emissions can accumulate within the temperature inversion and reach levels above the Environmental Protection Agency's (EPA's) National Ambient Air Quality Standards (NAAQS) (Malek et al., 2006; Silcox et al., 2001).

Urban areas are regions of concentrated population, economic development, transportation, and industrial activity. With 50% of the world population already living in urban areas, and a projected 81% living in urban areas by 2030 (UNFP, 2007), a portion of this population shift will be moving into valleys and basins. Increasing population and the corresponding increase in anthropogenic greenhouse gas and particulate pollution within basins and valleys pose a pressing human and environmental health problem.

3.2.1 Cold-air Pools

Lareau et al. (2012) defined a cold-air pool (CAP) as cold air within a topographic depression when atmospheric conditions initiated processes involving cooling of air near the surface, warming of the air aloft, or both. CAPs are commonly found in mountain basins during all seasons, and are common during periods of light winds, high atmospheric pressure, and low insolation (Lareau et al., 2012; Whiteman et al., 1999). As a result of a CAP, the air becomes stably stratified within the topographic depression and prevents air within the basin from mixing with the atmosphere aloft. Topography surrounding the basin prevents lateral displacement of air and favors stagnant conditions (Lareau et al., 2012).

There are two main classifications of CAPs: *diurnal* and *persistent*. Diurnal CAPs form at night and decay the next morning. Persistent CAPs last for multiple days and are more complex in their structure and dynamics. Diurnal CAPs form from nighttime radiative surface cooling. They decay the next morning with solar input stimulating growth of the boundary layer. They can often be recognized in morning atmospheric soundings as a surface temperature inversion that were absent from the previous evening's atmospheric sounding.

Persistent CAPs are more complex. They can arise due to a variety of atmospheric processes such as differential heating, horizontal and vertical differential temperature advection, and vertical

deformation occurring on a range of timescales (Gillies et al., 2010; Lareau et al., 2012; Reeves and Stensrud, 2009; Whiteman et al., 2001; Wolyn and McKee, 1989; Zong et al., 2001). Although the conditions favoring the development of a persistent CAP are relatively well documented, the physical processes listed above still require additional analysis to understand the exact mechanisms of the evolution process (Lareau et al., 2012).

Surface heating and cooling in the presence of topography can lead to thermally driven flows that influence CAP evolution and transport of pollutants. Drainage flows of warmer upper level air can penetrate the CAP and assist in its breakup (Zangl, 2003). Upslope flow can ventilate polluted and cold air out of the valley or basin into the mountains (de Wekker et al., 2008). These complex flows associated with orography during CAPs present a significant forecasting and modeling challenge.

There are still a limited number of observational and modeling studies that have aimed to document the mechanisms governing CAP evolution despite their societal importance (Gillies et al., 2010; Lareau et al., 2012; Reeves and Stensrud, 2009; Whiteman et al., 2001; Wolyn and McKee, 1989). The thermodynamics governing CAP evolution can have drastic impact on horizontal and vertical distribution of air pollution and greenhouse gas emissions. The complexities and range of scales involved in maintaining and breaking-up CAPs make them difficult to model. Models used in operational weather forecasting generally do not have the formulations or resolution to model small scale turbulent mixing and diffusion which can play a large role in distribution of pollutants. Models used to forecast pollutant concentrations generally parameterize boundary layer evolution, and are continually improved by comparison against observations.

3.2.2 Air Pollution Within Cold-air Pools

Stably stratified air within a topographic depression limits atmospheric mixing. In basins affected by urban growth or development, emissions from vehicles, home heating, factories, and other industrialized sources are emitted into stagnant air within the CAP. It is well known that persistent wintertime temperature inversions within the Intermountain West of the United States result in poor air quality detrimental to human health. These emissions build up within the CAP allowing pollutants to reach levels that often exceed National Ambient Air Quality Standards (NAAQS) (Lareau et al., 2012; Malek et al., 2006; Pataki et al., 2003, 2006; Silcox et al., 2001).

In 1971, the EPA developed NAAQS for several air pollutants including particulate matter of size 10 microns or less (PM10) and particulate matter of size 2.5 microns or less (PM2.5) (Environmental Protection Agency, 1990). Under the current NAAQS for PM, which were last revised in 2006, the 24-hour average of PM10 may not exceeded 150 μg m^{-3} more than once per year on average over any three-year period. PM2.5 may not exceed an annual mean of 15 μg m^{-3},

and three-year average of the 98th percentile of the 24-hour average cannot exceed 35 μg m^{-3} (Environmental Protection Agency, 1990).

The following counties in Utah were designated as nonattainment for regulation of PM2.5 under the NAAQS: Cache County, Weber County, Davis County, Salt Lake County. Salt Lake County and Cache County are especially prone to pollutant trapping under temperature inversions because they are located within mountain basins.

The designation of nonattainment for Logan was in part due to an extreme air pollution event on 15 January, 2004. The 24-hour PM2.5 concentrations were recorded to be 132.5 μg m^{-3}. This was over twice the PM2.5 24-hour standards at the time (65 μg m^{-3} per 1997 NAAQS). The precursors to this day included frequent occurrences of near-surface inversions, surface CAPs, cold temperatures, and lack of precipitation or strong winds. These conditions resulted in stagnant air with minimal tendency for vertical movement (Malek et al., 2006). Malek et al. (2006) raised the point that despite suppressed vertical motion, there could be significant horizontal advection of air pollutants and greenhouse gases within the urban basin.

A recent study in Salt Lake City during wintertime CAPs found that PM2.5 concentrations increased roughly linearly over time at all elevations (from valley floor to 300 m above the floor) during CAP events (Silcox et al., 2001). PM2.5 concentrations were found to be linearly related to the presunrise atmospheric heat deficit in the valley, which is an instantaneous measure of atmospheric stability and CAP strength (Lareau et al., 2012; Silcox et al., 2001). During mix-out events, upper elevations were found to decrease in concentration proceeding lower elevations. In the occurrence of a partial mixout, upper elevations mixed out first, then rebounded up (Silcox et al., 2001).

Steamboat Springs, Colorado is an example of a developing urban ski town, has a current population of slightly more than 12,000, and is located within a valley (U.S. Census Bureau, 2012). Steamboat suffers from temperature inversions that trap pollutants, yet the city was able to control its air pollution issue despite its topography. Cold-air pools combined with wood burning caused the area to reach nonattainment status for PM10 in 1993 (Air Pollution Control Division, 2011). The city council members created a State Implementation Plan (SIP) in 1995 to address these issues. The SIP controlled wood-burning emissions, street sanding, and stationary sources, and created street sweeping requirements. These regulations have markedly improved the air in Steamboat Springs since 1995, and the city is projected to remain in attainment for the NAAQS through 2024 (Air Pollution Control Division, 2011).

3.2.3 CO_2 Wintertime Variability

CO_2 is a largely nonreactive trace gas with a global mean concentration near 392 ppm. Within the Salt Lake Valley, near-surface CO_2 mole fractions have been measured continuously using a network of infrared gas analyzers at urban and rural sites (Fig. 3.1a). Some of the network's CO_2 concentration records extend back to 2001 (http://co2.utah.edu).

The volume of enhanced CO_2 mole fractions within urban areas has been called the urban CO_2 dome (Idso et al., 1998). The urban CO_2 dome can be thought of as a gaseous analogue of the so-called urban heat island – the enhanced urban temperatures relative to temperatures in surrounding rural areas (Environmental Protection Agency, 1990; Moriwaki and Kanda, 2004; Oke, 1967). In an urban area of one million residents, annual mean temperatures can range from 1-2°C warmer than surrounding rural areas, and can reach 12°C higher on calm nights (Akbari, 2005).

Similarly, CO_2 within the urban CO_2 dome is elevated relative to surrounding rural areas (Idso et al., 2002; Pataki et al., 2003). Idso et al. (2002) found that the CO_2 concentrations in the city of Phoenix, Arizona could reach up to 50% higher than surrounding rural values on winter mornings, and could reach 25% higher during winter afternoons. Similarly, winter morning concentrations of CO_2 in Salt Lake City can exceed 550 ppm, approximately 40% higher than surrounding rural areas.

Urban areas generally exhibit a double peak in CO_2. The morning peak occurs when traffic emits CO_2 into a shallow boundary layer. Mole fractions decrease during daytime mixing in the winter and summer before a second, lower, peak occurs due to evening traffic and a diminishing boundary layer (Gratani and Varone, 2005; Idso et al., 2002; Kelome et al., 2006; Lichtfouse et al., 2003; Nasrallah et al., 2003; Pataki et al., 2003; Soegaard and Moller-Jensen, 2003; Strong et al., 2011; Widory and Javoy, 2003; Zimnoch et al., 2004).

The results of a study during a winter temperature inversion in the Salt Lake Valley indicated a strong relationship between atmospheric stability, the height of the capping inversion, and CO_2 mixing ratios (Pataki et al., 2005). The results indicated that CO_2 mole fraction can provide information about complex wintertime atmospheric transport and mixing in addition to carbon cycling in urban mountain basins (Pataki et al., 2005).

Strong et al. (2011) developed a multiple-box model to determine how meteorological, anthropogenic, and biological processes combine to create diel cycles of CO_2 mole fraction during each of the four calendar-based seasons within the Salt Lake Valley. The multiple-box model accounted for 53% of the hourly observations in the urban Salt Lake Valley (C_{obs}), and 90-94% of the mean diel cycle of C_{obs} depending on season. This indicated that the model formulations and prescribed anthropogenic emissions provided a realistic framework for investigating CO_2 variability within the urban Salt Lake Valley (uSLV).

Strong et al. (2011) concluded that the rate of change of the mean diel cycle of CO_2 within the uSLV was largely the result of imbalances between anthropogenic processes adding CO_2 and meteorological processes removing or diluting CO_2. Advection (removal by wind) was the most important CO_2 reduction process on average. However, dilution of CO_2 by entrainment of air from above the mixing height overtook advection in importance between sunrise and midday (Strong et al., 2011).

Although CO_2 variability has been studied within urban areas, CO_2 variability within CAPs has not be extensively studied (Pataki et al., 2005). CO_2 responds to atmospheric conditions, but little is known about its distribution and variability during CAP events. The purpose of this chapter is to use observations and a model to investigate CO_2 variability during the Persistent Cold Air Pool Study (PCAPS) described in Section 3.3.1. Section 3.3 details the data and methods for studying the variability of CO_2 within the Salt Lake Valley. Section 3.4 presents results from observational and modeling work, and Section 3.5 provides a summary and conclusion.

3.3 Data and Methods

3.3.1 The Persistent Cold-air Pool Study (PCAPS)

The Persistent Cold-air Pool Study (PCAPS) was funded in 2010 by the National Science Foundation. Salt Lake Valley is well known for wintertime temperature inversions that trap pollutants and often exceed NAAQS. The PCAPS study aimed to 1) investigate the processes leading to the formation, maintenance, and destruction of persistent midwinter temperature inversions (CAPs) that form in the Salt Lake Valley, 2) determine impacts of these processes on air pollution transport and diffusion in urban valleys and basins, and 3) determine how meteorological models can be improved to provide more accurate simulations of persistent CAPs (Lareau et al., 2012). The investigation included a large field experiment in the Salt Lake Valley from 1 December 2010 to 7 February 2011 – the winter period with minimal insolation during which persistent CAPs are most likely to occur.

Salt Lake City is located on the eastern edge of the semi-arid Great Basin of the western United States (inset, Fig. 3.2). The topography surrounding the Salt Lake Valley (SLV) is dominated by steep and narrow north-south oriented mountain ranges with the Wasatch (approximately 3300 masl) on the east side of the SLV and the Oquirrhs (2500 masl) on the west side of the SLV. The Traverse Mountains run east-west at the south end of the SLV and separate the SLV from its southern Utah Valley. There is a gap in the Traverse Mountains called the Jordan Narrows which allows the exchange of air between Utah Valley and the SLV (Lareau et al., 2012). The base of the SLV resides at approximately 1284 masl and is approximately 900 km^2 of the larger basin that encompasses most of northwest Utah (Lareau et al., 2012). SLV has approximately one million residents and is

expected to double in population over the next 30 years.

3.3.2 Meteorological Data

Instrumentation used to collect meteorological data during PCAPS is described in this section. This section comes largely from the PCAPS website (http://pcaps.utah.edu) and Lareau et al. (2012). Figure 3.2 shows locations of meteorological instruments and transects taken during the PCAPS time period, and additional information is given in (Lareau et al., 2012) and on the PCAPS website (http://pcaps.utah.edu).

3.3.2.1 Remote Sensors

Continuous observations of wind above the SLV were taken by two National Center for Atmospheric Research (NCAR) radar wind profiles, a scanning pulsed Doppler LiDAR, and a miniSoDAR (LiDAR and SoDAR, Fig. 3.2).

Changes in surface layer winds (20 – 200 magl) were determined using the minSoDAR. This instrument was ideally situated near the Great Salt Lake (GSL) to observe land and lake breezes. Winds from 200 – 3000 magl were measured with the radar wind profiles (915 and 449 MHz). The LiDAR measured winds aloft on the western edge of the SLV.

A Radio Acoustic Sounding System (RASS), which operated in conjunction with the 195-MHz radar, measured the vertical temperature structure within the SLV. RASS data allowed for high temporal sampling during transitional periods. A microwave radiometer took additional measurements of temperatures aloft.

Finally, a laser ceilometer measured the aerosol and hydrometeor backscatter. It was used to visualize boundary layer structure and provide information on the presence of the low- and midlevel clouds.

3.3.2.2 Surface Meteorological Stations

Surface meteorological stations were established to measure the surface energy balance, vertical transects of temperature and humidity, and air quality.

NCAR Integrated Surface Flux Stations (ISFS) were positioned at each of the seven surface locations measuring the surface energy balance (ISFS; Fig. 3.2). The ISFS each had a 3-D sonic anemometer, fast response temperature and humidity sensors, solar and terrestrial radiometers, and soil temperature probes.

Five extra weather stations were set up at the south end of the SLV along a quasivertical transect in the Traverse Mountains (Fig. 3.2). These stations monitored wind, temperature, and humidity

during CAPs. Additional surface meteorological stations included existing meteorological stations in the MesoWest network (Horel et al., 2002).

Temperature and humidity were recorded in 50-meter increments of elevation using HOBO® dataloggers arranged in cross-valley transects ascending the Oquirrh and Wasatch Mountains (HOBO, Fig. 3.2). One of the transects ascended Grandeur Peak, which is a prominent ridge on the west slopes of the Wasatch Range (toward upper right in Fig. 3.2).

The Utah Division of Air Quality (DAQ) measured PM2.5 hourly and provided 24-hour means. Silcox et al. (2001) supplemented these measurements with a quasivertical transect of samples in a steep slope through a neighborhood at the north end of the SLV.

3.3.2.3 Radiosondes

Radiosondes were launched from the NCAR Integrated Sounding System (ISS) site. They provided insight into the vertical thermodynamic structure of the atmosphere during CAPs. For Intensive Operational Periods (IOPs), ISS soundings were launched every 3 hours during periods of rapid change and once a day for additional monitoring of CAPs.

The National Weather Service (NWS) launched soundings twice a day as routine. Mixing depths (h) were determined by following a dry adiabat up in elevation from the surface temperature until it intersected the morning sounding profile ("parcel method"; Holzworth, 1967).

Three mobile radiosonde systems (GRAW) were used to take additional thermodynamic profiles during events such as lake-breeze fronts, differential side-wall heating, canyon drainage flows, and partial "mix-out" events during strong winds (Lareau et al., 2012).

Two vehicles and a paraglider provided additional horizontal and vertical transects. They were equipped with GPS, wind, temperature, humidity, and pressure sensors.

3.3.2.4 CO_2 Surface Network

A network of CO_2 surface samples (co2.utah.edu) ran continuously during the PCAPS period. The station locations are depicted in Fig. 3.1a and details for each site are located in Table 1 of Strong et al. (2011). The uSLV sites were defined as sites 1-5 and were compared with two baseline nonurban stations, one at the upper western edge of the SLV ("Kennecott", site 6, Fig. 3.1) and the other at the peak of one of the Wasatch Mountains ("Hidden Peak", site 7, Fig. 3.1). More detail discussing the CO_2 network can be found in Strong et al. (2011).

3.3.2.5 Anthropogenic Fluxes

The anthropogenic CO_2 flux (Q_a) estimates were developed from the "Vulcan" dataset (Gurney et al., 2009) of hourly fossil fuel emissions on a 10 km grid for the year 2002 (Strong et al., 2011).

The Vulcan dataset included flux contributions from the industrial, commercial, residential, on-road, nonroad, utility, aircraft, and cement sectors. To use this data, Strong et al. (2011) had to account for three main issues: 1) the Vulcan day of week may not accurately match simulated day of week, 2) 2002 air temperatures may not match the 2005-2009 air temperatures, and 3) the 2002 urban population count may not match the 2005-2009 population counts.

To account for the effects due to day of week, temperature, and population differences, Strong et al. (2011) calculated the anthropogenic flux for a given hour in a model box i as

$$(Q_{V,i} + \alpha_i e^{\beta_i T})\gamma^{(T-2002)} \tag{3.1}$$

where $Q_{V,i}$ is the nonresidential portion of the Vulcan anthropogenic flux. The term with α_i and β_i is an empirical model of the residential anthropogenic flux based on the air temperature (T) at the Salt Lake City International Airport for year Y. The annual mean values of Q_a are depicted for the model domain in Fig. 3.1b. For more detailed information about the development of the anthropogenic flux, please see Section 2.6 in Strong et al. (2011).

3.3.3 Development of Time-height Diagrams

Time-height potential temperature (θ) data were developed by Lareau et al. (2012), and involved blending observations from the surface meteorological stations (ISS3 data), the radio-acoustic sounding system (RASS), the NCAR Integrated Sounding System (ISS), and the NWS operational soundings. Surface data and the RASS were used to improve the interpolation of the sounding data (which was three-hourly at its most frequent) to an hourly or subhourly temporal grid. Pressure data from the soundings were used to convert the RASS virtual temperature to virtual potential temperature (assumed to be very close to the regular potential temperature in dry winter air). The data were inspected for unrealistic super adiabatic layers, which were then replaced by adiabatic layers. Additional quality control steps are detailed in Lareau et al. (2012). Contours of potential temperature are referred to as isentropes.

The radar wind profiler (RWP) data were used in a similar fashion to process the winds in the sounding time heights (Lareau et al., 2012).

3.3.4 Quasivertical CO_2 Sampling

Two sets of quasivertical CO_2 profiles were taken on the eastern edge of the Salt Lake Valley. The morning transects were taken on a prominent eastern slope where HOBO® data loggers were located (green circles south of Parley's Canyon, Fig. 3.2). The evening set of quasivertical CO_2 profiles were taken up Big Cottonwood Canyon (yellow curve, Fig. 3.2).

3.3.4.1 Infra Red Gas Analyzer (IRGA)

The instrument used for quasivertical profiles was the Infra Red Gas Analyzer (IRGA). The LI-800 CO_2 Infra Red Gas Analyzer (LI-COR Inc.) is a nondispersive IRGA that operates based on a single path, dual wavelength infrared detection system. The system measured carbon dioxide as a function of absorbed infrared energy when the sample traveled through a detection chamber. The absorbed energy and therefore carbon dioxide measurement was strongly dependent on the sampling pressure within the chamber.

For the following experiments, the IRGA collected data through an RS-232 interface connected to an external computer. The analyzer's software had a series of operating parameters to optimally configure the data collection.

3.3.4.2 Initial Laboratory Experiments

Taking quasivertical profiles of CO_2 involved an unconventional use of the IRGA in part because of the ambient pressure changes resulting from ascent in elevation. It was necessary to test the capabilities of the instrument to create a procedure that would produce reproducible and accurate results.

Laboratory experiments focused on understanding the pressure compensation feature under the following fixed conditions: the path length for the IRGA was 13.97 cm, the heater was on, the input voltage remained the same, the alarm was not enabled, the Digital to Analog Converter (DAC) offset was not enabled, the C-range was from 0–1000 ppm, the sampling period was 0.5 seconds, and the digital filter operated at 10 seconds.

The IRGA's built-in pressure compensation feature controlled for small changes in pressure. A side effect of the infrared detection system was that the concentration of CO_2 in the air sample was related to the pressure between the IRGA's intake and outtake tubes. The changes in pressure due to elevation gain or an intake pump could cause the IRGA to no longer be calibrated. To control for this effect, a mass flow controller (MFC) was used to control the mass entering and exiting the system for calibration and sampling purposes.

A 12-V, 0.45-Amp pump (Neuberger Inc., Trenton, NJ) was used to pump air samples into the system. Air samples were first pumped into a magnesium perchlorate ($Mg(ClO_4)_2$) desiccant to remove the water vapor, and were then filtered before entering the CO_2 analyzer. The sample air intake tube was attached to a one-meter avalanche probe that protruded out of the instrument backpack.

Figure 3.3 is a diagram of the laboratory setup used to test the pressure compensation feature of the IRGA. To calibrate the IRGA, the instrument needed a zero-CO_2 sample and an air sample of known CO_2 mole fraction. To zero the entering air sample, the gas was sent through the Magnesium

Perchlorate (MPL) and Soda Lime (SL) filters first. The MPL filter was used as a desiccant to remove any water vapor in the incoming air sample. The SL filter was used as a scrubber to remove any CO_2 in the sample. Once through the MPL and SL filters, the gas entered another filter removing particles and any remaining water vapor. The pump forced air through the system and the variable resistor allowed to test the instrument performance at a variety of different pressures. The variable resistor was set to a constant value during the calibration. Once the instrument finished calibrating the zero-CO_2 air sample, a gas of known CO_2 mole fraction was introduced. The calibration gas was then sent through an alternate line (indicated by a valve Fig. 3.3) and passed through the filter, through the variable resistor, and into the IRGA.

It was found that the pressure compensation feature kept CO_2 mole fractions constant during 0–10 hPa variations in pressure. In the lower troposphere, a 10-hPa decrease in pressure approximately corresponds to a 100-m increase in elevation. It was decided that during the quasivertical profile, the IRGA would be calibrated every 100-m increase in elevation at the HOBO® temperature probe corresponding to that elevation.

3.3.4.3 Final Setup

The final experimental setup is depicted in Fig. 3.4. For simplicity, the entire sampling unit could be contained in one backpack carried by one individual (Fig. 3.5a,b). A second individual was needed to carry the extra batteries and the calibration gas (Fig. 3.5c). The calibration gas was assumed to be free of water vapor. To calibrate the system, a known WMO (World Meteorological Organization) traceable calibration standard was introduced into the LI-800 every 100 m gain in elevation. Similar to the laboratory experiments, the calibration gas went through a valve to be zeroed of CO_2 before entering the IRGA or went directly to the IRGA as a known CO_2 concentration gas. Different from the laboratory setup, the calibration system and the experimental system were separated and controlled by a valve located before the IRGA (Fig. 3.4 and 3.5b).

The separate sampling system was run through a MPL desiccant before being filtered and entering the IRGA at a constant flow rate. The pump drew in air from the sampling tube, before entering the filter. A mass flow controller (MFC, Fig. 3.4) was located before the input to the IRGA to regulate the amount of mass entering the IRGA for both calibration and sample – solving the pressure change difficulties. The mass flow controller was run at 300 L/min and the computer recorded 10-second running averages every 0.5 seconds.

Samples were collected continuously until the computer battery died. A laptop computer was used in place of a datalogger to save weight and human-power while hiking. The instrument setup is shown in Fig. 3.5a and 3.5b, calibration at a HOBO® site is shown in Fig. 3.5c, and sampling

technique is shown in Fig. 3.5d. Table 3.1 details the experimental setup for the IRGA controls. The controls were set using the IRGA software installed on the computer.

3.3.4.4 Quasivertical Profiles of CO_2

Grandeur morning transects of CO_2 mole fractions were taken on foot on the mornings of 26, 27, and 29 January 2011 at approximately 6:00 LST. During the morning of 28 January 2011, the transect was taken driving up Parley's Canyon to gain greater elevation.

Grandeur Peak borders the east side of Salt Lake City (Fig. 3.2). To the north of Grandeur Peak is Parley's Canyon and Interstate-80, and to the south of Grandeur Peak is Mount Olympus and the rest of the central Wasatch Mountain Range. In the winter, the low-lying vegetation on Grandeur Peak was mainly covered in snow. Toward the summit, there were sparse trees near the trail but their net CO_2 contribution was considered negligible. The trail was west-facing, meaning that the samples were heavily influenced by air from different elevations within the Salt Lake Valley as desired. The sampling for the Grandeur morning transects started at approximately 6:00 LST on 26 January 2011 during IOP 9 to sample the nocturnal boundary layer and the free tropospheric air.

Big Cottonwood Canyon (BCC) quasivertical profiles were taken daily on 26-30 January 2011 starting at 19:00 LST. The CO_2 intake tube was located one meter above the vehicle roof. Additional instruments in the vehicle continuously measured pressure, wind, humidity, position, and temperature during the transects. The pressure from the vehicle and the pressure on the IRGA were consistently 2 hPa apart during all transects with the vehicle measurements always higher. Big Cottonwood Canyon is located south of Grandeur Peak, also on the east side of the SLV (Fig. 3.2).

3.3.4.5 Representativeness of Measurements

The quasivertical profiles were intended to provide information about the vertical distribution of CO_2 within the SLV and its relationship to atmospheric dynamics. The results appeared to be an informative proxy for truly vertical in-situ measurements over the valley as presented in Section 3.4. Nonetheless, several considerations discussed below warranted some caution in the interpretation of results: the measurements involved an unorthodox use of the instrument, were performed in the surface layer along the valley walls, evidenced effects from occasional pooling of dense air in the topography, were subject to the influences of traffic, and were collected in the airspace above breathing humans.

The atmospheric surface layer is defined as the layer of the atmosphere that is in contact with the ground. As such, measurements taken in the surface layer are subject to spatial heterogeneity due to surface turbulence and mechanical mixing from interactions with the ground, trees, and other objects in the surface layer. The morning transects taken on foot were on an exposed ridge selected

to maximize sensitivity to air from the valley. It was assumed that elevations gained by hiking would capture the transition between the nocturnal boundary layer, the previous day's residual layer, and depending on atmospheric stability, the free troposphere. The evening transects were taken by vehicle up a large canyon to span a much greater elevation range capturing the depth of air that was mixed during daytime heating.

Traffic contamination was seen during the driving transects. Large spikes were seen in the CO_2 data when cars passed due to localized CO_2 emissions from fossil fuel combustion. It was assumed that the values taken between the vehicular CO_2 spikes represented ambient canyon air at a specific elevation.

Localized pooling of air potentially occurred within topographic depressions. CO_2 gas is denser than air, causing it to sink and pool in topographic depressions during minimal turbulence. Topographic pools of higher CO_2 mole fraction air were seen during the driving transects up Big Cottonwood Canyon at consistent locations as noted in Section 3.4.

As discussed in Section 3.3.4, this field work involved an unorthodox use of the IRGA. In conventional applications, the IRGA's pressure compensation feature controls for synoptic storms before, during, and after which the atmospheric pressure changes (variations typically are 5 to 10 hPa). For this field work, the instrument was used to make quasivertical measurements where an elevation change of 100 m was approximately equal to a 10-hPa pressure decrease. The mass flow controller was used to control for this effect.

Humans exhale high mole fractions of CO_2. This required the intake tube for the IRGA to extend well above the human hiking. During the field work, the intake tube protruded one meter out of the sampling backpack and was assumed high enough to avoid substantial effects from breathing.

3.3.5 Classification of High-CO_2 and Low-CO_2 Periods

The PCAPS winter of 2010-2011 was divided into periods of high, low, and variable CO_2 to guide the analysis and presentation of results. First, the arithmetic mean of the uSLV sites (locations 1-5, Fig. 3.1a) was calculated (C_{obs}; thin black curve, Fig. 3.6). C_{obs} was then temporally smoothed using a 48-hour running mean filter (bold black curve, Fig. 3.6), and values were identified above the 66^{th} percentile (red circles, Fig. 3.6) and below the 33^{rd} percentile (blue circles, Fig. 3.6). "High-CO_2" periods were defined when C_{obs} remained above its 66^{th} percentile for 60 or more hours (H1-H3 shaded red, Fig. 3.6), "low-CO_2" periods were defined when C_{obs} remained below its 33^{rd} percentile for 60 or more hours (L1-L5 shaded blue, Fig. 3.6), and the intervening times were defined as "variable-CO_2" periods (unshaded, Fig. 3.6). Table 3.2 provides details for the CO_2 periods including their beginning and ending dates.

3.3.6 Statistical Methods

Reported correlations were tested for significance at the 95% confidence level by bootstrapping the distribution of the Pearson correlation coefficient r (Efron, 1979). For each bootstrapping procedure, data pairs were selected with replacement 1,000 times.

Spectral filtering of time series was accomplished using a 5^{th}-order Butterworth filter with zero phase distortion and a monotonic magnitude response that was maximally flat in the passband (Butterworth, 1930). Where a "cutoff period" was specified in the text, the filter's magnitude response was 0.5 at the frequency corresponding to that period.

3.4 Results

Variability of CO_2 during PCAPS is presented in this section. Observations and modeling were used to investigate atmospheric influences on CO_2 (Section 3.4.1), vertical variations in CO_2 (Section 3.4.2), the influence of boundary layer evolution on CO_2 (Section 3.4.3), and the performance of the multiple box model during PCAPS (Section 3.4.4).

3.4.1 Atmospheric Influences on Surface CO_2 Mole Fractions During Winter

The success of the multiple box model used by Strong et al. (2011) indicates that its inputs should provide insight into the principal controls on CO_2 variability within the uSLV. Fig. 3.7 shows the various model inputs alongside the time series of C_{obs}, and presentation of these results is organized below according to the periods of high-CO_2, low-CO_2, and variable-CO_2 defined in Section 3.3.5.

3.4.1.1 Periods of High CO_2 Mole Fraction

High periods 1, 2, and 3 (H1, H2, and H3; Fig. 3.6) were all characterized by lower boundary layer growth (h, Fig. 3.7b), low wind speeds (V, Fig. 3.7d), and above average anthropogenic emissions (Q_a, Fig. 3.7e).

The first half of H1 was dominated by very high nocturnal CO_2 mole fractions. The peak in C_{obs} on 1 December 2010 reached 599.2 ppm (Fig. 3.7a; Table 3.3) and resulted from high anthropogenic flux (Q_a, Fig. 3.7e) presumably elevated by natural gas combustion (Q_r, Fig. 3.7e). During the following day, 2 December 2010, the very small boundary layer growth of 216 m coupled with reduced Q_a and increased V markedly decreased mole fractions in the valley to approximately 450 ppm (Fig. 3.7), suggesting that the residual layer air was very clean compared to the uSLV air. During 4 December 2010, there was no or very minimal boundary layer growth, and C_{obs} elevated once again (Fig. 3.7a).

The later half of H1 was dominated by increased winds, larger boundary layer growth, and decreasing CO_2 mole fractions. On 6 December 2010, CO_2 mole fractions decreased to approximately 416 ppm. This event was initiated by wind speeds rapidly increasing from 0 m s^{-1} to 5 m s^{-1} and remaining high through 7 December 2010. Very minimal boundary layer growth on 7 December allowed CO_2 to build up in the uSLV and increase up to 500 ppm. Boundary layer growth on 8 December decreased mole fractions from 500 ppm down to the lowest level of H1 (406.5 ppm; Table 3.3). H1 ended with consistently above average winds associated with the arrival of a cold front near 10 December 2010 (V, Fig. 3.7d). This was described as a "southerly mix-out event" (Lareau et al., 2012) because of the strong southerly flow (v, Fig. 3.7c).

The second high period, H2, had two distinct relative maxima above the average of the period and three distinct relative maxima below the average (Fig. 3.7; Table 3.2). CO_2 mole fractions started lower than in H1, but rose quickly from a daytime minimum of 435 ppm to an overnight maximum of 555 ppm. This was due to small boundary layer growth of 342 m (Fig. 3.7b), consistently low winds (V, Table 3.2 and Fig. 3.7d), and higher than average anthropogenic emissions (Q_a, Table 3.2 and Fig. 3.7e). Anthropogenic emissions were elevated in part due to cold night time temperatures and larger amplitude diurnal residential heating cycles (Q_r, Fig. 3.7e). Although boundary layer growth was minimal, the extreme decrease in daytime CO_2 mole fractions down from 555 ppm to 445 ppm was in part due to entraining much cleaner residual-layer air into the atmosphere as compared with the extremely high CO_2 mole fractions that built up in the nocturnal boundary layer overnight. With a minimal boundary layer growth from the day before, mole fractions the following day exceed 555 ppm and reached 564.7 ppm (Table 3.3), the highest of H2. Once again, minimal mixed layer growth of 213 m during daytime mixing was enough to decrease uSLV mole fractions to 453 ppm.

During the latter half of H2, CO_2 mole fractions decreased largely due to slightly lower anthropogenic emissions (Q_a, Fig. 3.7d and Table 3.2) and elevated mixed layer growth (h, Table 3.2 and Fig. 3.7b). H2 ended with declining anthropogenic emissions, larger mixed layer growth, a wind shift, and higher wind speeds. These changes heralded the arrival of a sharply delineated arctic front approaching Salt Lake Valley from the north. Unlike H1, the end of H2 was not preceded by particularly strong southerly winds, and thus the southerly wind mix-out mechanism was not observed.

CO_2 mole fractions within the uSLV remained moderate, varying between 410 ppm and 472 ppm after H2 ended, and then increased into period H3 as wind speeds decreased (V, Fig. 3.7d) and mixing depths decreased (h, Fig. 3.7b). Similar to H2, H3 featured a large spike in CO_2 mole fraction up to 543 ppm due to large anthropogenic emissions (Q_a, Fig. 3.7e) and shallow mixed

layer heights (280 m, Fig. 3.7b). The mole fraction then decreased into the afternoon on 12 January 2011 in part due to the large difference between the residual layer cleaner air and the extreme high CO_2 mole fraction urban air (i.e., entrainment). Anthropogenic emissions steadily decreased during H3 (Q_a, Fig. 3.7e) due to warming and decreased Q_r (Fig. 3.7e), but mixed layer growth remained small. This attributed the decrease in CO_2 mole fraction largely to the variable winds and the larger diurnal up valley/down valley flow advecting air around and out of the uSLV (Fig. 3.7c). H3 ended with very low anthropogenic emissions, and low, but consistent wind speeds. Similar to H1, H3 ended with the arrival of a cold front moving from west to east and causing winds to shift from southerly to northerly (Fig. 3.7c).

In summary, periods of high CO_2 mole fraction were sustained largely due to elevated anthropogenic emissions, decreased wind speeds, and small boundary layer growth. Large variability during high periods was related to the difference in peak urban mole fraction and the lower mole fraction residual-layer air being mixed into shallow winter mixed layers. The end of high-CO_2 periods was generally associated with decreased anthropogenic input and increased wind speeds, and was sometimes characterized by the passage of a cold front (i.e., a "southerly mix-out event").

3.4.1.2 Periods of Low CO_2 Mole Fraction

Low periods (L1-L5, Fig. 3.6) were generally characterized by strong winds proceeding or following a wind shift and decreased anthropogenic emissions (Fig. 3.7 c-e). The boundary layer growth varied from small growth in L1-3 to large growth in L4-5 (Table 3.2; Fig. 3.7b).

L1 started as a synoptic front moved in. The winds steadily increased, and the wind direction was predominately from the south (i.e., $v > 0$ indicating down-valley flow). CO_2 mole fractions in the uSLV steadily decreased as the winds became stronger. Anthropogenic emissions were low, as were residential emissions (Q_r, Fig. 3.7e), indicating a warmer period. The cold front moved past just before 00:00 LST on 19 December 2010 and decreased CO_2 mole fraction to 395.8 ppm, the lowest value during PCAPS (Table 3.3, Fig. 3.7a). After the frontal passage, wind speeds decreased and boundary layer growth was small. Also, anthropogenic emissions increased due to temperature-driven increases in Q_r (Fig. 3.7e), causing CO_2 mole fractions to slowly increase again and exceed the threshold for defining a low-CO_2 period (Fig. 3.6a).

Relatively low Q_r and moderate winds then allowed C_{obs} to return quickly to values below its 33rd percentile, marking the beginning of L2. Mole fractions started at their highest value of the period at 435.6 ppm but quickly decreased to 403.6 ppm, their lowest value of L2 (Table 3.3). Wind speeds remained elevated, boundary layer heights remained variable, and anthropogenic emissions were steady. The low boundary layer growth midway through L2 (h, Fig. 3.7b) caused a spike in CO_2 mole fraction (Fig. 3.6a). The slightly elevated wind played a large role in advecting high

mole fraction air out of the valley, keeping the mole fractions low. L2 ended with slowly rising CO_2 mole fractions in part due to anthropogenic emissions, lower wind speeds, and a moderate mixed layer height.

For L3, CO_2 mole fractions within the uSLV decreased to their lowest consistent values as a large front moved through the uSLV with the largest sustained wind speeds of the period (Tables 3.2 and 3.3; Fig. 3.7). A large shift from southerly to northerly winds indicated a large cold frontal passage just before 00:00 LST on 29 December 2011 (Fig. 3.7c). During the next four days after the frontal passage, C_{obs} remained within 6 ppm of the L3 minimum (399.4 ppm; Table 3.3). Cold air advection caused an increase in residential emissions and the total anthropogenic emissions (Fig. 3.7e). The mixed layer heights were consistent and moderate relative to the rest of the PCAPS period (Table 3.2). However, the increase in anthropogenic CO_2 emissions and the small mixed layer heights were not enough to increase the uSLV mole fraction. Consistently strong winds advected high CO_2 mole fraction air out of the uSLV bringing in cleaner air. There was a very small amplitude diurnal cycle in CO_2 during this period, in part due to the consistently strong winds. L3 ended as the winds decreased to near zero and elevated anthropogenic emissions continued because of low temperatures. The weak winds no longer advected high mole fraction air out of the uSLV, and the CO_2 mole fractions increased once again.

L4 started in a preconditioned environment after a small wind storm. Unlike the previous low periods, the mole fractions were quite variable ranging from 396.7 to 471.3 ppm – one of the largest ranges observed during a low period (Table 3.3). Another small cyclonic storm shifted winds from southerly to northerly slightly after 00:00 LST on 18 January 2011 (Fig. 3.7c), bringing elevated wind speeds. L4, unlike L1-3, had moderate-to-large mixing heights (Fig. 3.7b; Table 3.3), and C_{obs} remained low with a discernible diel cycle as anthropogenic emissions decreased (Q_a, Fig. 3.7e; Table 3.3). L4 ended with consistently low winds which were not strong enough to advect the high-concentration air out of the uSLV despite the large mixing depths.

The final low period, L5, started after a series of moderately high mixed layer heights entrained cleaner residual-layer air (Fig. 3.7). The beginning period of L5 was characterized by large diel cycles in wind, average CO_2 emissions, and moderate mixed layer growth (Fig. 3.7). Around 00:00 LST on 30 January 2011, a cold front brought strong northerly winds to the uSLV. These were the strongest winds seen during PCAPS. CO_2 mole fractions in the uSLV remained around 398 ppm and varied by 5 ppm before extremely large anthropogenic emissions caused a spike around 15:00 LST on 2 February 2011. Similar to L3, the frontal passage brought cold air into the uSLV and anthropogenic CO_2 emissions increased, and CO_2 mole fractions in the uSLV continued to rise despite large mixing heights of 753 magl. L5 ended with winds returning to near zero, and CO_2

increasing to the highest levels seen during a low period, up to 478.6 ppm (Table 3.3).

In summary, periods of low C_{obs} and minimal variance in the uSLV were sustained by strong elevated winds and consistent boundary layer growth. A cyclonic storm occurred during all low-CO_2 periods causing residential temperature-driven increases in total anthropogenic flux and minimized boundary layer growth. The increased wind associated with the cyclonic passage acted to diffuse the emissions and maintain low CO_2 mole fractions. Large mixed layer heights without elevated winds were not able to sustain low CO_2 periods.

3.4.1.3 Periods of Variable CO_2 Mole Fraction

Periods of variable CO_2 mole fractions are indicated by the white panels in Figs. 3.6 and 3.7. The variable period between H1 and L1 lacked the conditions that caused elevated CO_2 during the proceeding H1 period, featuring instead variable mixing heights, variable wind directions, variable to strong winds, and upward trending anthropogenic CO_2 emissions.

The very short variable period between L1 and L2 was due in part to the consistently low mixed layer heights and low winds that increased the CO_2 mole fractions above the 33^{rd} percentile threshold. Larger winds followed that ventilated the uSLV removing any excess CO_2 and initiating L2.

The variable period between L2 and L3 and between L3 and H2 were similar to the first variable period. The variable CO_2 mole fractions were driven by a mixture of high and low mixed layer heights, variable winds, and increasing anthropogenic emissions (Fig. 3.7). These periods ended with a large mixout event due to high winds.

The variable period between H2 and H3 was short and stemmed from a weak front and moderate mixed layer heights larger than during H2 and H3. The CO_2 mole fractions were so high during H2 that the weak wind event just past 00:00 LST on 9 January 2011 (Fig. 3.7c) was not strong enough to advect all the high mole fraction air out of the uSLV. However, the large dramatic spike in CO_2 mole fractions at Hidden Peak after 9 January 2011 (green curve, Fig. 3.8) indicates that moderate winds and very high mole fraction air can ventilate out of the uSLV to higher elevations. As discussed, the small wind event was too weak to fully mix out the uSLV, allowing another high period to initiate shortly after the wind event ended.

3.4.2 Vertical Variations

The Kennecott and Hidden Peak sites (numbered 6 and 7, respectively, Fig. 3.1a) offer insight into the dynamics underlying C_{obs} variability because of their vertical and horizontal location relative to the uSLV (sites 1-5, Fig. 3.1a), and contrasts among the sites were probed to highlight quasivertical temporal variations in CO_2. Kennecott is situated near the urban-rural transition west

of the uSLV on the east slope of the Oquirrh Mountains approximately 250 m above the valley floor, and Hidden Peak is an alpine site approximately 2 km above the valley floor [See also Table 1 in (Strong et al., 2011)].

The Kennecott CO_2 mole fraction (C_{Ken}; red curve, Fig. 3.8) was positively correlated with C_{obs} overall ($r = 0.38$). Low-pass filtering the data with a cutoff period of one week (Section 3.3.6) enhanced this positive correlation substantially ($r = 0.73$; Fig. 3.9a), illustrating the tendency for C_{obs} and C_{Ken} to move together in response to weekly variations in meteorological conditions (i.e., wind and stability) and anthropogenic emissions from uSLV (i.e., air temperature-driven natural gas combustion).

By contrast, focusing on diel time scales by band-pass filtering with cutoff periods at 18 and 24 hours, C_{obs} and C_{Ken} were inversely correlated ($r = -0.38$; Fig. 3.9b). This tendency for inverse correlation illustrated an important aspect of the meteorological linkage between the sites. Specifically, as the mixing depth increased during the day, C_{obs} tended to decrease in response to lower-concentration air being mixed in from higher elevations, and C_{Ken} tended to increase in response to higher-concentration air being mixed in from lower elevations (Fig. 3.9b). At night, C_{obs} tended to increase as anthropogenic emissions concentrated in the nocturnal boundary layer, and C_{Ken} tended to decrease as wind removed the CO_2 that was delivered quasivertically by daytime mixing.

Analogous results for CO_2 mole fractions at Hidden Peak (C_{Hid}) were quite different from the Kennecott results described immediately above. Firstly, C_{Hid} and C_{obs} were negatively correlated overall ($r = -0.36$; Fig. 3.8). Low-pass filtering the data with a cutoff period of one week slightly enhanced the correlation ($r = -0.43$; Fig. 3.9c), indicating that elevated CO_2 at Hidden Peak was associated with export of CO_2 from uSLV. Band-pass filtering for diel time scales with cutoff periods of 18 and 24 hours yielded no correlation between C_{obs} and C_{Hid} (not shown). Hidden Peak was thus impacted by venting of CO_2 from the uSLV not by diurnal variations of wind or mixing depth, but rather by synoptic time scale meteorological conditions that enabled or suppressed sufficiently large horizontal and vertical transport, and this interpretation follows naturally from Hidden Peak's elevation above the valley floor being larger than typical winter mixing depths (Fig. 3.11, Chapter 2).

To summarize, sustained periods of stability, low-V, and high-Q_a were conducive to decreased CO_2 at Hidden Peak because these conditions inhibited vertical and horizontal transport of air from uSLV to Hidden Peak. The same conditions were conducive to elevated CO_2 at Kennecott because the high-concentration uSLV air generally mixed up to the elevation of Kennecott during the day. On diel time scales, this quasivertical mixing of uSLV air to Kennecott led to the inverse correlation

between C_{obs} and C_{Ken} (Fig. 3.9b). If C_{Ken} responded to vertical mixing from uSLV during the day, it may have captured information about concentrations in the residual nocturnal boundary layer, and this idea is probed further in Section 3.4.4.

3.4.2.1 Quasivertical CO_2 Profiles

To further investigate vertical variations of CO_2 during PCAPS, quasivertical profiles of CO_2 were taken over a period of five days during IOP9 (Fig. 3.10). In addition, one test profile was taken up Big Cottonwood Canyon (BCC) prior to the start of IOP 9 and discussion below begins with this test profile. Associated time-heights plots of θ, RH, and h are shown in Fig. 3.11. The quasivertical CO_2 variations are discussed below as if they were truly vertical, although it was noted that they were oriented quasivertically following the terrain (Section 3.3.4).

Cold air pooling can occur within the topographic depressions along the Big Cottonwood Canyon driving transect. These cold pools can have locally higher CO_2 mole fractions similar to the larger scale cold pools seen within the SLV. Multiple topographical depressions can be seen in Fig. 3.12 from just above 2000 m to 2200 m.

Morning (6:00 LST) profiles were taken on Grandeur Peak along the line of temperature HOBOs® with the exception of 6:00 LST on 28 January 2011 when a quasivertical profile was taken up Parley's Canyon (Fig. 3.2). Evening profiles were taken up Big Cottonwood Canyon (BCC; yellow circles, Fig. 3.2) in an effort to measure well above the uSLV mixing depth.

Running mean C_{obs} was within its 66^{th} percentile for a short period before IOP 9 started (Fig. 3.6 and 3.7). The test profile (Fig. 3.10a) showed CO_2 mole fractions decreasing rapidly over 300 m up to a clear, well mixed layer at approximately 1700 m. In contrast to all subsequent profiles, the reading at the Kennecott station did not align with the vertical transect data, indicating that different phenomena were driving Kennecott's mole fractions than were driving the eastern SLV's mole fractions. The uSLV sites showed significant variation which was replicated during subsequent transects.

The second profile (Fig. 3.10b) was taken starting at 6:00 LST on 26 January 2011, the first morning of IOP 9. Figure 3.10b shows high concentrations near the valley floor decreasing to a relatively well-mixed layer above assumed to be the residual layer. The photograph in Fig. 3.5c was taken during this profile and shows a very shallow cloud layer moving from the western SLV to the eastern edge of the SLV. Kennecott appeared to be above the nocturnal boundary layer and cold pool. The Kennecott data on the west side of the SLV corresponded well with the quasivertical profile taken on the East side of the SLV. Kennecott's mole fraction were still above free tropospheric values, indicating the presence of a residual layer from the previous day.

The uSLV site's CO_2 mole fractions were much higher than Kennecott and Hidden Peak. Spatial heterogeneity of site measurements indicated that multiple processes affect CO_2 concentrations even during persistent cold-air pool events. The Sugarhouse reading suggested advection from a large traffic or natural gas source, whereas the Rose Park site may have been cleaner due its proximity to the Great Salt Lake (GSL) and its displacement north of the major downtown traffic. University site was more influenced by local topography, was higher in elevation, and was elevated above concentrated traffic emissions.

The evening profile collected in BCC at 17:00 LST on 26 January 2011 (Fig. 3.10c) indicated a shallow well-mixed surface layer with concentrations lower than the proceeding morning. Kennecott remained cleaner and out of the cold-air pool as was indicated in Fig. 3.10c, with Hidden Peak representative of the free troposphere. At the time of this profile, Fig. 3.11 showed a moderately well-mixed surface layer to around 1500 m about 80 m below Kennecott (1580 masl), followed by a rapid decrease to the free tropospheric values at Hidden Peak. Kennecott was within the residual layer with lower concentrations than the valley, but still higher concentrations than Hidden Peak. The potential temperature contours were nearly vertical, indicating an unstable air mass allowing for mixing.

On the morning of 27 January 2011, conditions were markedly different than on the morning of 26 January 2011 (Fig. 3.10b,d). The quasivertical morning profile showed high surface concentrations and a well-mixed atmosphere above Kennecott. The potential temperature contour lines (isentropes) in Fig. 3.11 indicated that a strong shallow cold pool had developed at the valley floor, but did not extend vertically to overtake Kennecott's elevation. The high surface CO_2 mole fractions confirmed that surface stability plays an important role in elevating CO_2 mole fractions.

The following evening (17:00 LST 27 on January 2011; Fig. 3.10e), the mixed layer extended well above Kennecott (magenta curve, Fig. 3.11) and the atmosphere was well mixed within the boundary layer, as indicated by similar CO_2 mole fractions recorded well into BCC. The higher mixing heights allow CO_2 to mix higher in elevation within the urban CO_2 dome without completely leaving the system.

The following morning (6:00 LST on 28 January 2011; Fig. 3.10f), the quasivertical profile was taken up Parley's Canyon, a busy large canyon that had extensive truck traffic even very early in the morning. The network stations corresponded well with the quasivertical profile data, indicating a complex spatially heterogeneous vertical profile of CO_2. The CO_2 mole fractions were increased from the previous night (compare Fig. 3.10e,f). However, based on the potential temperature contours in Fig. 3.11, evening and early morning anthropogenic CO_2 emissions were entering a neutral or conditionally unstable lower atmosphere. The 100% relative humidity contour near

the profile time (white contour near green vertical transect line, Fig. 3.11f) indicated the presence of clouds overnight that dissipated with afternoon mixing. CO_2 mole fractions varied little with elevation, indicating that mixing occurred below the cloud bottom. Cloud-top radiational cooling strengthened the elevated temperature inversion, as shown by the near-horizontal, closely packed potential temperature contours in Fig. 3.11f from 1650 to 1850 masl.

By the subsequent evening (17:00 LST on 28 January 2011), the midlevel temperature inversion had continued to strengthen (Fig. 3.10g). The estimated mixing depth was large, allowing mixing to occur within the conditionally unstable surface airmass. Despite mixing, CO_2 mole fractions increased from the morning, and higher-concentration air was building up within the urban CO_2 dome held in by strong stability (Fig. 3.10g). In Figs. 3.10 and 3.11g the atmosphere was well mixed to around 1800 masl. Above 1800 masl, CO_2 mole fractions decreased close to free tropospheric values indicated by the Hidden Peak station. Strengthening atmospheric stability (descending isentropes, above 1900 masl, Fig. 3.11g) contributed to inhibiting the vertical transport of anthropogenic CO_2 above the uSLV.

The following morning (6:00 LST on 29 January 2011), anthropogenic CO_2 emissions into a shallow nocturnal boundary layer increased the surface concentrations (Fig. 3.10h). Unlike the other seven profiles, the Rose Park station was higher than all other uSLV stations, indicating the presence of a local CO_2 source, or a wind shift that advected higher mole fraction air towards the Rose Park station (Fig. 3.10h). The Kennecott station had lower mole fractions than the previous evening in agreement with the inverse diel correlation between $C_{\mathrm{Ken}}$and C_{obs} (Section 3.4.2). Increased RH remained in the valley and a cloud formed at the elevated temperature inversion (100% RH contour near green transect line, Fig. 3.11h). The presence of this cloud was verified in Fig. 3.5d, where C. Stwertka was above the cloud-topped inversion during the morning quasivertical transect.

The final profile was taken at 17:00 LST on 29 January 2011 (Fig. 3.10i). As expected, afternoon mixing decreased the morning uSLV surface concentrations. Although conditions were well-mixed, similar to Fig. 3.10g, the uSLV sites were lower in CO_2 mole fraction than the Kennecott site, indicating that other phenomena such as katabatic winds or a lake breeze were contributing to evening uSLV mole fractions.

A profile of data from the CO_2 network stations is shown in Fig. 3.10j and indicated by a green line toward the right edge of Fig. 3.11. This profile depicted quasivertical CO_2 variability within a synoptic storm system (00:00 LST on 31 January; Fig. 3.7d,e) that caused mechanical and thermodynamic mixing. Although not supplemented by a quasivertical transect, these station data indicated that valley-floor observations can approach free-tropospheric mole fractions under sufficient synoptic forcing (Figs. 3.10j, 3.11j).

3.4.3 Insight into High-CO_2 Periods from IOP Data

This section focuses on the role of boundary layer evolution observed during the PCAPS IOPS that corresponded to higher CO_2 periods (H1 was IOP 1, H2 was IOP 2, and H3 was IOP 6, Table 3.2). The detailed data sets collected during these IOPs enabled insights into the atmosphere's vertical structure that were not available from the model input terms presented in Section 3.4.1, and so these high-CO_2 periods are revisited here.

The highest CO_2 mole fractions of PCAPS occurred in IOP 1 at 7:00 LST on 2 December 2010 (Fig. 3.8a; Table 3.3). This absolute maximum was proceeded by a period of very high surface atmospheric stability, low wind, cold temperatures, and high relative humidity (Fig. 3.13). The high surface atmospheric stability was in part due to overnight radiational cooling from minimal cloud cover (Fig. 3.13c). During this overnight period, CO_2 started to build within this very shallow nocturnal boundary layer (Fig. 3.14a) until a maximum was reached right at sunrise. Then, the atmosphere evolved toward conditional instability through 1500 masl (nearly vertical isentropes), and the surface nocturnal boundary layer air mixed with the residual layer.

A partial mixout occurred during the night of 3 December 2010. This was seen by warmer temperatures aloft which acted to erode the cold-air pool downward from the top (Fig. 3.13b), affecting Kennecott before the uSLV. Before and after this partial mixout, atmospheric surface stability was extremely high, acting to contain higher CO_2 mole fraction air within the uSLV. This in part kept C_{obs} high, suppressing vertical transport and minimizing uSLV influence on C_{Ken}. However, the partial mixout first affected Kennecott (decrease of C_{Ken} close to C_{Hid} values at 00:00 LST on 3 December 2010; Figs. 3.8a, 3.13b) while C_{obs} held steady. As the partial mixout reached the uSLV, C_{obs} decreased and C_{Ken} increased as expected from their tendency for inverse diel correlation (6:00 LST on 3 December 2010; Fig. 3.8a), yet this partial mixout was not sufficient to decrease the uSLV CO_2 mole fractions below the high-period criterion.

CO_2 mole fractions in the uSLV were once again very high during 4-5 December 2010 (Fig. 3.8a). There was a double peak in nocturnal CO_2 which was in part due to the shift in atmospheric stability seen in the isentropes in Fig. 3.13. Low wind speeds and clear skies acted again to set up a pronounced nocturnal boundary layer with strong atmospheric stability. Relative humidities were high in part due to condensation and sinking of cold air at the surface. The relative humidities were not sufficient to create a surface fog which would be visible in the ceilometer data as red shading near the surface (e.g., Fig. 3.13c at 18:00 LST on 5 December 2010). Mixing heights remained low, allowing CO_2 to build up within the surface layer and limiting mixing with free tropospheric air. The nocturnal cold-air pool was broken up in part by a weak, short period of low atmospheric stability and warmer temperatures (Fig. 3.8).

On the night of 5 December 2010, CO_2 mole fractions in the uSLV were elevated (yellow shading between 5 and 6 December 2010; Fig. 3.14a), but not as high as the previous evenings. During the night, temperatures were warmer, there was some low level cloud cover, and the surface atmospheric stability was not as strong as it was earlier in IOP 1. There was a double peak in nocturnal CO_2 mole fractions. Examining the thermodynamic variables in Fig. 3.13, there was a short period of atmospheric instability (near 00:00 LST on 5 December 2010) in which isentropes shifted to near vertical. Cold temperatures kept mixing heights very low, constraining CO_2 to the boundary layer.

During the final nocturnal period of IOP 1, CO_2 mole fractions were elevated and increased as the night progressed (after 6 December, Fig. 3.14a). This was in part due to consistent emissions into the nocturnal boundary layer and increased atmospheric stability toward the end of the night. During this period, there were low level clouds or fog as seen by the red shading in the ceilometer data in Fig. 3.13c. Surface stability remained low while, around 1700 masl, atmospheric stability was high. Temperatures were cold and wind speeds were low. Fig. 3.14a indicated an elevated cloud-topped inversion which corresponded to the high ceilometer readings and the elevated atmospheric stability. CO_2 was able to mix below the cloud top, which in part explained the elevated but not extreme CO_2 mole fractions.

IOP 5 started at the end of low period 4 (L4, Fig. 3.6) after a large storm passed through the Salt Lake Valley, deposited snow on the ground, and decreased CO_2 mole fractions in the valley and at Kennecott to their lowest consistent values during PCAPS. IOP 5 included and ended in conjunction with the end of H2 (Table 3.2).

The beginning period of IOP 5 was dominated by nocturnal cooling seen by tightly packed horizontal isentropes with moderate CO_2 mole fractions, and featured daytime periods with tightly-packed, near-vertical isentropes (Fig. 3.15). The temporal evolution of the daytime isentropes indicated strong horizontal gradients in vertical motion consistent with the localized subsidence found along the back edge of upper level troughs (Lareau et al., 2012).

During the first night of IOP 5, the sky was clear, surface and near-surface temperatures were cold, and there was high atmospheric stability at the surface. However, CO_2 mole fractions in the uSLV were low (Fig. 3.14b). This was in part due to the low CO_2 mole fractions in the uSLV before the IOP started and in part due to very high mixed layer growth (magenta curve, Fig. 3.14b). CO_2 thus was not built up to levels seen in IOP 1 despite similar thermodynamic conditions. Over the next two days, an upper-tropospheric ridge developed over the region, indicated by the 285-K adiabat becoming more horizontal in Fig. 3.15 (Lareau et al., 2012).

The night of 2 January 2011, CO_2 mole fractions were elevated above the previous night, but

still not extremely high. Strong nocturnal cooling occurred again with clear skies, cold surface temperatures, and low wind speeds (Fig. 3.15). The mixed layer the day before was higher than average for PCAPS (Table 3.2), and acted to dilute the surface air with air from above the nocturnal boundary layer. This allowed for decreased CO_2 mole fractions in the uSLV but elevated mole fractions at Kennecott and Hidden Peak as seen in Fig. 3.8.

A strong stable nocturnal boundary layer indicated by tightly-packed horizontal isentropes did not develop during the night of 3 January (Fig. 3.15), leading to the variable-CO_2 period between L3 and H2. Lower CO_2 mole fractions were in part due to a weak nocturnal surface layer and low CO_2 mole fractions from the previous day (Fig. 3.14b). In the atmosphere, surface temperatures were much warmer than the previous two nights, there was little wind, minimal cloud cover, particulates in the atmosphere, and moderate relative humidities (Fig. 3.15).

Another above-average mixed layer height on 4 January 2011 once again diluted CO_2 mole fractions in the uSLV to much lower values (Fig. 3.14b). During the beginning of the night of 4 January 2011, a weak nocturnal temperature inversion set up but was quickly dissipated in part due to an elevated cloud forming and allowing mixing to occur below the cloud. This was indicated by the near-horizontal isentropes becoming increasingly vertical during the late night and early morning of 5 January 2011 (strong returns from the laser ceilometer; Fig. 3.15c).

Strong anticyclonic flow generated an extended period of warming aloft that slowly descended and strengthened the capping inversion (horizontal isentropes starting around 1700 masl, Fig. 3.15). IOP 5 and H2 had the highest mean uSLV CO_2 mole fractions of the PCAPS period (Table 3.3).

The nights of the 5 and 6 January 2011, very high surface CO_2 mole fractions were recorded in the uSLV (red shading, Fig. 3.14b). Both periods had strong nocturnal temperature inversions in part from clear skies and low wind speeds. This was indicated by the domes of tightly packed horizontal isentropes at the surface (Figs. 3.14b, 3.15). Similarly, surface isentrope domes were seen during the nights of 1 and 2 January 2011, but mixing heights on corresponding afternoons were above the PCAPS average (Table 3.2), causing CO_2 mole fractions to be diluted in the uSLV (Fig. 3.14b).

During the afternoon of 5 January 2011, mixed layer growth was minimally higher than the average for the period (Table 3.2). Mole fractions at Kennecott remained elevated, but much lower than the uSLV (Fig. 3.8, the darker blue shading above the valley floor in Fig. 3.14b and the lower backscatter from the laser ceilometer in Fig. 3.15). CO_2 remained elevated at the surface and very high during the following night. Kennecott CO_2 mole fractions initially diverged from uSLV values, but steadily increased throughout the remainder of the period until C_{obs} and C_{Ken} were both elevated and aligned. This indicated that the urban atmosphere was essentially "filling up" vertically with

high mole fraction air (light blue shading up to 2100 masl; Fig. 3.14b).

The nights of 7 and 8 January 2011 were dominated by a shift in atmospheric surface stability. Lower surface CO_2 mole fractions were seen accompanied by elevated Kennecott and Hidden Peak mole fractions. Anticyclonic motion at upper levels initiated a period of warming in the upper and middle troposphere (Lareau et al., 2012), and warm air appeared at lower elevations via advection and subsidence (Fig. 3.15). Initiated by radiational cooling, elevated boundary layer clouds formed overnight on both 7 and 8 January 2011. The clouds formed near the interface between the capping stable layer and the decaying convective boundary layer indicated by the horizontal isentropes in Fig. 3.15 (Lareau et al., 2012). The weaker nocturnal surface inversion that occurred below elevated stratiform clouds allowed for greater atmospheric mixing below the cloud layer. This was seen in the lower, but still elevated, CO_2 mole fractions the nights of 7 and 8 January 2011 (Figs. 3.8, 3.14b). Warmer temperatures allowed for larger mixed layer growth which acted to mix concentrated CO_2 mole fraction air higher into the urban atmosphere.

H2 and IOP 5 ended with an arctic upper-level trough that approached the region from the north. Winds started out northerly ($v < 0$, Fig. 3.7c) but quickly shifted towards southerly ($v > 0$, Fig. 3.7c), consistent with the passage of a cold front over the region. Wind speeds were higher than average (Table 3.2), but not strong enough to entirely mix out surface CO_2 mole fractions. High-concentration air was advected up to Hidden Peak where CO_2 mole fractions rapidly increased to some of the highest levels observed at that site during PCAPS (Table 3.2). uSLV mole fractions decreased, but not to values observed during low periods (Fig. 3.7).

IOP 6 and H3 initiated shortly after IOP 5 and H2 ended. High surface CO_2 mole fractions occurred on the nights of 11 and 12 January. Nocturnal temperature inversions occurred and were depicted by tightly packed isentropic domes similar to those seen in IOP 1 and IOP 5 (Figs. 3.13, 3.14, 3.15, and 3.16). As indicated in Fig. 3.16, cold temperatures and clear skies helped set up the nocturnal temperature inversions.

Larger than average mixed layer growth on 12 and 13 January 2011 increased CO_2 mole fractions at Kennecott (Figs. 3.8 and 3.14c). A small peak in CO_2 can be seen in the Fig. 3.8 time series, suggesting ventilation from the uSLV up to Hidden Peak. However, a strong nocturnal temperature inversion set up on 13 January, and mole fractions in uSLV increased markedly while mole fractions at Kennecott and Hidden Peak decreased (Figs. 3.8, 3.14c).

Warming aloft initiated subsidence and advection of warm air (starting on 13 January 2011; Fig. 3.16b). An elevated stratiform cloud layer formed on the night of 14 January 2011 in part due to subsidence and nocturnal cooling of the decaying boundary layer and capping inversion. Lareau et al. (2012) described a period of snowfall from clouds aloft which resulted in evaporative cooling

and eventual saturation within the middle and lower troposphere, but intense mixing was not seen (Fig. 3.14c). As seen in IOP 1 (period H1) and IOP 5 (period H2), CO_2 mole fractions below the capping cloud layer were diluted compared to mole fractions under a strong stable surface nocturnal boundary layer. CO_2 nonetheless built up overnight with anthropogenic and biological fluxes into the atmosphere.

The stratiform cloud layer (overnight on 13 January 2011; Fig. 3.16c) at the top of the nocturnal boundary layer decayed with daytime mixing. However, another elevated cloud layer near mountain peak level remained covering the Salt Lake Valley (14 January 2011, Fig. 3.16b). The nights of 15 and 16 January had strong nocturnal temperature inversions despite the peak-level cloud layer remaining (Fig. 3.16). CO_2 uSLV mole fractions were high, whereas Kennecott CO_2 mole fractions were low (Figs. 3.8, 3.14c), indicating that Kennecott did not receive substantial uSLV air during these days. However, a small peak in Hidden Peak CO_2 mole fractions was seen during daytime mixing on 15 and 16 January 2011 (Fig. 3.8). Associated boundary layer growth was below average as indicated in Table 3.2 and Fig. 3.7. This indicated that uSLV air could be ventilated up to Hidden Peak while not influencing air on the west slope of the Salt Lake Valley. As discussed in Lareau et al. (2012), mountain valley flows are very complex in part due to diurnally-varying slope and valley thermal flows and the presence of the Great Salt Lake to the northwest.

Descending warm air, advection, and subsidence slowly eroded away the remainder of the cold-air pool (17 January 2011; Fig. 3.16b). Kennecott and Hidden Peak mixed to their minimum mole fractions while a strong but warmer nocturnal boundary layer, and low mixed layer heights kept CO_2 elevated in the uSLV (Fig. 3.14c). Warmer temperatures decreased anthropogenic CO_2 emissions which were in part responsible for the slow decrease in uSLV CO_2 mole fractions towards the end of H3 (Fig. 3.14c). IOP 6 ended shortly after as another trough approached from the north (Fig. 3.7c).

3.4.4 Modeling PCAPS

To further understand the variability of CO_2 mole fractions during periods of high, low, and variable CO_2 mole fractions within the uSLV during winter, the multiple-box model developed by Strong et al. (2011) was run for the PCAPs period (1 December 2010 – 7 February 2011).

3.4.4.1 Model Inputs

Composite diel cycles of the model inputs for PCAPS (Fig. 3.17) closely resembled corresponding inputs for the preceding winters (compare Figs. 2.10 and 3.17). The PCAPS inputs indicated that mixing heights averaged approximately 400 m with values as high as 1200 m (Fig. 3.17a). There was a diurnal cycle in wind with morning winds coming from the south and afternoon winds coming

from the north (Fig. 3.17b). There was a double peak in anthropogenic emissions (Q_a) indicating morning and evening traffic and home heating cycles. Finally the biological flux averaged positive (i.e., into the atmosphere) with a slight increase during daytime warming (Q_b; Fig. 3.17).

3.4.4.2 PCAPs Period Model Performance

The multiple-box model accounted for 85% of the C_{obs} mean diel cycle (Fig. 3.18a), and accounted for 33% of C_{obs} on an hourly bases (Fig. 3.19). Model performance during PCAPS was not atypical (hourly performance for the preceding four winters ranged $0.28 \leq r^2 \leq 0.39$). Similar to the winter simulations for preceding years (Strong et al., 2011), the PCAPS simulation had a low bias from midday through the hours past sunset that placed the observations in the upper quartile of simulated values (circles in yellow shading, Fig. 3.18a). Overnight, the model tended to capture the PCAPS observations within its interquartile range (circles in green shading, Fig. 3.18a), but was biased high.

In the following, PCAPS and the periods corresponding to the PCAPS dates during the four preceding winters are referred to as the "winter simulations." The nocturnal high bias during PCAPS contrasted somewhat with other years in the winter simulations which tended to have a nocturnal low bias (Fig. 3.20a). The strength of the low bias scaled linearly with the variability in the observed CO_2, meaning more variability in C_{obs} corresponded to a stronger model low bias. To illustrate, box plots of C_{obs} are shown in Fig. 3.20b, and PCAPS had the smallest variance, the smallest $10^{\text{th}} - 90^{\text{th}}$ percentile range, and hence the smallest (least negative) bias. Blue symbols in Fig. 3.20c show the linear strengthening of the model bias with increases in C_{obs} variability. Interestingly, the model r^2 improved with increases in C_{obs} variability (green symbols, Fig. 3.20c) despite the associated strengthening of the low bias. This result indicated that, as C_{obs} became more variable, the model reasonably captured the amplitude of its larger diel cycles even as the negative bias strengthened.

Overall, Fig. 3.19 indicated that the model realistically simulated the timing of maxima and minima, and the simulated amplitude of the diel cycles was reasonable with positive and negative error. The first large divergence of the model from observations occurred during the first low period, L1. A large front moved through on the night of 19 December 2010 (Fig. 3.7c,d). This decreased the model uSLV mole fractions from 460 ppm to 410 ppm, very close to the observational values (Fig. 3.19). However, the model uSLV mole fractions did not remain low, but instead recovered to maintain a large amplitude diel cycle in CO_2. During L2–L5, the model also overestimated the amplitude of diel cycle of CO_2, and was not able to capture the lowest values achieved in the observations.

It was hypothesized that the model's failure to suppress the diel cycle amplitude and achieve low CO_2 mole fractions during the low periods stemmed from its dependence on a temperature-based

mixing depth (parcel method, section 3.3.2.3) that likely underestimated mechanical mixing by elevated wind speeds (Fig. 3.7d).

During the high periods, H2 and H3, there was a striking divergence of model results from observations (Fig. 3.19). During these periods, the model simulated afternoon CO_2 mole fractions much lower than observed. Two factors were hypothesized to contribute to this intriguing divergence of the model from observations. First, the model assumed a vertically homogeneous column of CO_2 below h, whereas the observations likely reflected the tendency for CO_2 to be higher at the bottom of the column – an effect most pronounced under stable conditions (Moriwaki et al., 2006).

Second, specifying a trended smooth harmonic fit to C_{Ken} as the boundary condition C_h at the model top (i.e., the concentration at the mixing depth h; Section 2.1) may have resulted in entrainment of air with unrealistically low CO_2 concentrations. Specifically, under conditions of low wind and high stability, high-concentration air vertically mixed during the afternoon likely remained above h as a so-called "nocturnal residual layer" available for mixing into the boundary layer during the subsequent afternoon (Stull, 1988), meaning the model's entrainment of C_h would explain part of its low bias. In contrast, nights with sufficient nocturnal winds above h would ventilate the nocturnal residual layer, rendering C_h more reasonable. Alternate specifications of C_h are revisited toward the end of this section.

3.4.4.3 Hourly Variation in Model Terms

Fig. 3.21 shows the hourly values of the model terms labeled in equation 2.2 of Section 2.1, and Fig. 3.18b shows the composite diel cycle of these terms. There was a peak in CO_2 mole fractions in the morning, the mole fractions decreased during afternoon mixing, then increased again as the boundary layer reformed near the surface and evening traffic emitted CO_2 into this shallow layer. The model's anthropogenic term exhibited a double peak reflecting morning and evening traffic (yellow curve, Fig. 3.18). The biological term was slightly positive in the evening and early morning due to respiration into the atmosphere and then weakened as the mixing depth increased (green curve, Fig. 3.18b). The advection term was negative because wind generally delivered cleaner air from outside the uSLV (red curve, Fig. 3.18b). The advection term weakened during the afternoon (despite the tendency for faster wind speeds) because of the weakened horizontal gradients of CO_2. The entrainment term (blue curve, Fig. 3.18b) was zero when $\partial h/\partial t \leq 0$ (Section 2.1). With daytime heating and mixed layer growth, the entrainment term become negative and contributed to rapid decline of CO_2 through midday (Fig. 3.18b).

An hourly plot of the model terms (Fig. 3.21) provided a strikingly different view of the variations underlying the composite diel cycles in Fig. 3.18b. The advection term was generally negative, indicating its role in removing CO_2 from the uSLV, but positive advection resulted occasionally

when pools of CO_2 accumulated outside the uSLV and were returned by a wind shift (red curve, Fig. 3.21). Advection had the largest variance of any model term. The entrainment term rivaled advection in the magnitude of its peaks, but mixed layer growth was limited to daytime hours. Entrainment occasionally achieved positive values when an extreme negative advection term (e.g., 17 December 2011 in Fig. 3.21) lowered uSLV concentrations below C_h by finite differencing (Section 2.1). The diel cycle of traffic emissions and natural gas combustion consistently provided positive flux into the atmosphere (light blue curve; Fig. 3.21).

3.4.4.4 Experiments

During periods of consistently high mole fractions, the model mixed the surface air with residual-layer air that was likely too low in concentration as discussed earlier in this section. The modeling framework developed by Strong et al. (2011) for the multiple-box model allowed for one vertical layer whose depth changed with mixing height. As the mixed layer grew, it entrained air with concentration C_h, specified as the harmonic fit to C_{Ken} for the period 2005 – 2011 [Fig. 2 in Strong et al. (2011)]. As discussed above referring to Figs. 3.8 and 3.10, the Kennecott site was representative of an important transition to lower mole fraction air on the vertical profile of CO_2 during most circumstances, and its elevation 250 m above the valley floor placed it higher than the uSLV climatological nocturnal boundary layer (approximately 100 m above the valley floor). As such, C_{Ken} was hypothesized to capture variations of potential relevance to the horizontally adjacent nocturnal residual layer overlying the uSLV.

Motivated by this hypothesis, the smooth harmonic used for C_h was replaced by the raw hourly Kennecott time series and the model was rerun. The experimental run with raw C_{Ken} as the upper boundary condition is referred to as the "C_{Ken} simulation" to distinguish it from the original "PCAPS simulation." The goal was to test whether using C_{Ken} more accurately simulated the variability of uSLV CO_2 mole fractions during high, low, and variable CO_2 time periods.

The C_{Ken} simulation results are shown in Fig. 3.22. As anticipated, there was some improvement of the afternoon minima in the diel cycle of CO_2 as compared to the original PCAPS simulation, particularly in the red-shaded high-CO_2 periods (compare Figs. 3.19 and 3.22). The variance accounted for by the model increased to 45%, compared to 33% for the original PCAPS simulation. Correlations of the composite diel cycles remained at 85% (not shown) in part because much of PCAPS lacked conditions conducive to accumulation of CO_2 in the nocturnal residual layer.

Importantly, however, use of raw C_{Ken} as the upper boundary condition exacerbated the model's tendency for a positive nocturnal bias, increasing the mean bias error from 4.2 ppm for the PCAPS simulation to 8.9 ppm for the C_{Ken} simulation, and the root mean square errors were consequently very similar for the two simulations (approximately 27 ppm).

Table 3.4 shows that use of C_{Ken} as the upper boundary condition improved model performance the most in the high-CO_2 periods, somewhat less in the low-CO_2 periods, and not at all in the variable-CO_2 periods.

It is concluded that C_{Ken} contains some variations of potential relevance to nocturnal residual layer variability, but was an overcorrection when applied to the PCAPS period. The bias aside, the improvement in model r^2 suggested that substantial gains in modeling performance may be realized via a more sophisticated analysis and treatment of CO_2 variability above the mixed layer, especially under stable conditions conducive to accumulation of CO_2 in the nocturnal residual layer.

3.5 Conclusions and Discussion

An in-depth observational and modeling study was undertaken to explain the variability of CO_2 in the urban Salt Lake Valley (uSLV) during the winter of 2010-2011, corresponding to the Persistent Cold Air Pool Study (PCAPS). Intensive observation periods during PCAPS included three-hourly atmospheric soundings and continuous laser celiometer measurements. In addition, an existing multisite network of CO_2 observations was supplemented with quasivertical profiles of CO_2 collected by ascending steep topography on foot or by vehicle.

PCAPS was divided into periods of prolonged high CO_2 ($\geq 66^{\mathrm{th}}$ percentile), low CO_2 ($\leq 33^{\mathrm{th}}$ percentile), and variable CO_2 based a 48-hour running average of CO_2 mole fraction averaged across the uSLV stations. Atmospheric influences on CO_2 variability were then investigated observationally using data collected during the intensive observation periods. In addition, CO_2 variability was simulated using a multiple-box model (Strong et al., 2011) forced by surface winds, mixing heights derived from atmospheric soundings, an anthropogenic emissions data set, and an empirical biological flux.

Periods in which uSLV CO_2 mole fractions (C_{obs}) were high were dominated by lower than average mixing heights, large anthropogenic flux, and low wind speed. The largest nighttime peaks in CO_2 were due to extremely high surface stability, moderate nighttime peaks were due to mixing under an elevated cloud-top inversion, and low nighttime values were due to the absence of strong nocturnal stability. The high-CO_2 periods ended with either a gradual weakening of stability or a synoptic storm passage providing a rapid mixing out of valley air.

On weekly time scales, C_{obs} was positively correlated with CO_2 mole fractions measured at the rural Kennecott site (C_{Ken}) because prevailing atmospheric conditions extended spatially to encompass both sites and the urban CO_2 dome expanded to influence Kennecott on time scales longer than a day. In contrast, C_{obs} and C_{Ken} were inversely correlated on diel time scales. Specifically, during periods of high CO_2, C_{Ken} tended to remain lower at night when C_{obs} was increasing due to anthropogenic CO_2 emissions into a shallow nocturnal boundary layer. As the mixing depth

increased during the day, C_{obs} tended to decrease in response to lower-concentration air being mixed in from higher elevations, and C_{Ken} tended to increase in response to higher-concentration air being mixed in from lower elevations.

Results for mole fractions a the Hidden Peak mountain site (C_{Hid}) were notably different. First, C_{Hid} and C_{obs} were inversely correlated overall and on weekly time scales because increases in C_{Hid} required venting of the valley air by synoptic conditions conducive to lower C_{obs}. Second, on diel time scales, C_{Hid} and C_{obs} were not correlated because the daytime growth of the mixed layer did not typically span the elevation difference between the valley floor and Hidden Peak.

Periods of low C_{obs} were dominated by strong winds and higher than average mixed layer growth. Low periods ended when advection and entrainment were insufficient for maintaining low CO_2 mole fractions in the uSLV. During periods of low C_{obs}, C_{Ken} remained largely inversely correlated with C_{obs}. Due to continual advection of uSLV air, C_{Hid} was above average, remaining inversely proportional to C_{obs}.

Periods of variable C_{obs} had a mixture of conditions described above, lacking the sustained mechanisms responsible for periods of low or high CO_2.

The multiple-box model accounted for 33% of C_{obs} on an hourly basis and 85% of the C_{obs} mean diel cycle. The performance of the multiple-box model during PCAPS was low relative to its overall performance during the preceding five years ($r^2 = 0.33$ versus $r^2 = 0.53$). However, considering "winter simulations" (PCAPS plus the preceding four winter periods matching the PCAPS dates), model performance during PCAPS was not atypical (winter-simulation performance ranged $0.28 \leq r^2 \leq 0.39$). Also for the winter simulation, model r^2 was higher for winters with larger observed ranges of CO_2, yet the model's negative bias also strengthened linearly with increases in the observed range of CO_2.

An experiment was conducted to investigate potential importance of CO_2 variations in the nocturnal residual layer which was drawn into the mixed layer during its daytime growth. Using raw data from the Kennecott site (C_{Ken}) rather than a smooth harmonic fit to the annual cycle of C_{Ken} for the upper boundary condition C_h improved model r^2 from 0.33 to 0.45 for PCAPS, suggesting that an upper boundary condition with more realistic variations could potentially advance understanding and model performance.

The multiple-box model captured only 15% of hourly cycle of C_{obs} during periods of low C_{obs}. The model performance did increase slightly to 18% when specifying raw C_{Ken} as the upper boundary condition. The multiple-box model's failure to capture the consistent low periods stemmed in part from simplifications underlying its construction and also the likelihood that the parcel method underestimated mechanically-driven mixing depths during higher wind speeds.

As urban centers grow and emit increasing amounts of greenhouse gases and pollutants, it is important to understand the sources and the meteorological controls on their cycling. Observational analyses such as those presented here can inform development of government policy, and models such as the one used here can inform future city planning under projected changes in climate and urban development, where the latter may be designed to include improved building efficiencies, reduced emissions, and establishment of biological or engineered CO_2 sinks. Within the PCAPS framework, the research presented here was developed specifically for an urban valley, but provided findings on principal CO_2 controls of potential relevance to a broader class of urban settings.

Table 3.1. IRGA Controls

Control	Description	Experimental Design
Enable Heater	Heater should always be on	ON
Pressure Compensation	Enable the Pressure Compensation check box to correct concentration values during changes in cell pressure.	ON
DAC Offset Enable	The DAC Offset Enable check box determines whether the analog output voltage includes a zero offset. The DAC in the LI-800 only allows positive analog values even if the apparent CO_2 mole fraction reads negative in the software. This could happen if the cell becomes contaminated. If the DAC offset is disabled, a voltage output of 0 ppm would correspond to an analog voltage of 0 volts. Enabling the DAC offset allows one to identify a negative zero drift. A negative 25 ppm offset is available for the 0-1000 ppm and 0–2000 ppm range, and a negative 100-ppm offset for the 0-5000 and 0–20000 ppm ranges.	OFF
Span	The span (range) buttons determine the maximum CO_2 range over which the IRGA will make measurements. If the 13.97-cm optical bench is installed, 5000 ppm and 20000 ppm will be grayed out, and if the 5.08-cm optical bench is installed, 1000 ppm and 2000 ppm will be grayed out. The narrower the range, the better the resolution in terms of the DAC.	0-1000 ppm
Reset LI-800	The Reset button allows one to set the parameters back to the default settings. This also happens every time the program is started. The zero and span values are set to 1, alarms are set to Off, heater is enabled, pressure compensation is disabled, and DAC offset is reset to zero. The software signal filtering is set to 20 seconds, span values are set to the maximum values depending upon size of optical bench installed. Calibration polynomial coefficients are also loaded when the IRGA is Reset.	Every time program restarts

Table 3.2. Mean meteorological surface variables during periods of extended high and low CO_2 mole fractions. CO_2 is given in ppm, mixing heights (h) are given in meters above ground level (magl), wind speed (V) is given in m s^{-1}, the anthropogenic CO_2 flux (Q_a) is given in 10^{-6} kg m^{-2} s^{-1}, and times are LST.

Period	Start date	end date	IOP	h	V	Q_a
H1	06:00 on 01 Dec 2010	01:00 on 10 Dec 2010	IOP 1	274	1.166	0.4779
H2	20:00 on 03 Jan 2011	10:00 on 09 Jan 2011	IOP 5	329	1.026	0.5816
H3	04:00 on 11 Jan 2011	22:00 on 16 Jan 2011	IOP 6	241	1.300	0.5425
L1	23:00 on 28 Dec 2010	08:00 on 01 Jan 2011	N/A	296	2.183	0.4546
L2	15:00 on 18 Dec 2010	22:00 on 21 Dec 2010	N/A	303	1.375	0.4572
L3	01:00 on 18 Jan 2011	02:00 on 21 Jan 2011	N/A	258	3.748	0.5620
L4	00:00 on 23 Dec 2010	22:00 on 25 Dec 2010	N/A	613	2.4322	0.4874
L5	09:00 on 30 Jan 2011	16:00 on 03 Feb 2011	N/A	753	3.182	0.5668
PCAPS	1 Dec 2010	7 Feb 2011	All	384	1.71	0.5098

Table 3.3. Maximum, minimum, and mean CO_2 mole fractions during periods of extended high and low CO_2 mole fractions and the PCAPS period. The locations of uSLV, Kennecott, and Hidden Peak are defined in Fig. 3.1a.

	uSLV			Kennecott			Hidden Peak		
Period	min	mean	max	min	mean	max	min	mean	max
H1	406.5	464.6	599.2	394.0	414.3	453.8	388.4	391.7	394.5
H2	420.5	472.4	564.7	402.9	437.6	491.7	391.1	392.9	400.6
H3	422.6	461.7	543.5	396.6	419.2	460.2	392.4	393.7	397.2
L1	395.8	411.9	444.3	393.3	399.7	422.1	392.3	394.0	396.4
L2	403.6	417.4	435.6	395.5	405.6	421.7	390.8	392.7	394.9
L3	399.4	411.8	467.4	396.4	400.4	406.8	392.0	395.5	400.2
L4	396.7	416.9	471.3	395.5	399.6	406.1	392.6	394.0	397.0
L5	398.5	416.6	478.6	398.4	407.0	437.8	392.4	395.6	400.6
PCAPS	395.8	439.9	599.2	392.9	411.0	491.7	388.4	393.4	400.6

Table 3.4. Hourly performance of PCAPS and C_{Ken} simulations using the squared Pearson correlation coefficient (r^2).

Period	PCAPS simulation	C_{Ken} simulation
High	0.31	0.35
Low	0.15	0.18
Variable	0.17	0.17

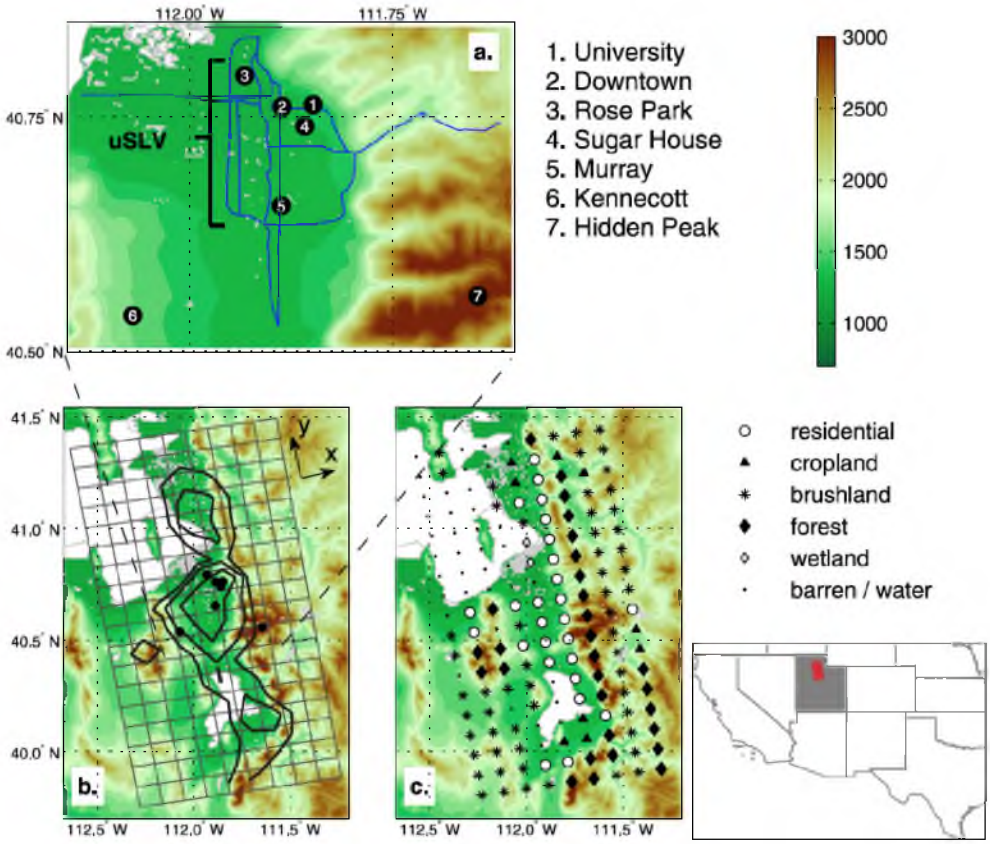

Figure 3.1. The domain of the multiple-box model. a) The sites with CO_2 observations. Sites 1-5 are called the urban Salt Lake Valley (uSLV) sites. b) The model domain with averaged anthropogenic CO_2 emissions in contours and the CO_2 observational network as the black dots. c) The model domain split into ecosystems. Adapted from Strong et al. (2011)

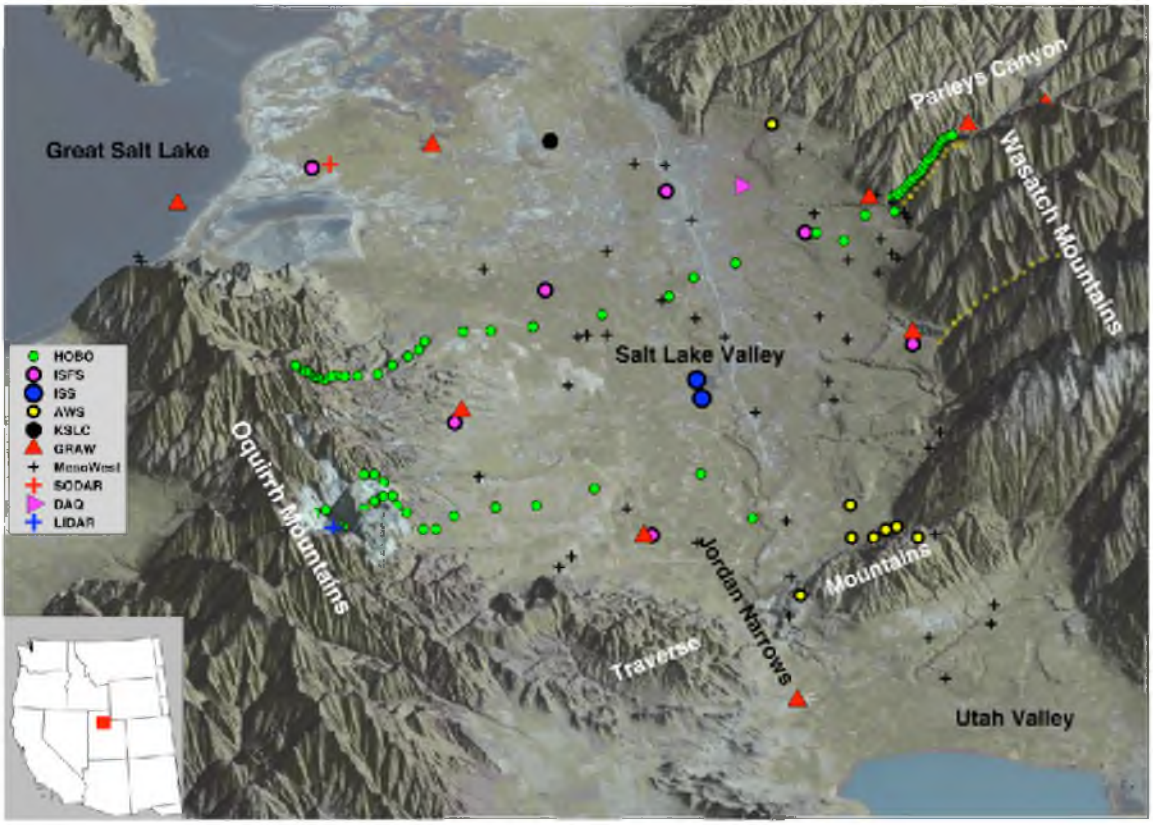

Figure 3.2. Locations of measurements during PCAPS. The Salt Lake Valley is bordered by the Wasatch to the east, the Oquirrhs to the west, the Great Salt Lake to the north, and the Traverse Mountains to the south. There is a small section called the Jordan Narrows which allows drainage flow out of the Salt Lake Valley. Adapted from Lareau et al. (2012)

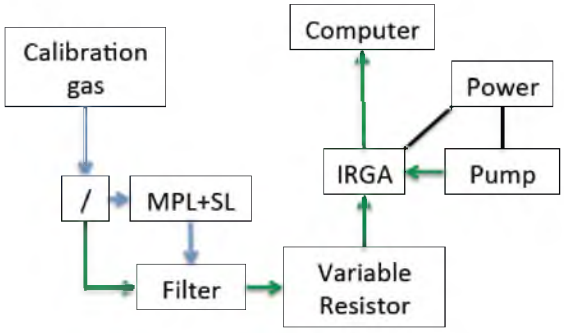

Figure 3.3. Schematic showing the test setup for the IRGA used to test the pressure compensation feature.

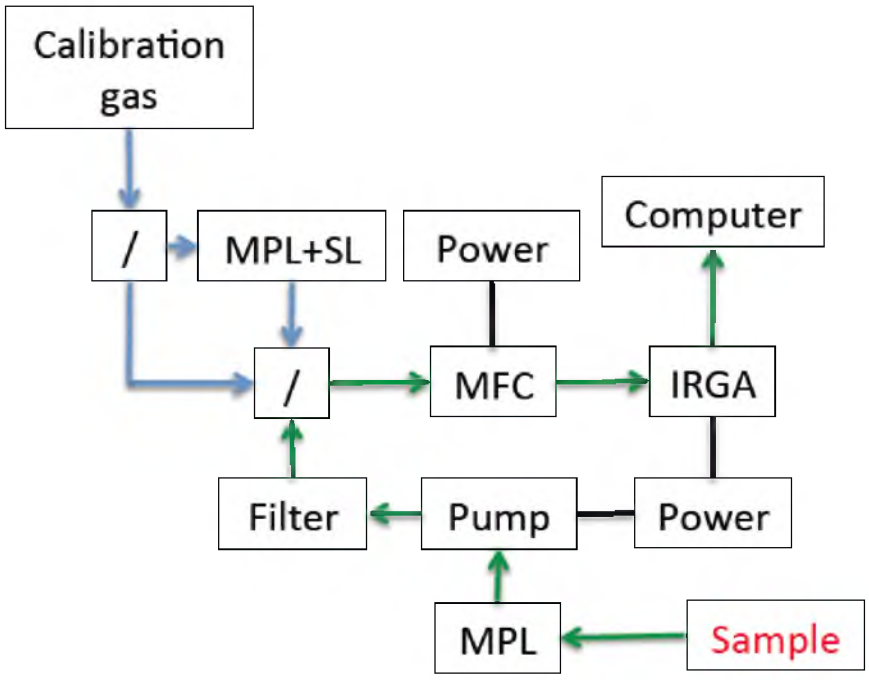

Figure 3.4. Schematic of field CO_2 equipment. The calibration gas and the sample intake tube are in different locations for ease and speed of calibration and sampling valvues offs. The blue arrows indicate the calibration process, the green arrows indicate the path of the air sample, and the black arrows indicate the instruments that needed to be powered.

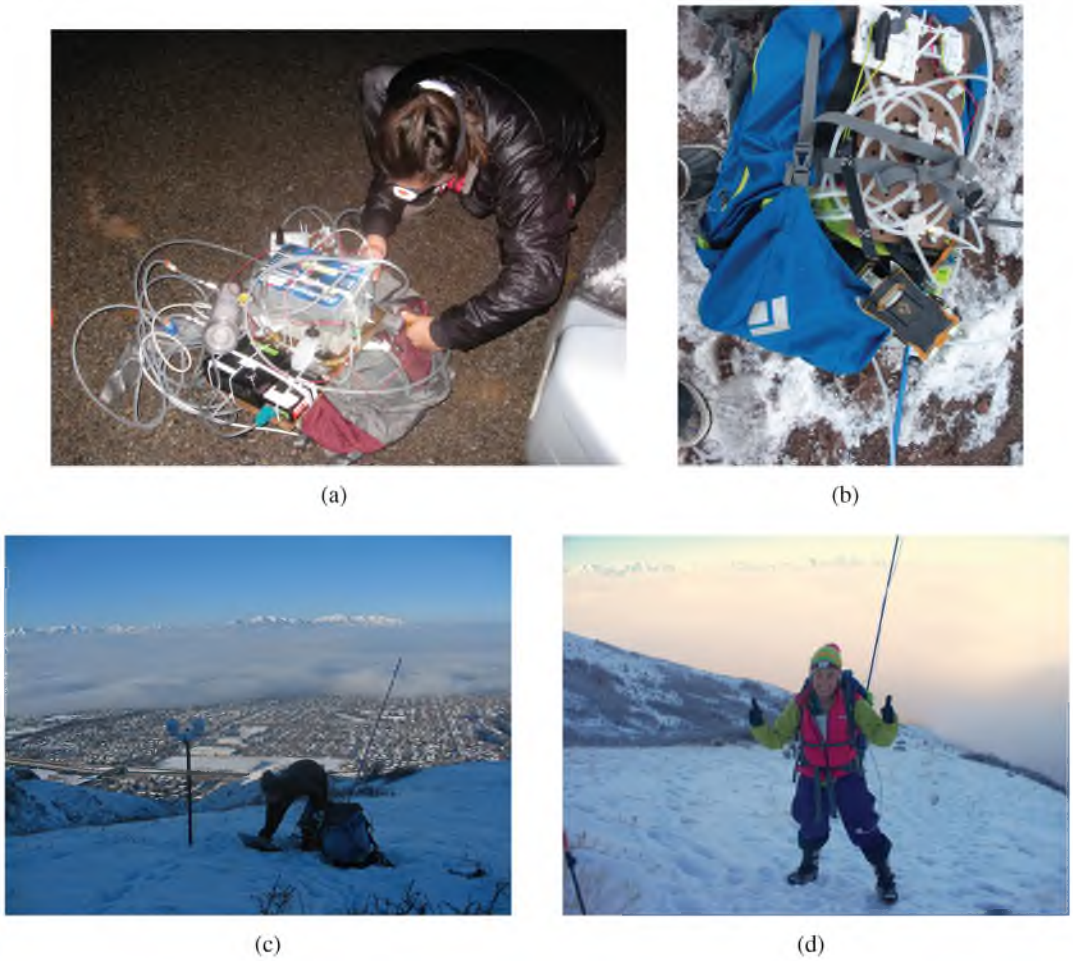

Figure 3.5. Images from field work, (a) C. Stwertka making final preparations for the quasivertical transect, (b) control panel that controlled calibration and sampling processes from the outside of the backpack, (c) calibrating the IRGA at one of the HOBO® locations at 6:00 LST on 26 January, (d) experimental setup with IRGA running in the backpack connected to the computer and the intake tube protruding out of the backpack.

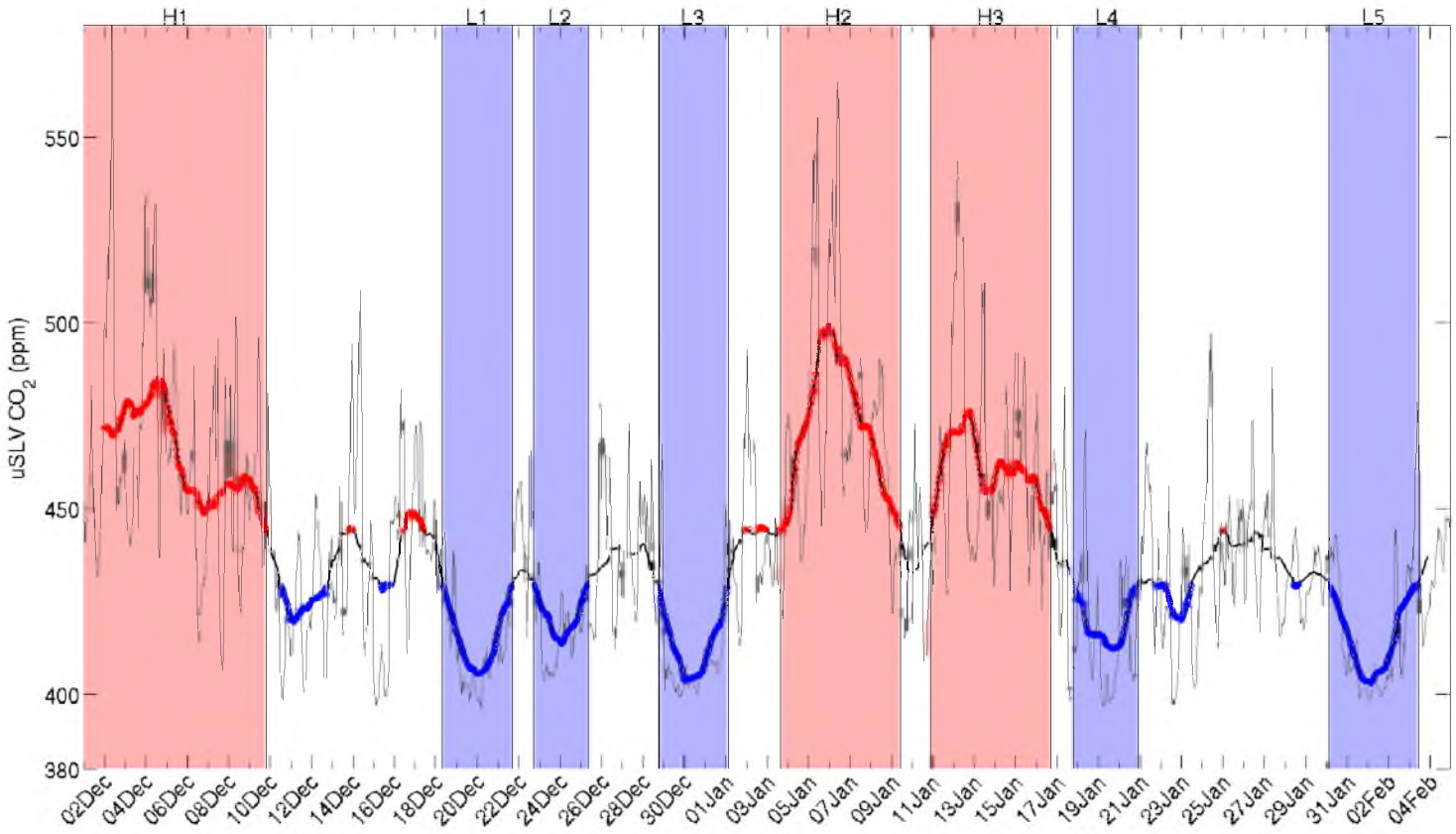

Figure 3.6. Defining High and Low Quartiles with the arithmetic mean of CO_2 across the uSLV sites (C_{obs}, thin black curve), and the 48-hour running mean of C_{obs} (bold black curve). Red circles indicate values above the 66th percentile of C_{obs}, and blue circles indicate values below the 33rd percentile of C_{obs}. Shading indicates "high-CO_2" periods (red), "low-CO_2" periods (blue), and "variable-CO_2" periods (white) as defined in Section 3.3.5.

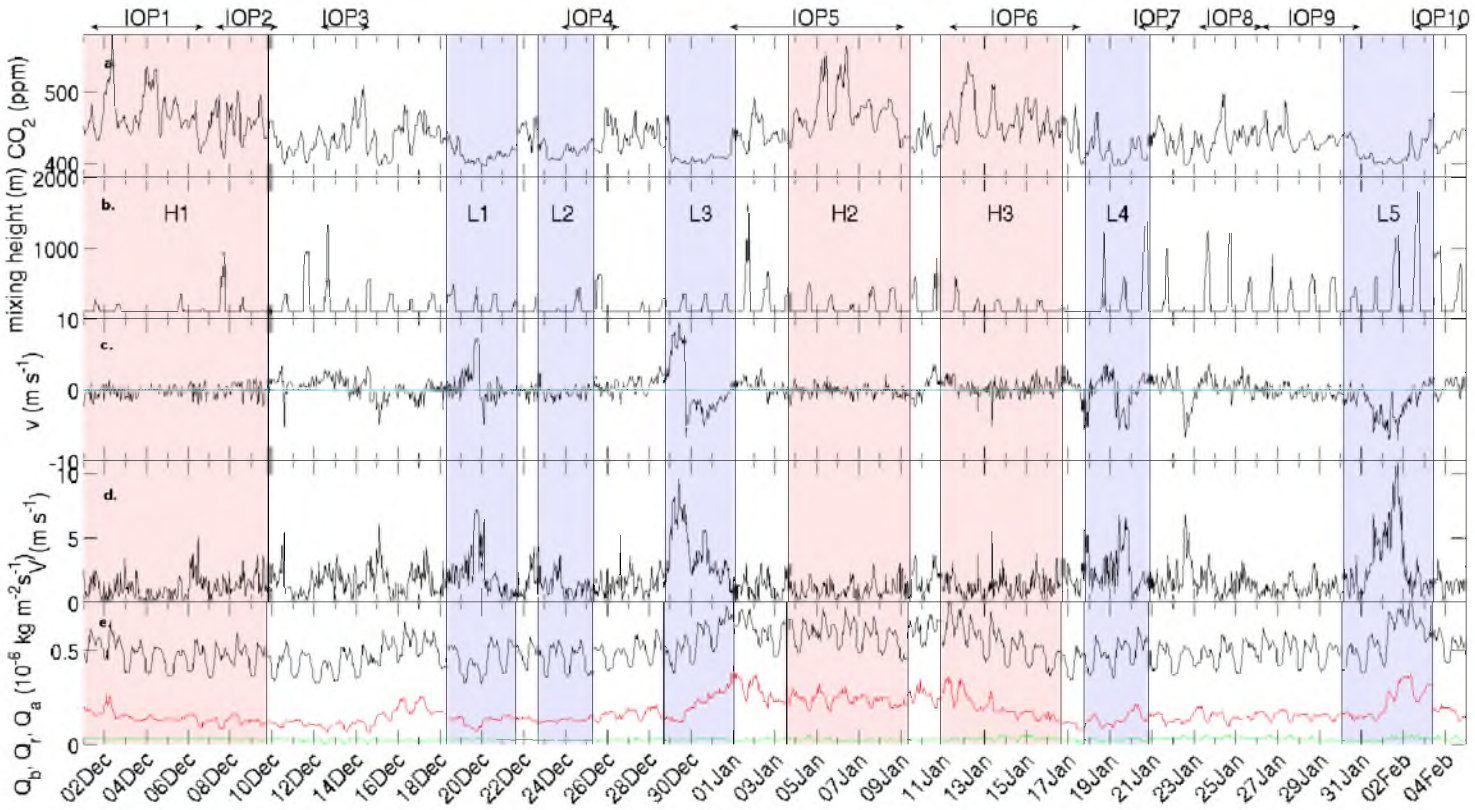

Figure 3.7. Time series of meteorological conditions for the PCAPS period in LST: (a) CO_2 mole fraction of the uSLV sites (C_{obs}). (b) Mixing heights (h). (c) Component of wind in model y direction (v, approximately northward). (d) Wind speed (V). (e) Surface CO_2 fluxes [Q_b is biological flux (green curve), Q_r is from residential natural gas combustion (red curve), and Q_a is total anthropogenic emissions (black curve)].

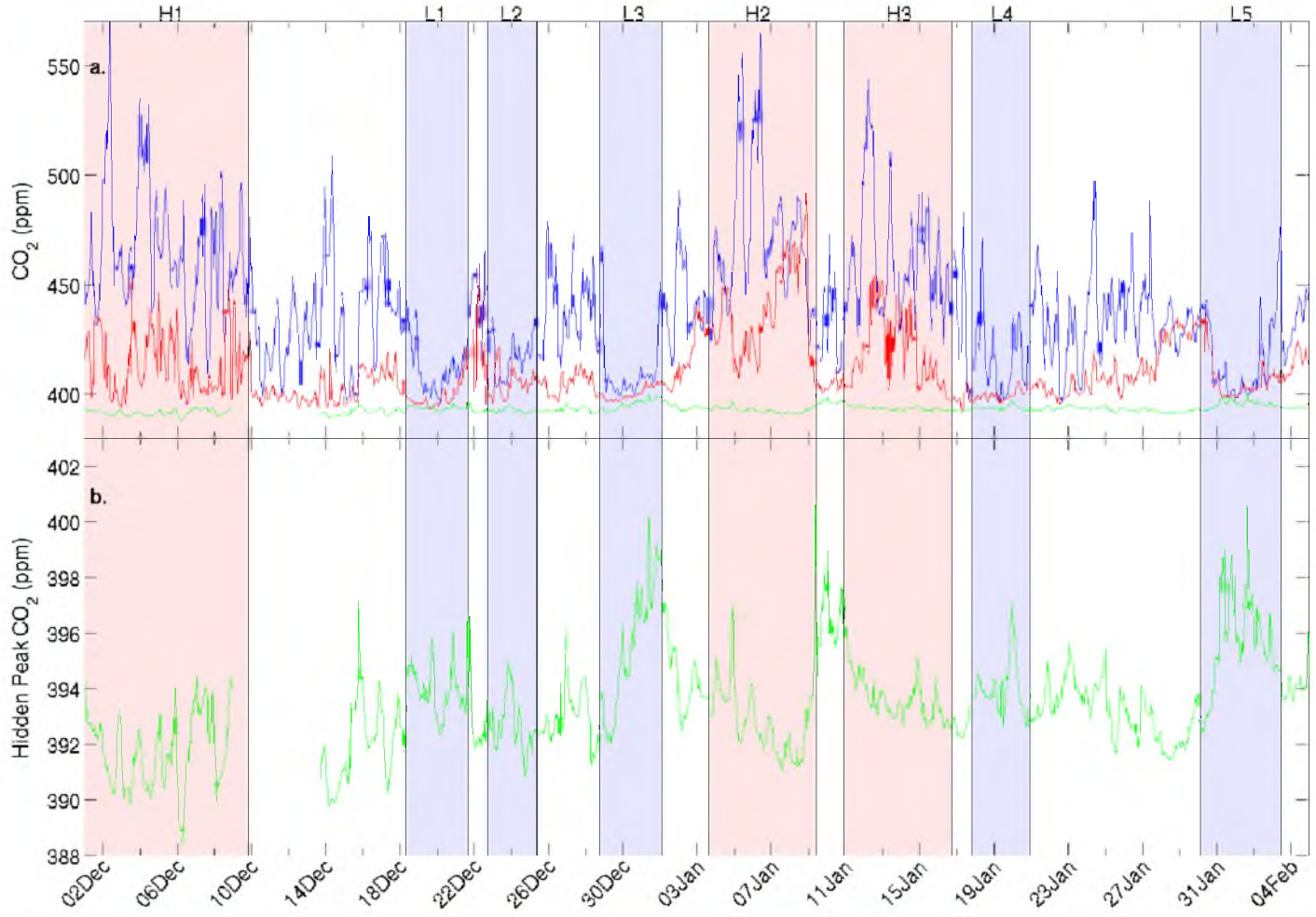

Figure 3.8. CO_2 timeseries: CO_2 mole fractions at Kennecott (C_{Ken}, red curve), at Hidden Peak (C_{Hid}, green curve), and averaged across available uSLV sites (C_{obs}, blue curve). (b) C_{Hid} enlarged for clarity.

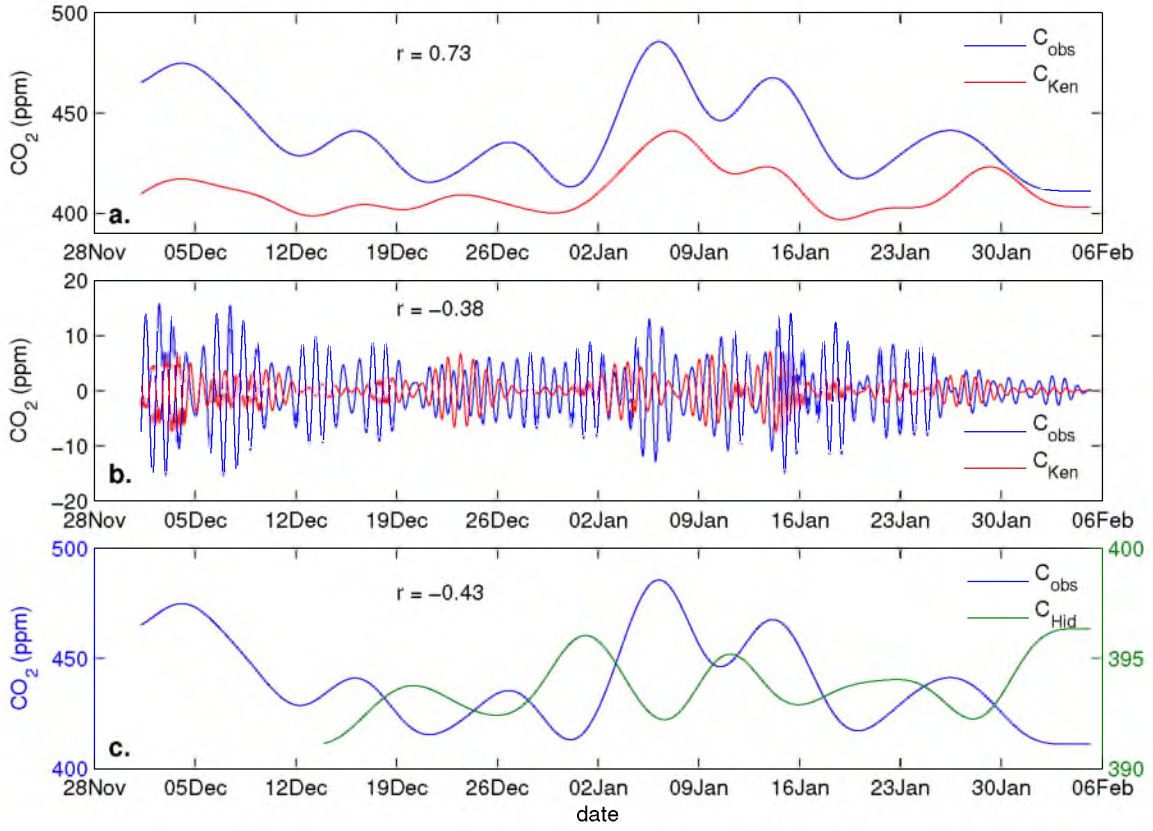

Figure 3.9. Filtered CO_2 data: (a) C_{obs} and C_{Ken} low-pass filtered with a one-week cutoff period. (b) C_{obs} and C_{Ken} band-pass filtered with cutoff periods at 18 and 24 hours. (c) C_{obs} and C_{Hid} low-pass filtered with a cutoff period of one week.

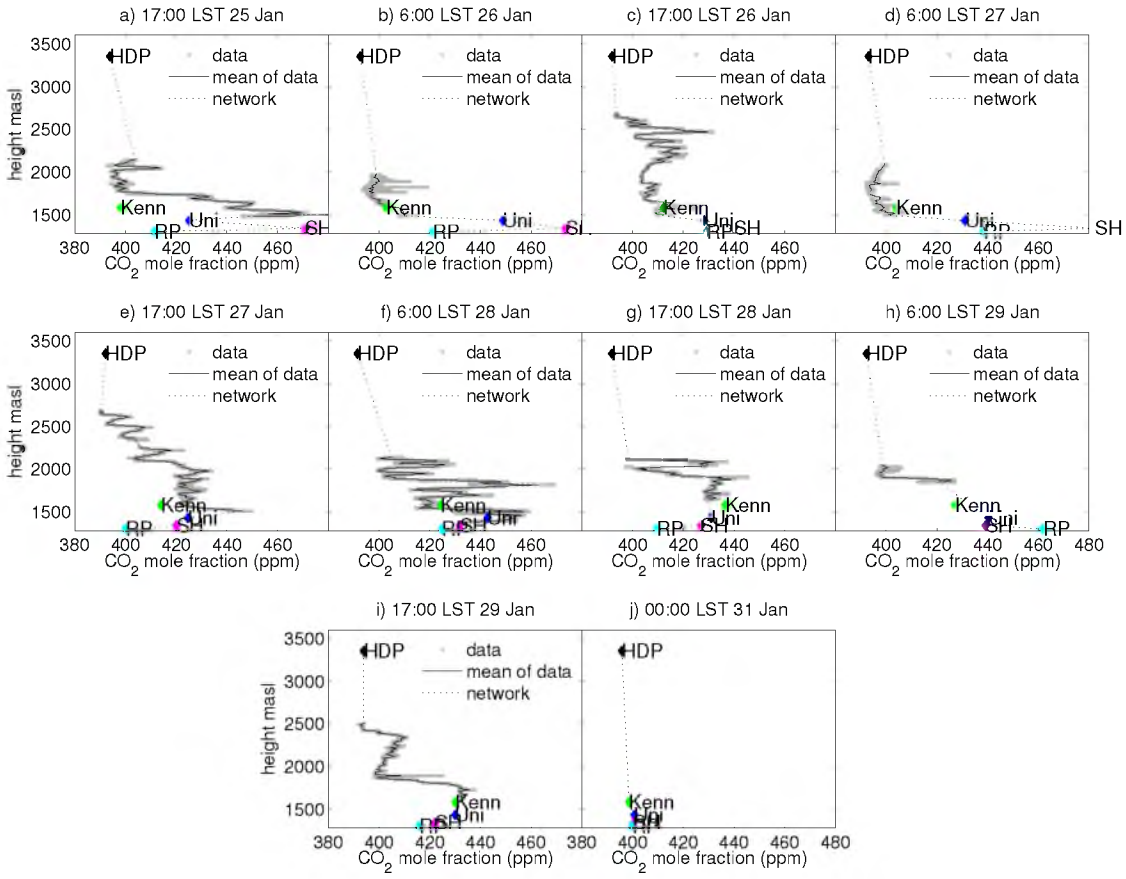

Figure 3.10. CO_2 quasivertical profiles collected during PCAPS (profile time shown above each panel). Station data are also shown at their elevation (Rosepark is the light blue diamond, Sugarhouse is the magenta diamond, University is the dark blue diamond, Kennecott is the green diamond, and Hidden Peak is the black diamond). Quasivertical profile data are shown by gray circles which merge to appear as a gray curve, and the thick black curve is a running mean. The dotted black lines span elevations without measurements.

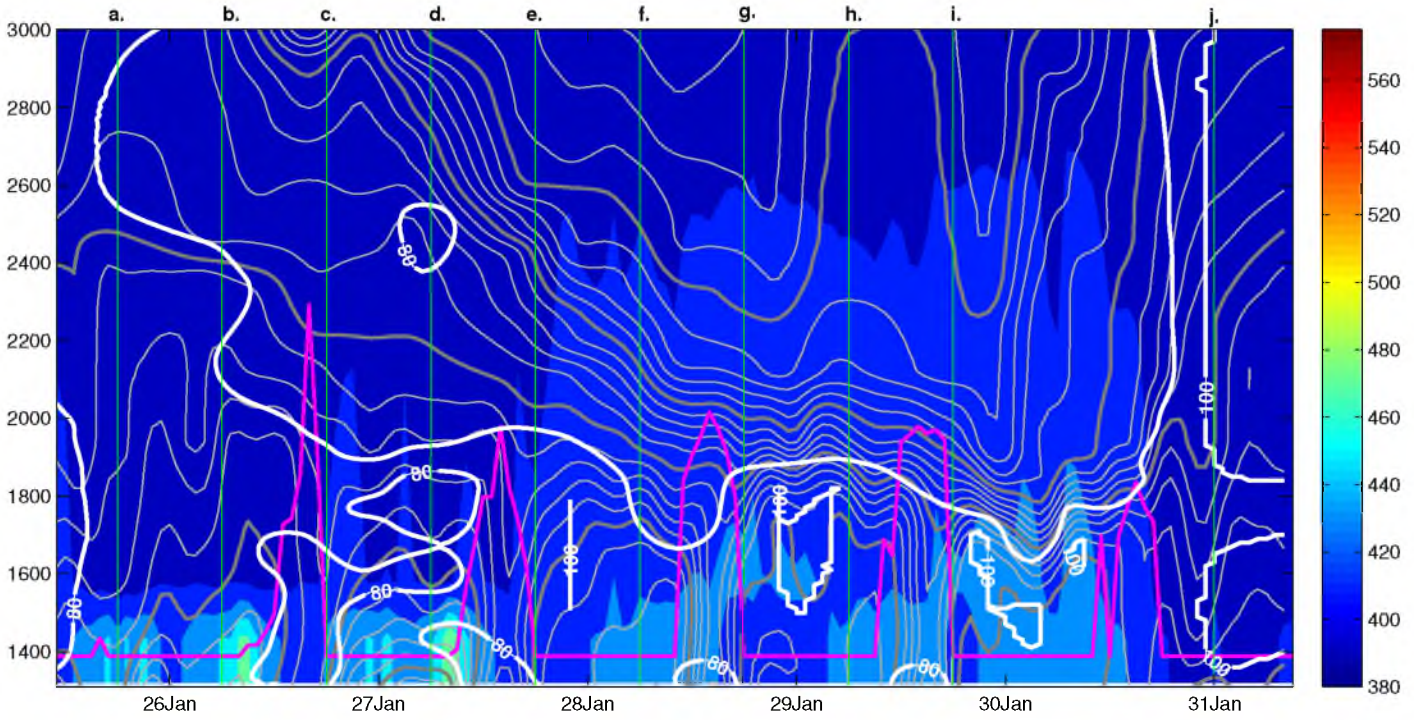

Figure 3.11. A time-height plot of IOP 9 with CO_2 mole fraction shaded (interpolation from station data). The magenta lines indicate mixed layer height (h, section 3.3.2), the white contour lines indicate 80 or 100% relative humidity (RH), and the black contours are isentropes in Kelvin (section 3.3.2).

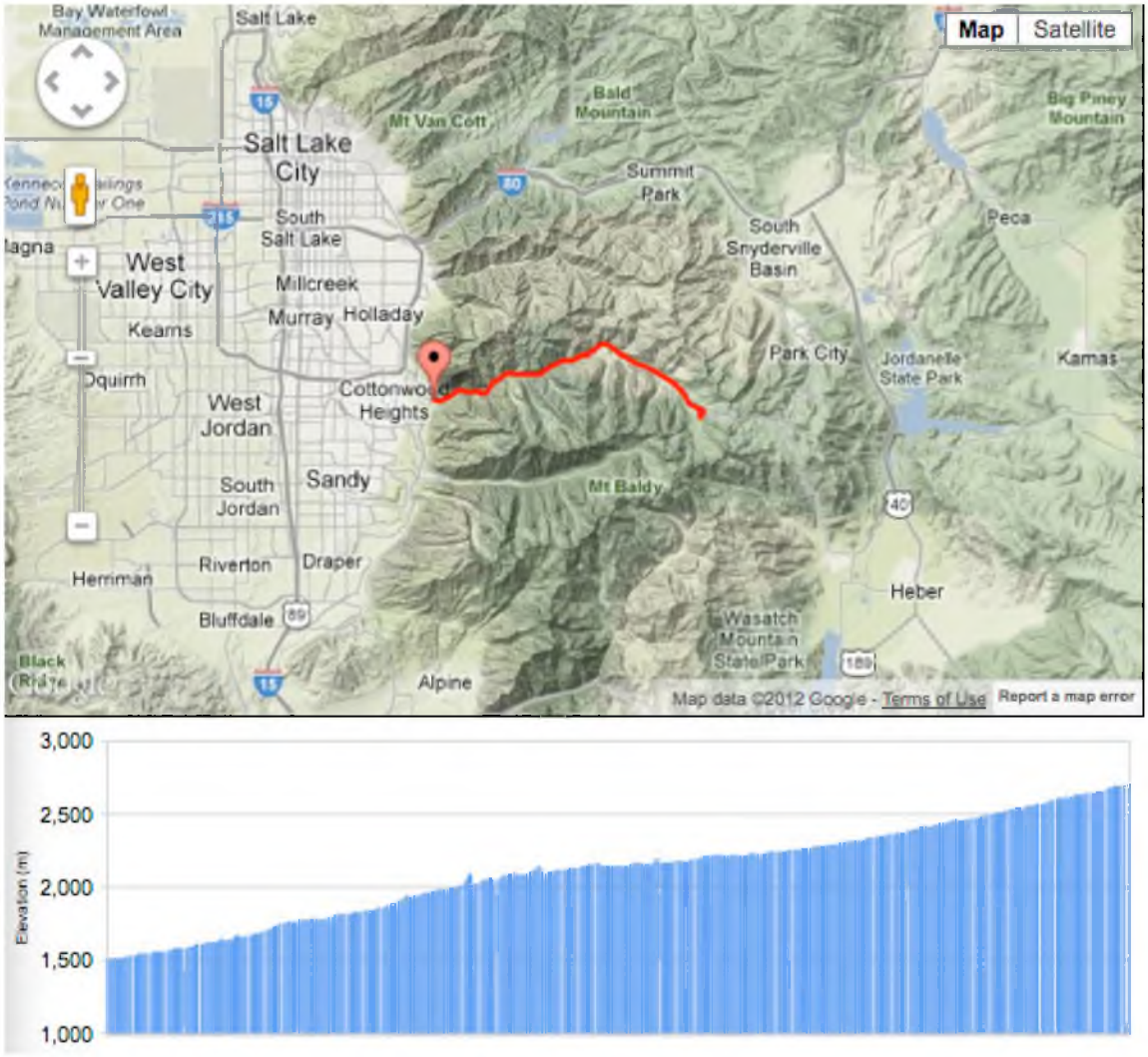

Figure 3.12. The path used for the Big Cottonwood Canyon (BCC) quasivertical transect (red curve, upper panel), and the elevation profile of the BCC quasivertical transect (blue shading, lower panel). Printed with permission from Roger Akers.

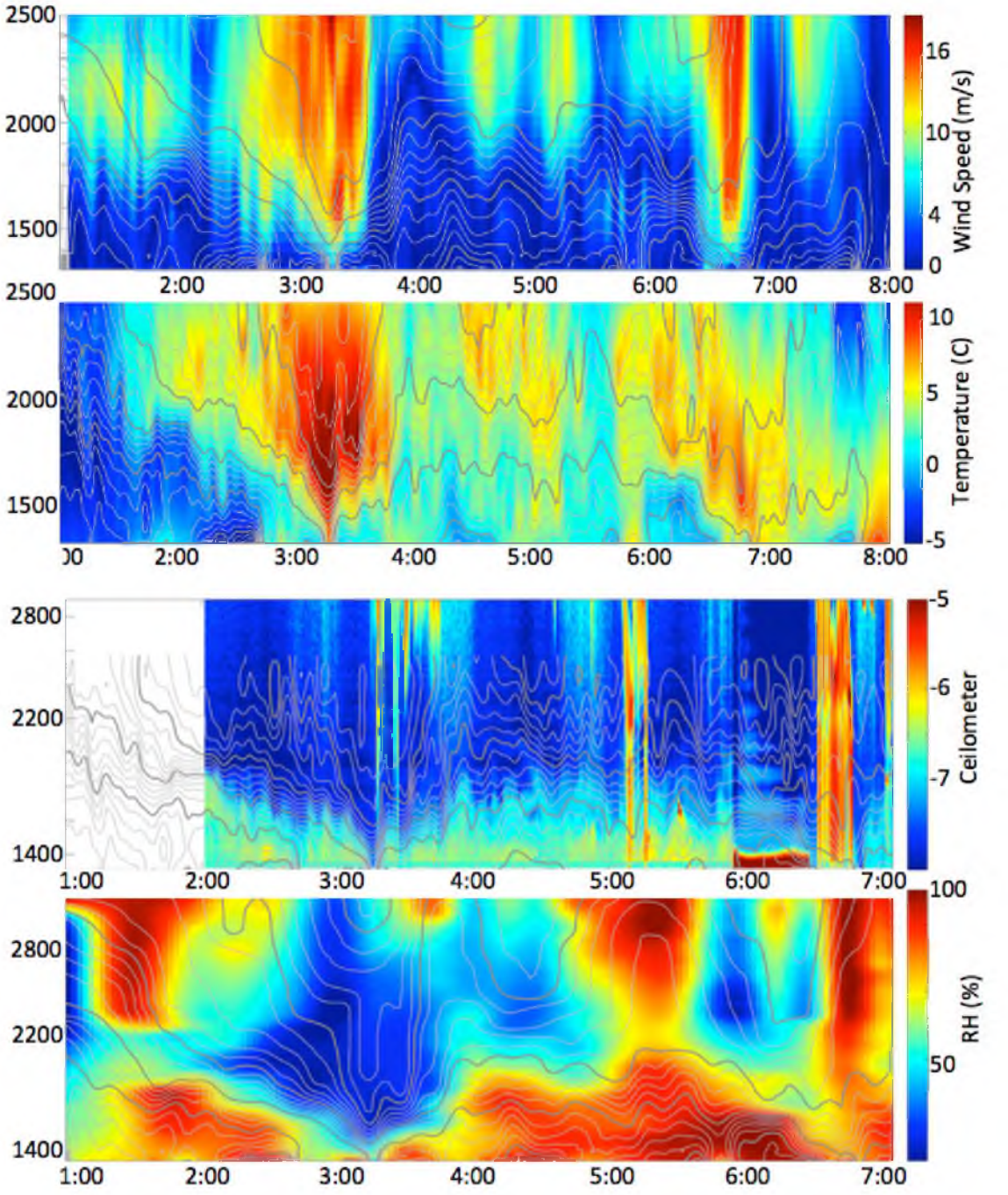

Figure 3.13. IOP1 thermodynamical time-heights. Potential temperature (contours) with (a) wind speed shaded, (b) temperature shaded, (c) ceilometer reflectivity shaded, and (d) relative humidity shaded. Printed with permission from Neil Lareau.

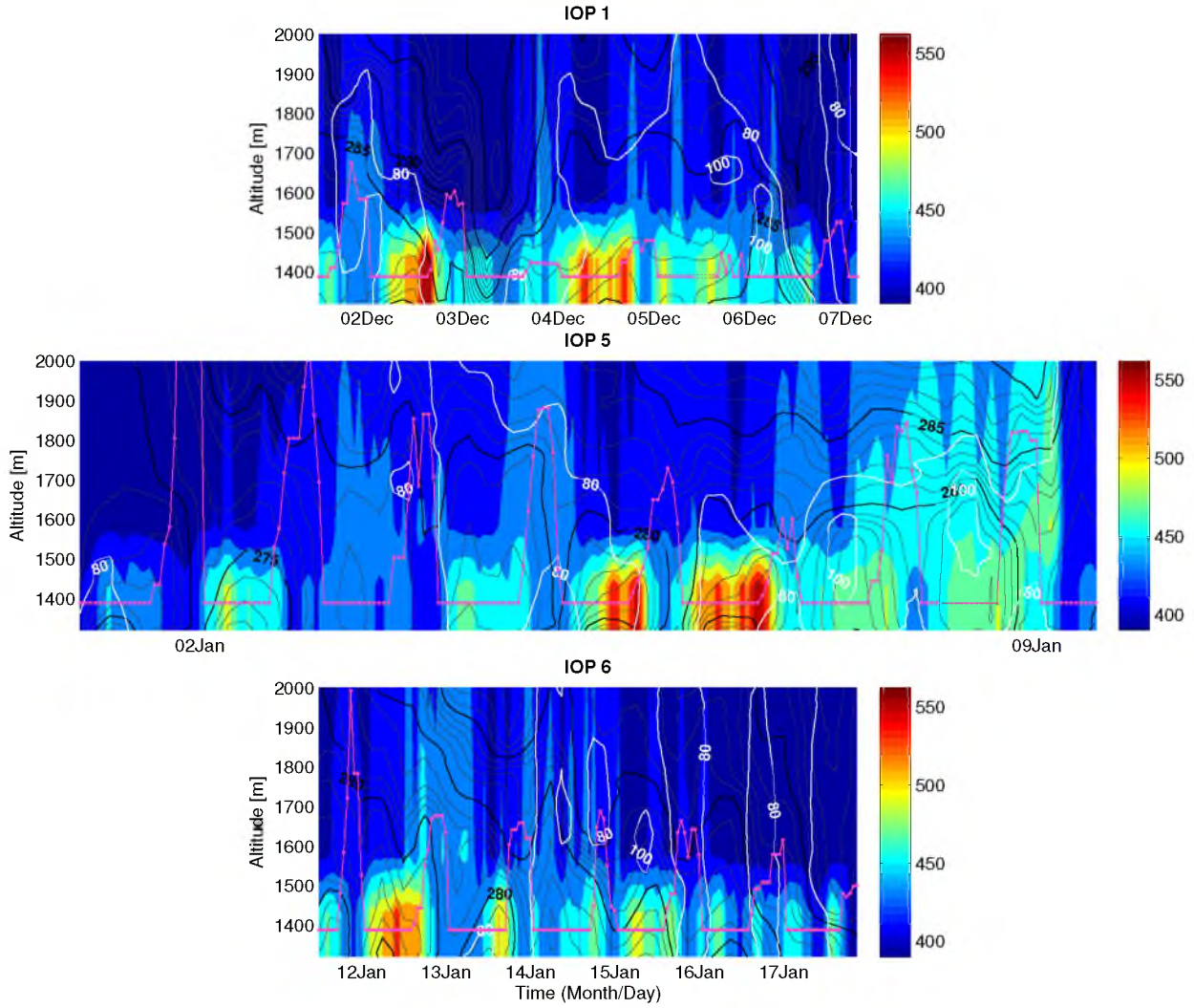

Figure 3.14. CO_2 time-heights for IOPs 1 (a), 5 (b), and 6 (c). The CO_2 mole fraction is shaded (interpolation from station data). The magenta lines indicate mixed layer height (*h*, section 3.3.2), the white contour lines indicate 80 or 100% relative humidity (RH), and the black contours are isentropes in Kelvin (section 3.3.2).

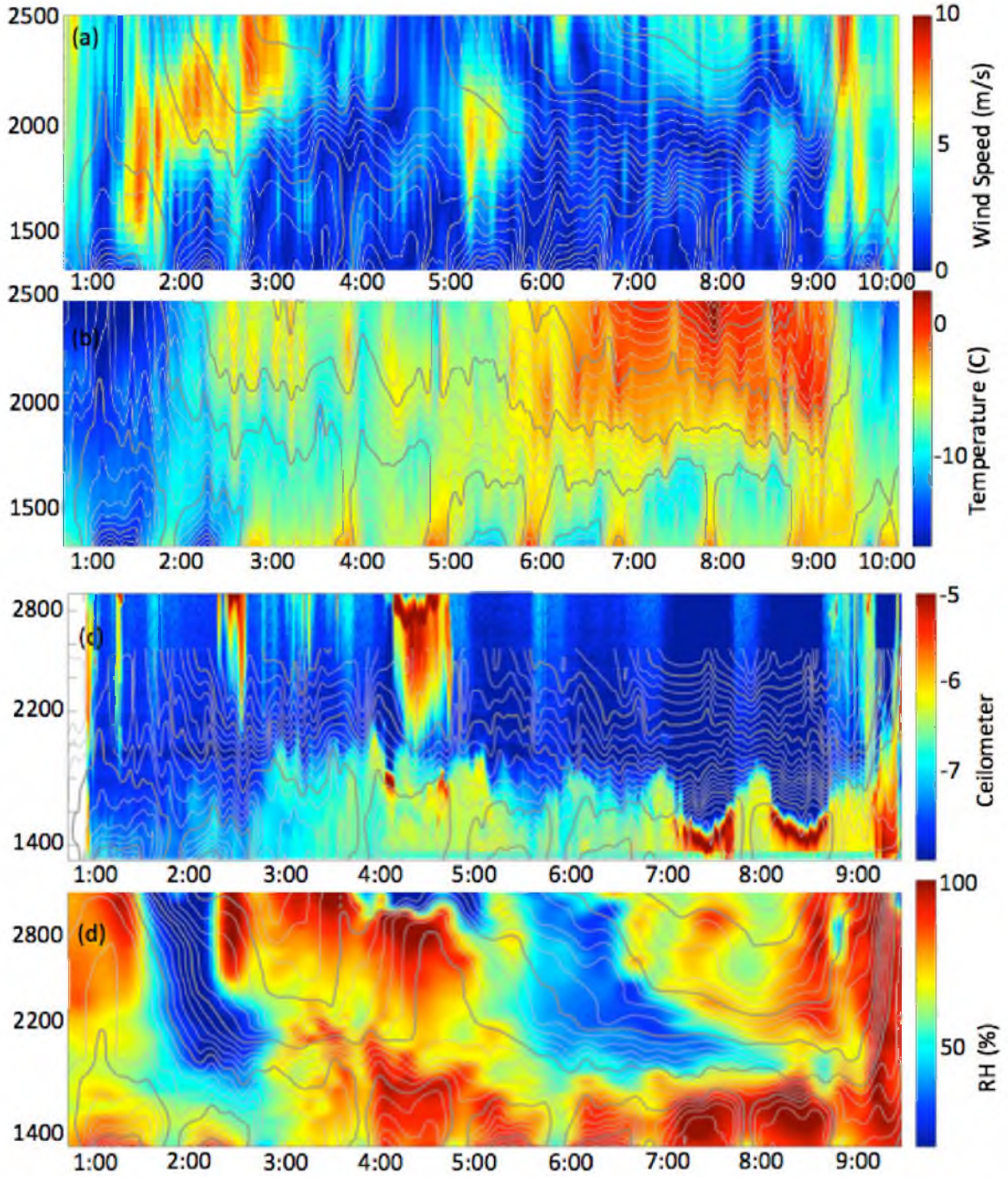

Figure 3.15. IOP5 thermodynamical time-heights. Potential temperature (contours) with (a) wind speed shaded, (b) temperature shaded, (c) ceilometer reflectivity shaded, and (d) relative humidity shaded. Printed with permission from Neil Lareau.

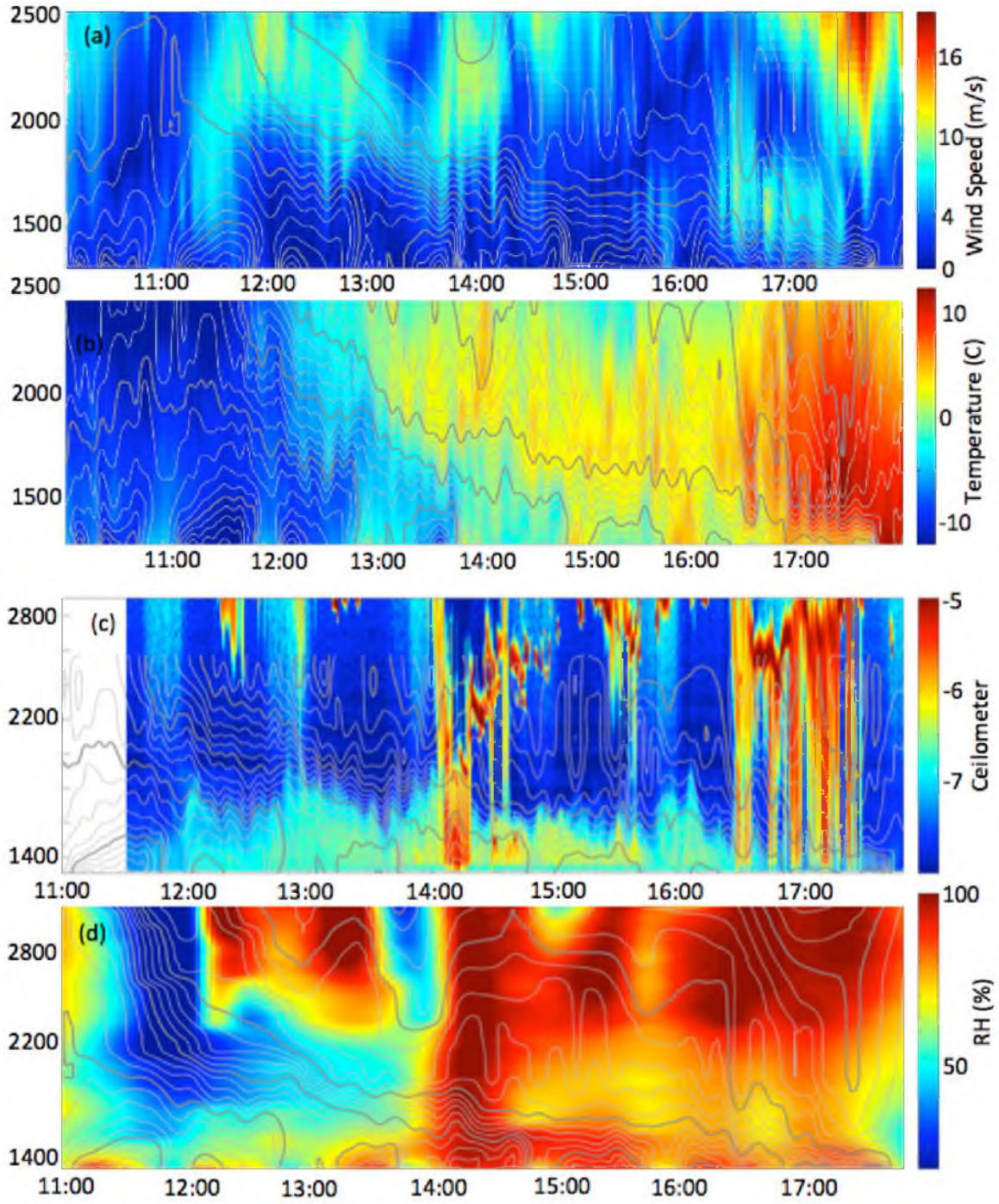

Figure 3.16. IOP6 thermodynamical time-heights. Potential temperature (contours) with (a) wind speed shaded, (b) temperature shaded, (c) ceilometer reflectivity shaded, and (d) relative humidity shaded. Printed with permission from Neil Lareau.

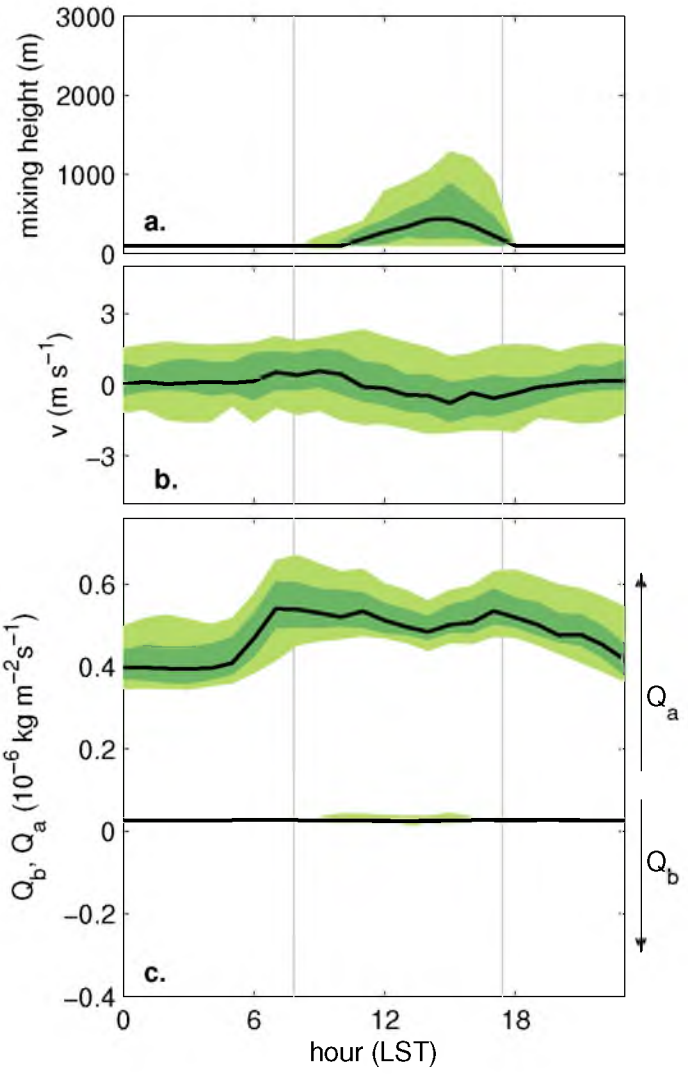

Figure 3.17. For PCAPS, mean composite diel cycles in local standard time (LST) of model forcing averaged across model boxes containing the uSLV measurement sites (Fig. 3.1a). (a) Mixed layer height (h). (b) Wind component in model-y direction. (c) Net anthropogenic flux (Q_a) and net biological flux (Q_b). For each variable, the darker shaded regions indicate the the 25$^{\text{th}}$ to 75$^{\text{th}}$ percentile, the lighter shaded regions indicate the 10$^{\text{th}}$ to 90$^{\text{th}}$ percentiles, and the bold line is the median. The vertical lines indicate sunrise and sunset times in the middle of the PCAPS period.

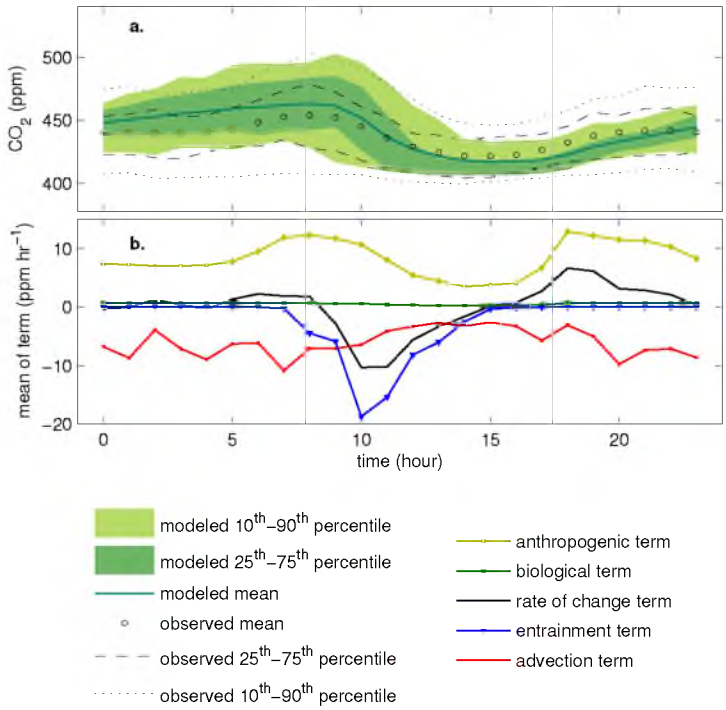

Figure 3.18. Mean diel cycle model performance for the uSLV area: (a) Diel model performance compared to observed CO_2 mole fractions for PCAPS.(b) Mean hourly values of the multiple-box model terms defined in Chapter 2. The gray vertical lines indicate sunrise and sunset as in Fig. 3.17.

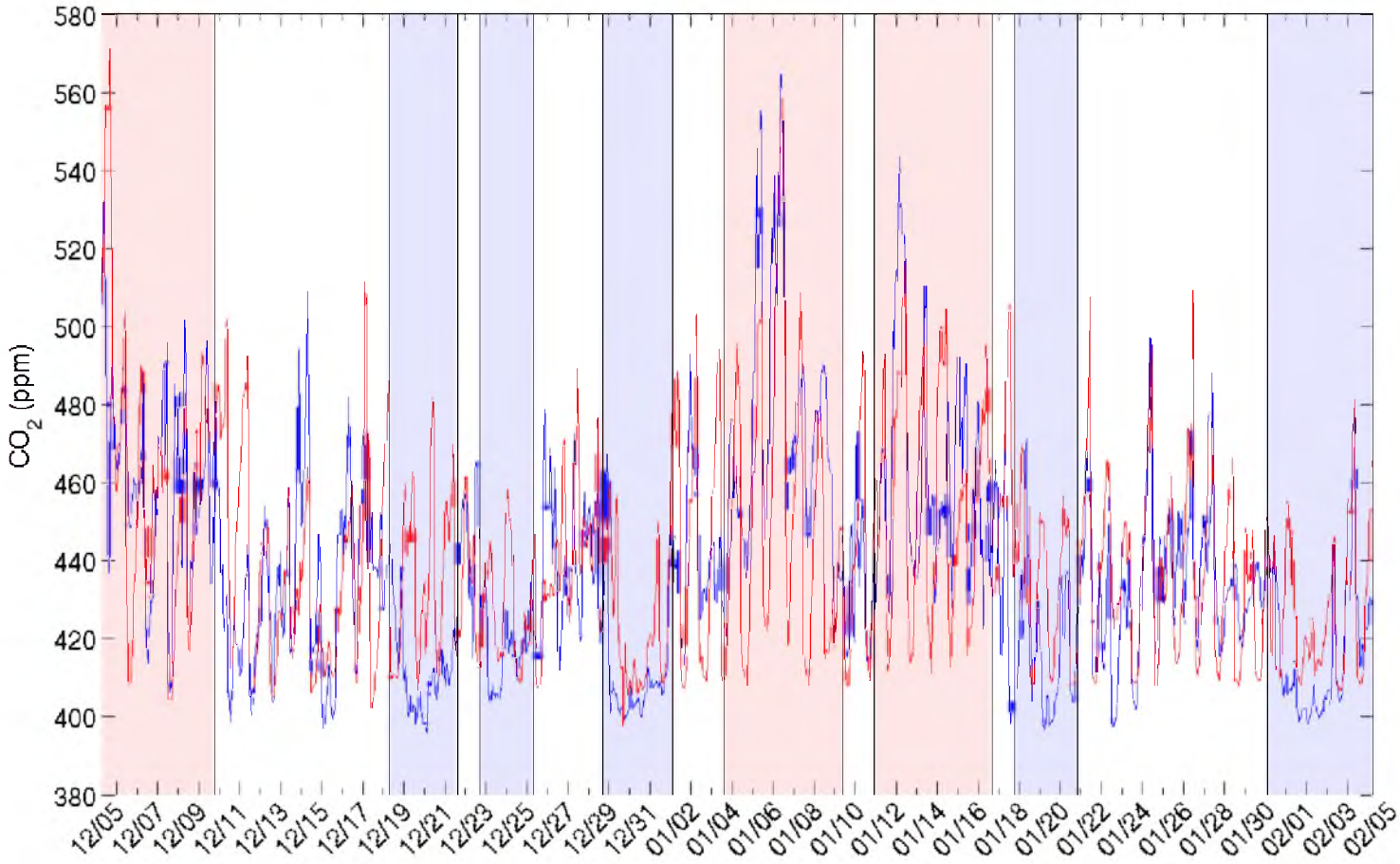

Figure 3.19. PCAPS model simulation. Hourly model output (red line) compared to hourly observations (blue line) for the uSLV sites. The model captured 33% of the hourly variability of C_{obs}. Time is in LST.

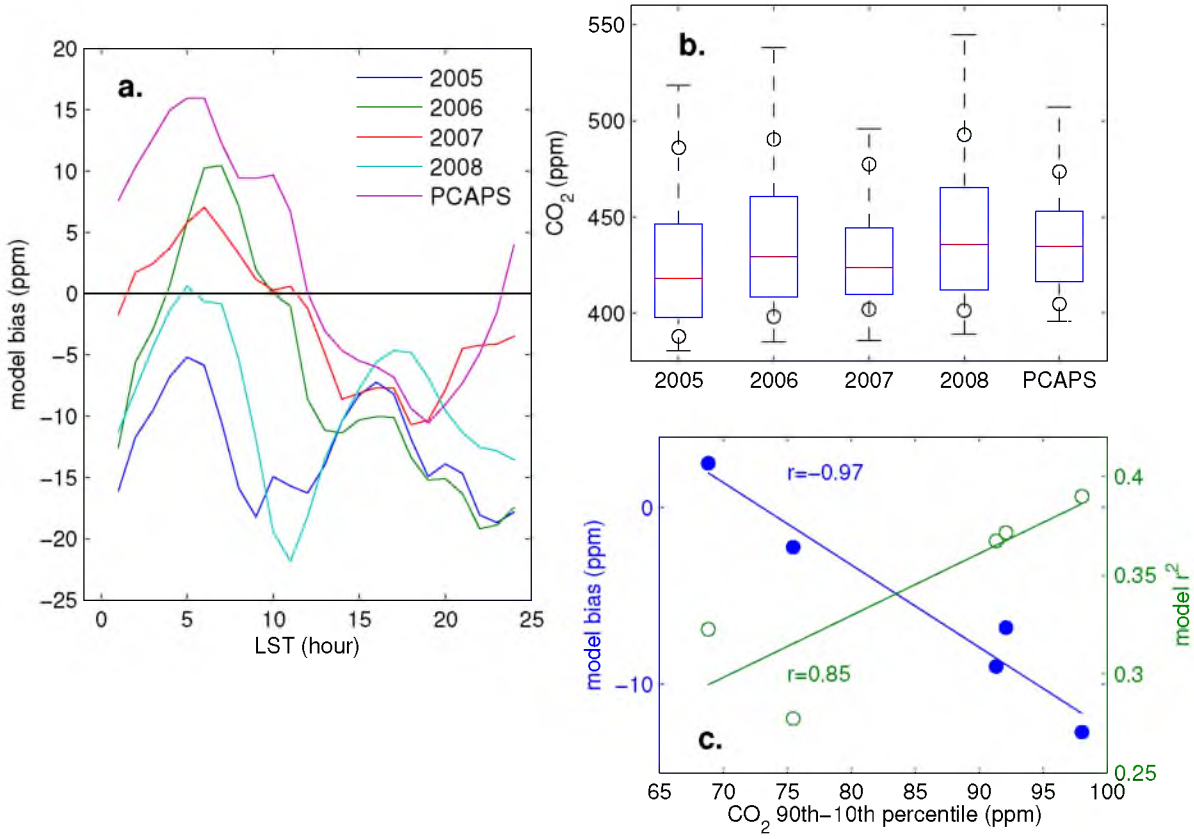

Figure 3.20. Model biases for historical winter simulations (a). Composite diel cycle of model bias for PCAPS and the preceding four winter periods corresponding to the PCAPS dates ("winter simulations"). (b) Box plots of C_{obs} for the winter simulations (red line is median, box spans interquartile range (IQR), whiskers span approximately 99% of the data, and circles show the 10^{th} and 90^{th} percentiles. (c) Model bias (blue) and model r^2 (green) plotted versus the difference between the 10^{th} and 90^{th} percentiles of CO_2 observed in the corresponding year.

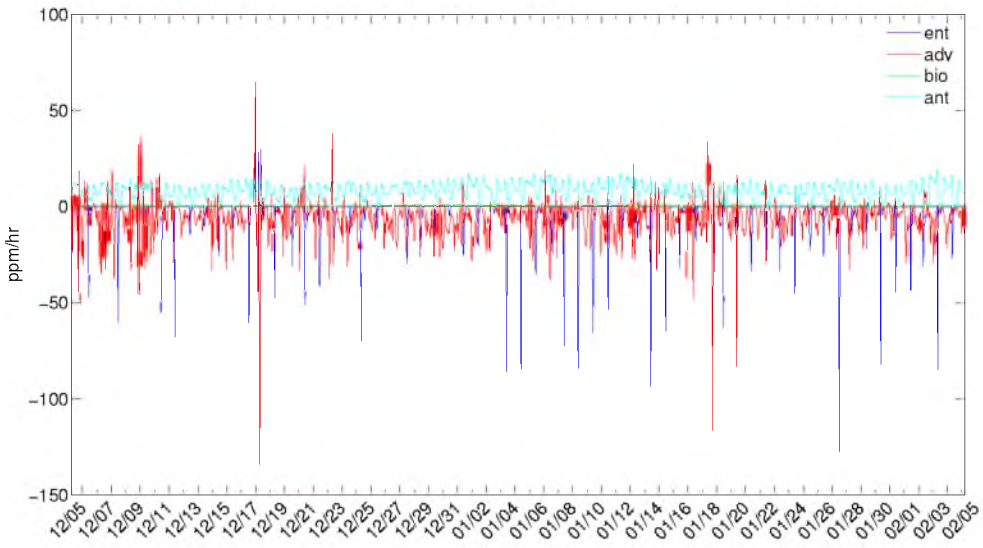

Figure 3.21. Hourly time series of the model terms defined in equation 2.2 of Section 2.1. The red line is advection term, the dark blue line is the entrainment term, the green line is the biological term, and the light blue line is the anthropogenic term.

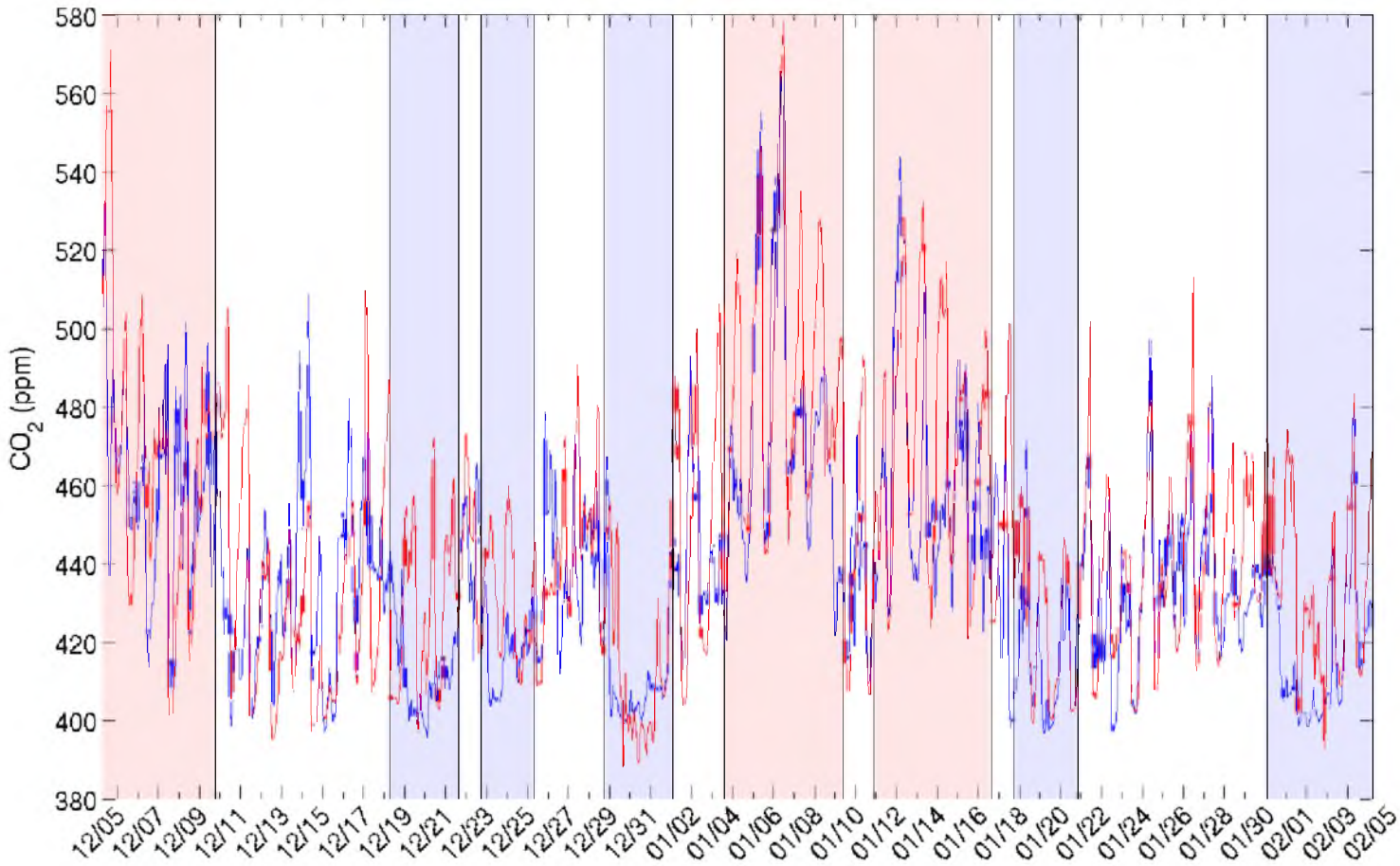

Figure 3.22. C_{Ken}model simulation. Hourly model output (red line) compared to hourly observations (blue line) for the C_{Ken}simulation defined in the text.

REFERENCES

Air Pollution Control Division, 2011: *Revised PM10 Maintenance Plan for the Steamboat Springs Attainment/Maintenance Area*. 4300 Cherry Creek Drive South Denver, Colorado 80246, Colorado Department of Public Health and Environment, 10th ed.

Akbari, H., 2005: Energy saving potentials and air quality benefits of urban heat island mitigation. *Lawrence Berkeley National Laboratory*, 19–251.

Anderson, J., H. E.E., J. Roach, and R. Witmer, 1976: *A Land Use and Land Cover Classification System for Use with Remote Sensor Data*. United States Government Printing Office.

Andres, M., J.-H. Park, M. Wimbush, X.-H. Zhu, H. Nakamura, K. Kim, and K.-I. Chang, 2009: Manifestation of the Pacific Decadal Oscillation in the Kuroshio. *Geophys. Res. Lett.*, **36**, doi: 10.1029/2009GL039216.

Apadula, F., A. Gottia, A. Piginia, A. Longhettob, F. Rocchettia, C. Cassardob, S. Ferrareseb, and R. Forzab, 2003: Localization of source and sink regions of carbon dioxide through the method of the synoptic air trajectory statistic. *Atmos. Environ.*, **37**, 3757–3770.

Balling Jr., R., R. Cerveny, and C. D. Idso, 2002: Does the urban CO_2 dome of Phoenix, Arizona contribute to its heat island? *Geophys. Res. Lett.*, **28**, 4599–4601.

Bogey, C. and C. Bailly, 2004: A family of low dispersive and low dissipative explicit schemes for flow and noise computations. *J. Comput. Phys.*, **194**, 194–214.

Bureau, U. C., 2012: State and County QuickFacts: Salt Lake City, Utah. URL `http://quickfacts.census.gov/qfd/states/49/4967000.html`, URL `http://quickfacts.census.gov/qfd/states/49/4967000.html`.

Bush, S., D. Pataki, K. Hultine, A. West, J. Sperry, and J. Ehleringer, 2008: Wood anatomy constrains stomatal responses to atmospheric vapor pressure deficit in irrigated, urban trees. *Oecologia*, **156**, 13–20, doi:10.1007/s00442-008-0966-5.

Butterworth, S., 1930: On the theory of filter amplifiers. *Experimental Wireless & the Wireless Engineer*, **7**, 536–541.

Chapin, F., P. Matson, and H. Mooney, 2002: *Principles of Terrestrial Ecosystem Ecology*. Springer.

Chapman, S., et al., 2001: Ecoregions of Nebraska and Kansas (color poster with map, descriptive text, summary tables, and photographs). Tech. rep., U.S. Geological Survey.

Ciais, P., P. Rayner, F. Chevallier, P. Bousquet, M. Logna, P. Peylin, and M. Ramonet., 2010: Atmospheirc inversions for estimating CO_2 fluxes: methods and perspectives. *Climatic Change*, **103**, 69–92.

Coutts, A., J. Beringer, and N. Tapper, 2007: Characteristics influencing the variability of urban CO_2 fluxes in Melbourne, Australia. *Atmos. Environ.*, **41**, 51–62.

de Wekker, S. F. J., A. Ameen, G. Song, W. J. Steenburgh, and B. Stephens, 2008: An investigation of the effect of valley boundary layer structure on atmospheric CO_2 concentrations at a mountain top location. *Proceedings of the 13th conference on Mountain Meteorology*, American Meteorological Society.

Durran, D. R., M.-J. Yang, D. N. Slinn, and R. G. Brown, 1993: Toward more accurate wave-permeable boundary conditions. *Mon. Wea. Rev.*, **121**, 604–620.

Efron, B., 1979: Bootstrap methods: another look at the jackknife. *The Annals of Statistics*, **7**, 1–26.

Ehleringer, J., A. Moyes, C. Cook, D. Pataki, C.-T. Lai, and A. Schauer, 2009: Long-term results from an urban CO_2 monitoring network, Eos Trans. AGU, Fall Meet. Suppl., Abstract B33D-0414.

Environmental Protection Agency, 1990: Clean Air Act: 42 U.S.C. 7401-7671g. Tech. rep., United States of America.

Gillies, R., S. Want, and M. Booth, 2010: Atmospheric scale interaction on wintertime intermountain west low-level inversions. *Wea. Forecasting*, **25**, 1196–1210.

Gottschalk, P., G. Churkina, M. Wattenbach, and U. Cubasch, 2010: Assessment of the potential of urban organic carbon dynamics to off-set urban anthropogenic fluxes, Eos Trans. AGU, Fall Meet. Suppl., Abstract B21E-0355.

Gratani, L. and L. Varone, 2005: Daily and seasonal variation of CO_2 in the city of Rome in relationship with the traffic volume. *Atmos. Environ.*, **39**, 2619–2624.

Griffith, G., et al., 2009: Ecoregions of New England (color poster with map, descriptive text, summary tables, and photographs). Tech. rep., U.S. Geological Survey.

Grimmond, C. S. B., T. S. King, F. D. Cropley, D. J. Nowak, and C. Souch, 2002: Local-scale fluxes of carbon dioxide in urban environments: methodological challenges and results from Chicago. *Environ. Pollut.*, **116**, S243–S254.

Gurney, K. R., D. L. Mendoza, Y. Zhou, M. L. Fischer, C. C. Miller, S. Geethakumar, and S. de la Rue du Can, 2009: High resolution fossil fuel combustion CO_2 emission fluxes for the United States. *Environ. Sci. Technol.*, **43**, 5535–5541.

Henninger, S., 2008: Analysis of near surface CO_2 variability within the urban area of Essen, Germany. *Meteorologische Zeitschrift*, **17**, 19–27.

Holstag, A. A. M. and A. P. V. Ulden, 1983: A simple scheme for daytime estimates of surface fluxes from routine weather data. *J. Appl. Meteor.*, **22**, 517–529.

Holzworth, G. C., 1967: Mixing depths, wind speeds and air pollution potential for selected locations in the United States. *J. Appl. Meteor.*, **6**, 1039–1044.

Homer, C., C. Huang, L. Yang, B. Wylie, and M. Coan, 2004: Development of a 2001 National Landcover Database for the United States. *Photogramm. Eng. Rem. S.*, **70**, 829–840.

Horel, J., et al., 2002: MesoWest: Cooperative mesonets in the United States. *Bull. Amer. Meteor. Soc.*, **83**, 211–226.

Idso, C. D., S. B. Idso, and R. Balling Jr., 1998: The urban CO_2 dome of Phoenix, Arizona. *Physical Geography*, **19**, 95–108.

Idso, C. D., S. B. Idso, and J. R. C. Balling, 2001: An intensive two-week study of an urban CO_2 dome in Phoenix, Arizona, USA Phoenix, AZ, USA. *Atmos. Environ.*, **35**, 995–1000.

Idso, S. B., C. D. Idso, and J. R. C. Balling, 2002: Seasonal and diurnal variations of near-surface atmospheric CO_2 concentration within a residential sector of the urban CO_2 dome of Phoenix, AZ, USA. *Atmos. Environ.*, **36**, 1655–1660.

IPCC, 2007: *Climate Change 2007: The physical science basis. Contribution of Working Group I to the Fourth Assessment Report of the Intergovernment Panel on Climate Change*. Geneva: IPCC.

Jacobson, M. Z., 2010: Enhancement of local air pollution by urban CO_2 domes. *Environ. Sci. Technol.*, **44**, 2497–2502.

Keeling, R., J. Chin, and T. P. Whorf, 1996: Increased activity of northern vegetation inferred from atmospheric CO_2 measurements. *Nature*, **382**, 146–149.

Kelome, N., J. Leveque, F. Andreux, M. Milloux, and L. Ovede, 2006: C4 plant isotopic composition (d13C) evidence for urban CO_2 pollution in the city of Cotonou, Benin (West Africa). *Science of the Total Environment*, **366**, 439–447.

Koerner, B. and J. Klopatek, 2002: Anthropogenic and natural CO_2 emission sources in an arid urban environment. *Environ. Pollut.*, **116**, S45–S51.

Lareau, N., E. Crosman, C. Whiteman, J. Horel, and S. Hoch, 2012: The persistent cold-air pool study. *Bull. Amer. Meteor. Soc.*, **in review**.

Lettau, H. H., 1970: Physical and meteorological basis for mathematical models of urban diffusion processes. *Proceeding of Symposium on Multiple-Source Urban Diffusion Models*, A. C. Stern, Ed., U.S. Environmental Protection Agency.

Lichtfouse, E., M. Lichtfouse, and A. Jaffrezic, 2003: d13C values of grasses as a novel indicator of pollution by fossil-fuel-derived greenhouse gas CO_2 in urban areas. *Environmental Science and Technology*, **37**, 87–89.

Loveland, T. and A. Belward, 1997: The IGBP-DIS global 1km land cover data set, DISCover: First results. *International Journal of Remote Sensing*, **18**, 3289–3295.

Luthi, D., et al., 2008: High resolution carbon dioxide concentration record 650,000 to 800,000 years before present. *Nature*, **453**, 379–382.

Malek, E., T. Davis, R. Martin, and P. Silva, 2006: Meteorological and environmental aspects of one of the worst national air pollution episodes (January, 2004) in Logan, Cache Valley, Utah, USA. *Atmos. Res.*, **79**, 108–122.

McKain, K., W. S., T. Nehrkorn, J. Eluszkiewicz, J. Ehleringer, and B. Stephens, 2012: Assessment of ground-based atmospheric observations for verification of greenhouse gas emissions from an urban region. *PNAS*, **109**, 8423–8428.

McPherson, E. G. and J. R. Simpson, 1999: Carbon Dioxide Reduction Through Urban Forestry: Guidelines for Professionals and Volunteer Tree Planters. Tech. rep., U. S. Forest Service.

Miller, M. E., 1967: An atmospheric diffusion model for metropolitan areas. *J. Air Pollution Control Association*, **17**, 46–50.

Molina, L. and M. Molina, 2002: Air quality in the Mexico megacity: an integrated assessment. *Kluwer Academic Publishers*, 21–59.

Monson, R. K., et al., 2005: Climatic influences on net ecosystem CO_2 exchange during the transition from wintertime carbon source to springtime carbon sink in a high-elevation, subalpine forest. *Oecologia*, **146**, 130–147.

Moriwaki, R. and M. Kanda, 2004: Seasonal and diurnal fluxes of radiation, heat, water vapor and CO_2 over a suburban area. *J. Appl. Meteor.*, **43**, 1700–1710.

Moriwaki, R., M. Kanda, and H. Nitta, 2006: Carbon dioxide build-up within a suburban canopy layer in winter night. *Atmos. Environ.*, **40**, 1394–1407.

Nasrallah, H. A., J. R. C. Balling, S. M. Madi, and L. Al-Ansari, 2003: Temporal variations in atmospheric CO_2 concentrations in Kuwait City, Kuwait with comparisons to Phoenix, Arizona, USA. *Environ. Pollut.*, **121**, 301–305.

Nowak, D. J. and D. E. Crane, 2002: Carbon storage and sequestration by urban trees in the USA. *Environ. Pollut.*, **116**, 381–389.

Nowak, D. J., J. C. Stevens, S. M. Sisinni, and C. J. Luley, 2002: Effects of urban tree management and species selection on atmospheric carbon dioxide. *J. Aboriculture*, **28**, 113–122.

Oke, T. R., 1967: City size and the urban heat island. *Atmos. Environ.*, **7**, 769–779.

Pataki, D. E., D. R. Bowling, and J. R. Ehleringer, 2003: Seasonal cycle of carbon dioxide and its isotopic composition in an atmosphere: anthropogenic and biogenic effects. *J. Geophys. Res.*, **108**, doi:10.1029/2003JD003865.

Pataki, D. E., D. R. Bowling, and J. R. Ehleringer, 2006: High resolution atmospheric monitoring of urban carbon dioxide sources. *Geophys. Res. Lett.*, **33**, doi:10.1029/2005GL024822.

Pataki, D. E., P. C. Emmi, C. B. Forster, J. I. Mills, E. R. Pardyjak, T. R. Peterson, J. D. Thompson, and E. Dudley-Murphy, 2009: An integrated approach to improving fossil fuel emissions scenarios with urban ecosystem studies. *Ecol. Complex.*, **6**, 1–14, doi:10.1016/j.ecocom.2008.09.003.

Pataki, D. E., B. J. Tyler, R. E. Peterson, A. P. Nair, W. J. Steenburgh, and E. R. Pardyjak, 2005: Can carbon dioxide be used as a tracer of urban atmospheric transport? *J. Geophys. Res.*, **110**, doi:10.1029/2004JD005723.

Pataki, D. E., T. Xu, Y. Q. Luo, and J. R. Ehleringer, 2007: Inferring biogenic and anthropogenic carbon dioxide sources across an urban to rural gradient. *Oecologia*, **152**, 307–322.

Ramamurthy, P. and E. R. Pardyjak, 2011: Toward understanding the behavior of carbon dioxide and surface energy fluxes in the urbanized semi-arid Salt Lake Valley, Utah, USA. *Atmos. Environ.*, **45**, 73–84.

Reeves, H. and D. Stensrud, 2009: Synoptic-scale flow and valley cold-pool evolution in the Western United States. *Wea. Forecasting*, **24**, 1625–1643.

Reid, K. H. and D. G. Steyn, 1997: Diurnal variations of boundary-layer carbon dioxide in a coastal city – observations and comparison with model results. *Atmos. Environ.*, **31**, 3101–3114.

Silcox, G., K. Kelley, E. Crosman, C. Whiteman, and B. Allen, 2001: Wintertime PM2.5 concentrations during persistent, multi-day cold-air pools in a mountain valley. *Atmos. Environ.*, **46**, 17–24.

Soegaard, H. and L. Moller-Jensen, 2003: Towards a spatial co2 budget of a metropolitan region based on textural image classification and flux measurements. *Remote Sensing of Environment*, **87**, 283–294.

Strong, C., C. Stwertka, D. Bowling, B. B. Stephens, and J. Ehleringer, 2011: Urban carbon dioxide cycles within the Salt Lake Valley: A multiple-box model validated by observations. *J. Geophys. Res.*, **116**, 1508.

Stull, R. B., 1988: *An Introduction to Boundary Layer Meteorology*. Kluwer Academic Press, Netherlands.

Stwertka, C., C. Strong, D. Bowling, and N. Lareau, 2012: Carbon dioxide variability in the Salt Lake Valley during the Persistent Cold Air Pool Study (PCAPS). *Atmos. Environ.*, in preparation.

Takahashi, H., E. Konohira, T. Hiyama, M. Minami, T. Nakamura, and N. Yoshida, 2002: Diurnal variation of CO_2 concentration, Delta14C and d13C in an urban forest: estimate of the anthropogenic and biogenic CO_2 contributions. *Tellus*, **54**, 97–109.

UNFP, 2007: UNFPA State of World Population 2007: Unleashing the Potential of Urban Growth. Tech. rep., United Nations Population Fund.

Urban Renewal Administration, U. and U. Bureau of Public Records, 1965: *Standard land use coding manual, a standard system for identifying and coding land use activities*. United States Government Printing Office.

Urbanski, S., et al., 2007: Factors controlling CO_2 exchange on timescales from hourly to decadal at Harvard Forest. *J. Geophys. Res.*, **112**, doi:10.1029/2006JG000293.

U.S. Census Bureau, 2012: State and County QuickFacts: Steamboat Springs, Colorado. URL `http://quickfacts.census.gov/qfd/states/08/0873825.html`, URL `http://quickfacts.census.gov/qfd/states/08/0873825.html`.

USEIA, 2011: State CO_2 Emissions. Tech. rep., U.S. Energy Information Administration.

Velasco, E., S. Pressley, E. Allwine, H. Westberg, and B. Lamb, 2005: Measurements of CO_2 fluxes from the Mexico City urban landscape. *Atmos. Environ.*, **39**, 7433–7446.

Verma, S. B., et al., 2005: Annual carbon dioxide exchange in irrigated and rainfed maize-based agroecosystems. *Agr. Forest Meteorol.*, **131**, 77–96.

Western Regional Climate Center, 2012: Stockton, California: normals, means and extremes. Tech. rep.

Whiteman, C., X. Bian, and S. Zhong, 1999: Wintertime evolution of the temperature inversion in the Colorado plateau basin. *J. Appl. Meteor.*, **38**, 1103–117.

Whiteman, C., W. Zong, J. Shaw, M. Hubble, X. Bian, and J. Mittelstadt, 2001: Cold pools in the Columbia Basin. *Wea. Forecasting*, **16**, 432–447.

Widory, D. and M. Javoy, 2003: The carbon isotope composition of atmospheric co_2 in Paris. *Earth and Planetary Science Letters*, **215**, 289–298.

Wofsy, S. C., S. C., K. McKain, J. Eluszkiewicz, T. Nehrkorn, D. E. Pataki, and J. R. Ehleringer, 2010: An observational method for verifying trends in urban CO_2 emissions using continuous measurements and high resolution meteorology, Eos Trans. AGU, Fall Meet. Suppl., Abstract A13F-0280.

Wofsy, S. C., M. L. Goulden, J. W. Munger, S. M. Fan, P. S. Bawkin, B. C. Daube, S. L. Bassow, and F. A. Bazzaz, 1993: Net exchnage of CO_2 in a midlatitude forest. *Science*, **5112**, 1314–1317, doi:10.1126/science.260.5112.1314.

Wolyn, P. and T. McKee, 1989: Deep stable layers in the intermountain Western Uunited States. *Mon. Wea. Rev.*, **117**, 461–472.

Woods, A., D. Lammers, S. Bryce, J. Omerinik, R. Denton, M. Domeier, and J. Comstock, 2001: Ecoregions of Utah (color poster with map, descriptive text, summary tables, and photographs). Tech. rep., U.S. Geological Survey.

Xu, L. K. and D. D. Baldocchi, 2004: Seasonal variation in carbon dioxide exchange over a Mediterranean grassland in California. *Agr. Forest Meteorol.*, **123**, 79–96.

Zangl, G., 2003: The impact of upstream blocking, drainage flow and the geostrophic pressure gradient on the persistence of cold-air pools. *Quart. J. Roy. Meteor. Soc.*, **129**, 117–137.

Zimnoch, M., T. Florkowski, J. Necki, and R. Neubert, 2004: Diurnal variability of d13C and d18O of atmospheric CO_2 in the urban atmosphere of Krakow, Poland. *Isotopes in Environmental and Health Studies*, **40**, 129–143.

Zong, S., C. Whiteman, X. Bian, J. Shaw, and J. Hubbe, 2001: Meteorological processes affecting evolution of a wintertime cold air pool in a large basin. *Mon. Wea. Rev.*, **129**, 2600–2613.